Università degli Studi di Torino
Doctoral School of Sciences and Innovative Technologies
PhD Programme in Chemical and Materials Sciences XXX Cycle

Study of the mechanical acoustic properties of brake pads

Simone Balestra

Supervisor:
prof. Ettore Vittone
Dott. Agusti Sin

Università degli Studi di Torino

Doctoral School of Sciences and Innovative Technologies
PhD Programme in Chemical and Materials Sciences XXX Cycle

Study of the mechanical acoustic properties of brake pads

Candidate: Simone Balestra

Supervisor: prof. Ettore Vittone
Dott. Agusti Sin

Jury Members: prof. Francesco Andreatta
University of Udine
Department of engineering and architecture
prof. Paolo Colombo
University of Padova
Department of Industrial Engineering

PhD Programme Coordinator: prof. Bartolomeo Civalleri

Torino, 2020

Abstract

Noise and vibration in automotive field are matters of primary importance and one of the main causes of noise originate from braking system. The movement of an object on a surface generates a friction force that is opposed to the motion. Friction can generate vibration in the body that can produce mechanical noise. The study of causes of friction force vibration generated by a brake pad is of remarkable interest in order to increase the vehicle comfort. Noises produced by brake pads are numerous and differentiated for their frequency and their generation mechanisms. One of these mechanisms, the so called *Stick-Slip*, generates a low frequency noise called *Creep Groan*. This thesis deals with the study of noise generation and propagation, carried out at the ITT company (Barge (CN), Italy).
In order to mitigate noise, brake pads are equipped with rubber underlayers, having the function of vibration dampers. However at low temperatures, rubber has a higher stiffness resulting in raising of acoustic components in the kHz range, which are not present at room temperature. This squeal problem is the so called *Cold noise*, nowadays there aren't underlayers that are able to damp this kind of vibration.
The goal for the noise generation is to define a measurement protocol for the tribological characterization, using a tribometer and dyno/vehicle test. The purpose of this protocol is to classify the friction materials according to their propensity to generate *Stick-Slip* processes in different environmental conditions. These measures are then compared with measures done with the same material on vehicle and on dyno test. From the comparison of these measures, a good correlation is found, showing an efficient laboratory friction material characterization protocol. The second aim was to correlate the noise generated with environmental parameters, in particular relative humidity, and with physical and chemical features of brake pad. The intensity and the number of *Stick-Slip* events is correlated with the humidity and the surface level of friction distribution. In order to understand the impact of the surface morphology on friction a study was done on polyethylene patterned surfaces. Different surface geometry are tested on tribometer and the friction behavior was investigate as a function of sliding velocity, pressure and relative humidity.
The goal for the noise propagation is to define the raw materials and underlayer features as a function of temperature and stress frequency. The main technique is the Dynamic Mechanical Thermal Analysis, this laboratory test is useful for studying the viscoelastic behaviour of polymer. Applying the Williams–Landel–Ferry theory and the time-temperature superposition principle, is possible to study the polymer behaviour (and underlayer) in a wide frequency range. The rubber composition influences the underlayer frequency response and glass transition. The influence of the underlayer composition on the brake pad was evaluated with dyno tests and analyzing the frequency response as a function of temperature. The friction material has no significant variation in the considered temperature range, so the *Cold noise* is affected by the underlayer

only. The main cause identified and studied is the rubber glass transition. The underlayer damping properties influence the brake pad damping, a relationship was found between frequency response function, Williams-Landel–Ferry and dyno results. The created characterization procedure allowed to develop new UL formulations that reduce mechanical vibration. The developed materials have been patented.

Contents

Chapter 1

Introduction

1.1 Thesis project

The thesis was born from a collaboration between University of Turin and ITT Motion Technologies and it was developed at R&D laboratory of the company, in Barge headquarter (CN). ITT Motion Technologies studies, tests and produces brake pads in Barge headquarters. The aim of the thesis is to investigate the phenomena related to the **generation** and **propagation** of noise.
An object on motion on a surface generates a friction force that is opposed to the motion. This force is not constant but vibrates around a mean value. The cause of these vibrations are due to microscopic effects occurring between the contact surfaces. The vibration of the force could generate vibration on the body and then mechanical noise. This phenomenon is the base of noise produced during a car brake and its study and understanding is of remarkable interest in automotive field. One kind of friction instability is generated by the *Stick-Slip* process. *Stick-Slip* could be studied with a tribometer that allows friction force measurement. A consistent part of the work was to find a right protocol of measure. A particular kind of noise generated by *Stick-Slip*, called *Creep Groan*, had been studied. *Creep Groan* is a low frequency noise and that makes it harder to filter mechanically once generated. For this reason, it is important to study the propensity of the friction material to generate *Creep Groan*.
Regarding the noise propagation, the goal is to characterize the mechanical properties of underlayer, which have the main task of damping mechanical vibrations. The two most important parameters are temperature and frequency to characterize the elastic and viscous properties of the underlayer and elastomer inside it. The main techniques that allow this characterization are the DMTA (Dynamical-Mechanical-Thermal analysis) and the FRF (Frequency Response Function). The analysis aims to define which are the main suitable raw materials to dampen certain vibrations, and consequently, to lay the foundations for formulating underlayers that contain such raw materials in suitable

quantities. The main type of noise on which attention is focused is the so called *Cold Noise*, that is, the worsening of the situation at low temperature, with the onset of characteristic frequencies that are absent at room temperature; but in general the approach is valid for any Squeal problem.

1.2 ITT Motion Technologies

ITT Motion Technologies is a multinational leader in the brake pads production. It is part of the ITT Corporation, a listed company with headquarters in White Plains, in the USA. ITT Corporation was born in 1920 and at the beginning operated in the telecommunication field, hence the name International Telephone and Telegraph. After the Second World War ITT broadened its horizons through new field of interest like military defense and valves and pumps for the transport of fluid. Now the ITT Corporation is one of the biggest listed society of USA and works in many fields like components for industrial process, brake pads, connector for transport of oil and gas. Barge Company was born in 1962 like a second production plant of the Galfer Company. Galfer Company, specialized in brake pads production, was born in 1950 in Turin, and ITT Corporation bought it in 1977. After that, the production was concentrated in Barge. In 1981 in Barge the R&D department was established, and now it is the first research pole of ITT Corporation in brake pads field.

1.3 Vehicle braking system

The brake system is one of the most important components in a vehicle. The braking system has evolved over the years, nowadays it is more reliable and safer. Your brakes work as hard or harder than any other part of the car, however much energy it takes to get your car up a hill, it takes at least as much energy to stop it at the bottom.
Vehicle braking system is the ensemble of components that allows the car to slow down and stop. The brake system most used is the disc brake and it takes advantage of the friction force generated by the brake pads pressed against the rotor in order to slow down and stop vehicles. Braking system brakes vehicles transforming kinetic energy into thermal energy. Over the years the mass and the speed of the vehicle has been raising and so does the amount of kinetic energy to transform, leading the research to more performing and secure pads and discs.
The principal braking system components are pedal, brake line, caliper, pistons, brake pad and brake disc (Fig. 1.1). The brake disc (or rotor in American English) is usually made of cast iron, but may in some cases be made of composites such as reinforced carbon-carbon or ceramic matrix composites. This is connected to the wheel and/or the axle. To stop the wheel, friction material in the form of brake pads, mounted on a device

called brake caliper, is forced mechanically, hydraulically, pneumatically or electromagnetically against both sides of the disc. Friction causes the disc and attached wheel to slow or stop. Brakes convert motion to heat, and if the brakes get too hot, they become less effective, a phenomenon know as brake fade (occurring at T>300 °C). Since major disc brake components are exposed to air, heat generated during braking can dissipate efficiently, which offers high resistance to brake fade. In addition, since water is flung off the rotor due to its rotation, the phenomenon of water fade (significant loss of braking performance caused by buildup of water on the disc) becomes less likely to occur, which in turn provides safer and more stable braking performance. Disc brake calipers provide a housing for the hydraulic piston or pistons that force the brake pads into contact with the disc. The disc brake caliper assembly is bolted to the vehicle axle housing or suspension. When the brakes are applied, hydraulic pressure force both pistons inwards, causing the pads to come in contact with the rotating disc. When the brakes are applied, hydraulic pressure force the piston inwards. This pushes the pad against the disc. The caliper is free to move on slides, so there is a clamping effect between the inner and outer pads. Equal force is then applied to both pads which clamp against the disc. In disc brake calipers, the piston moves against a stationary square section sealing ring. When the brakes are applied, the piston slightly deforms the seal. When the brakes are released, the seal returns to its original shape. The action of this sealing ring retracts the piston to provide a small running clearance between the disc and pads. It also makes the brake self-adjusting. The driver press the pedal that, through the brake line, put under pressure the piston and the brake pads is pressed against the disc. The brake pads for each vehicle are eight, two per wheel. Anterior and posterior pads are different between them, since the anterior brake give the 75-80% of contribution to the brake. Braking system is a fundamental component of any vehicle and it is subject to specific security rules.

1.4 Brake Pad

Brake pads are a component of disk brakes used in automotive and other application. Brake pads are steel backing plates with friction material bound to the surface that faces the disk brake rotor. Brake pads convert the kinetic energy of the car to thermal energy by friction. Two brake pads are contained in the brake caliper with their friction surface facing the rotor. When the brakes are hydraulically applied, the caliper clamps or squeezes the two pads together into the spinning rotor to slow/stop vehicle. The brake pad and disc provide the friction that stops the vehicle. In disc brake application, there are usually two brake pads per disc rotor, held in place and actuated by a caliper affixed to a wheel hub or suspension upright. Although almost all road-going vehicles have only two brake pads per caliper, racing calipers utilize up to six pads, with varying frictional properties in a staggered pattern for optimum performance. The brake pads

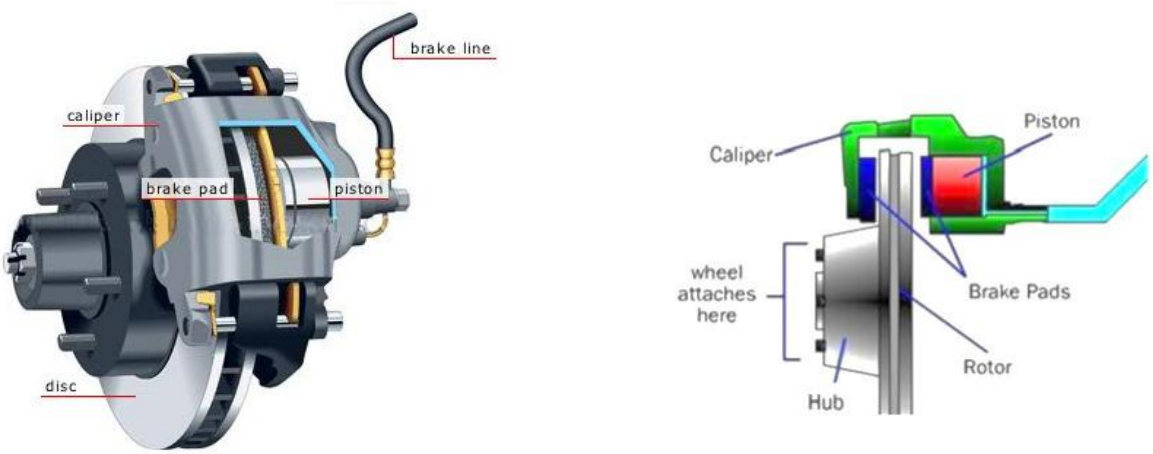

Figure 1.1: Scheme of a brake system (disc brake) [1].

must usually be replaced regularly (depending on pad material), and most are equipped with a method of alerting the driver when this needs to take place. Some have a thin piece of soft metal that causes the brakes to squeal when the pads are too thin, while others have a soft metal tab embedded in the pad material that closes an electric circuit and lights a warning light when the brake pad gets thin. More expensive cars may use an electronic sensor.

1.4.1 Brake pad composition

Many layers compose brake pads, they are the following (Fig.1.2 from the top downards):

- *Friction material layer* (thickness ~10mm);
- *Underlayer* (thickness ~3mm);
- *Adhesive Layer*, phenolic resin;
- *Backplate*, the metal support (thickness ~5mm);
- *Shim*, an anti-noise sheet.

Figure 1.2: Composition of a generic brake pad [2].

A good friction material must have the following characteristic:

- A friction coefficient of about 0.4 (depend on car maker requirement);
- Low wear;
- Low abrasiveness on disc;
- Stable friction coefficient at different temperature, humidity and speed;
- Low environmental impact (link to wear particulate emission);
- Appropriate thermal conductivity;
- Low noise generation.

In order to achieve this requisite, the friction material is a mixture of many materials from the following different family:

- *Metals* that are present as fibers or powders, in order to increase mechanical resistance and high temperature stability;
- *Abrasives* to regulate coefficient of friction;
- *Lubricants* to reduce wear;
- *Organic compounds*, like rubber and resins, to bind the material and to reduce vibration;
- *Binders* that are the matrix for the mixture (e.g. phenolic resin);

- *Fibers* to provide mechanical property to the pad;
- *Fillers*, to reduce the pad cost. They do not have to change material characteristic.

The underlayer is a layer that has as first aim the vibration and noise damping. It contains elastomers. Second purpose of underlayer is thermal insulation. This because during braking, the temperature of the pads can reach 700 °C, and if the relevant heat flow reaches the oil present into cantilever can induce the phase change of oil and to cause serious problems to the brake system.

1.4.2 Brake pads productive process

The brake pad production can be summarized as follow:

- Purchase of a backplate, sandblaster cleaning and roughness control;
- Adhesive layer application;
- Friction material and underlayer application;
- Press molding stage. In this stage, there is the combined effect of temperature and pressure in order to allow the resin reticulation and the powder compression.
- Final-Curing, the pads are put in an oven in order to complete the reticulation;
- Grinding, pad width control, eventual geometrical modification with bevels and notch;
- Industrial painting, in order to avoid backplate oxidation;
- Finishing.

Production batches are subject to quality control as tangential detachment control test, material distribution uniformity control, pad compressibility measure, chemical analysis and vehicle tests in order to evaluate pads security. On chassis dynamometer the pads are tested to characterize friction in different conditions and pad security. On vehicle there are two more used tests that are alpine downhill (in order to test the pads at high temperature) and stop test at maximum speed on track.

1.5 NAO and Low Steel material

ITT produces two different families of brake pads, *Non Asbestos Organic* (*NAO*) and *Low Steel* (LS) materials. These two families have different pros and cons and follow different global markets. *Low Steel* materials (developed in the 1970s) contain iron and are more performing. So their friction coefficients are higher and more stable at different temperature. *NAO* (first developed in the late 1960s) typically contain nonferrous metals, these materials are more comfortable and generate less noise. *LS* are sold principally in the European market while *NAO* are sold in the USA market.
The typical characteristics of *Low Steel* are: high level of coefficient of friction (0.38-0.50), good pedal feel and braking confidence, good fade and high speed performance, high rotor and pad wear, large amount of wheel dust, high noise propensity and short pad life. The typical characteristic of *NAO* are: low to medium coefficient of friction (0.33-0.40), excellent wear resistance at low temperature (<200 °C), good for wheel dust, good noise and roughness characteristic and more expensive.

One aim of *IIT* is to find a material that has *LS* performance and *NAO* comfort.

1.6 Comfort

Comfort in a vehicle is assuming an ever more important role in the automotive market. In order to have a more comfortable vehicle it is important to reduce all the noises produced by the vehicle. A consistent part of the noise produced by a vehicle comes from braking system. For this reason it is important to study noise generation and propagation during the brake. In general the noise generation is linked to a friction force instability, while the noise propagation is linked to all the brake system [3]. There are a lot of different noises produced by brake pads. These are classified according to their frequencies and generation causes, as shown in figure 1.3. Brake squeal is a phenomenon of dynamic instability that occurs at one or more of the natural frequencies of the brake system. The disc rotor is acting like a 'speaker' (sound wave coming from the rotor surfaces). Pads and rotor coupling has major impact on mid to high frequency (4-16 kHz) squeal. Brake squeal, although annoying and sometimes embarrassing, is not a safety related issues. Low frequency (1-3 kHz) squeal typically involves caliper, anchor bracket, knuckle and suspension, in addition to pads and rotor. Low frequency noise is caused by friction material excitation at the rotor and lining interface that is transmitted trough the brake corner and couples with other chassis components. Different noises need different ways to reduce them. It is hard to filter a low frequency noise, therefore it is important to work on the composition of the friction material in order not to generate noise. For this reason in order to avoid noise like *Creep Groan* (a low frequencies noise) it is fundamental to find a material that do not generate it. In order to do this it is important to identify the causes of this noise. The high frequency noise like *Squeal* can

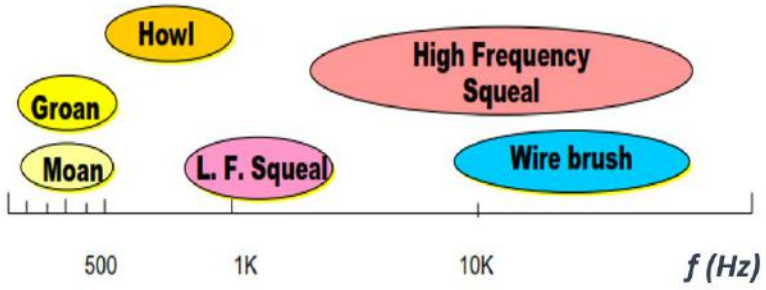

Figure 1.3: Frequencies of different noises [4].

be filtered out with the underlayer, that works like a low-pass filter, directly on the brake pad.

1.7 Performance characteristics

The performance characteristics depend on brake pad, caliper and rotor; therefore a strict cooperation between companies is necessary to provide a final product that meet the needs.
Generally IIT is working in co-design with caliper and disc maker and each take part for all the activities needed in DVP[1] plan deciding together each time in case of problems the direction to follow to find a solution. The main performance characteristics are:

- Efficiency. Typical test AK master: the friction level are measured in different conditions of speed, pressure and temperature. Fading (temperature sensibility with drop down of friction) and recovery are also considered from the test.
- Durability. Measurement the pad and disc wear at different condition of temperature or dyno simulation of specific usage of common driver (LACT - Los Angeles city traffic, Mojacar,...)
- Judder. Cold judder measurement of the tendency to generate vibration with generation of DTV[2] on vehicle or dyno. Hot judder measurement of the tendency to generate vibration at high speed and low pressure.
- NVH[3]. Measurement of the tendency to generate noise on vehicle or dyno.

[1]Design Verification Plan.
[2]Different Thickness Variation.
[3]Noise, Vibration and Harshness.

- Stiction corrosion. Measurement of the tendency of the pad to stick on the disc due to corrosion phenomena.
- Residual torque. Measurement of the tendency to torque without braking. Usually this is a caliper problem.
- Crack disc. Measurement of the tendency to generate cracks on the disc.
- AMS[4]. Measurement of the stopping distance during 10 application from 100 km/h to zero at max deceleration.
- Static friction. Measurement of friction level in static condition at different clamping force and different temperature and different slope. Evaluation of the roll away at different temperature (on vehicle or on dyno).

[4]Auto Motor Sport.

Chapter 2

Theoretical outline on noise generation

2.1 Tribology

Tribology is the science that studies friction, lubrication and wear. The word derives from the Greek word Tribos meaning rubbing. Surface interactions in a tribological interface are highly complex, and their understanding requires knowledge of various disciplines including physics, chemistry, applied mathematics, solid mechanics, fluid mechanics, thermodynamics, heat transfer, materials science, rheology. Tribological studies are crucial in cost reduction and security improvement in many field. Examples of unproductive friction may be observed in combustion engines, gears, bearing. Examples of productive friction are brakes, car tires, bolts and nuts. According to some estimates, losses resulting from ignorance of tribology amount in the United States to about 4% of its gross national product [5].

2.2 Coefficient of friction

Friction force F_f is the force that opposes the motion. If an object is in motion in a straight line, F_f is the force to apply in the motion direction and orientation in order to keep the motion at a constant speed. If the object is motionless, F_f is the force that is necessary to keep the object motionless.
The most important value used during friction study is the *Coefficient of Friction* (CoF). CoF is a dimensionless number and it is defined as the ratio between F_f and normal force F_N (Fig. 2.1). The classical Coulomb's law of friction is:

$$CoF = \frac{F_f}{F_N} \tag{2.1}$$

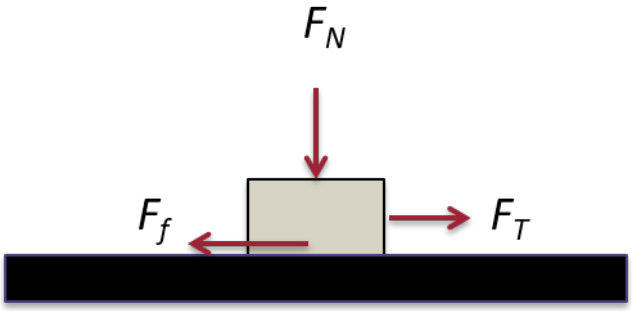

Figure 2.1: Friction coefficient definition.

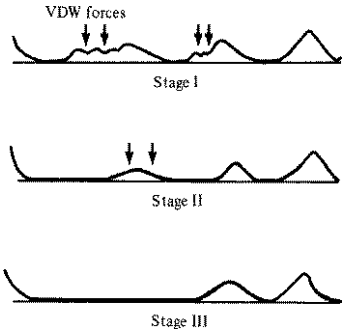

Figure 2.2: Increasing of contact area due to the Van der Waals forces [5].

F_f depend by the condition of motion of the body and so two different definitions of CoF are used: **static** and **dynamic**. The friction is due to the shear stress of the atoms in contact between the two surfaces. It has a distribution on the real contact area. The CoF is commonly assumed to be independent of surface area, normal reaction force and sliding speed, as originally determined by Leonardo da Vinci (1452–1519), Coulomb and Guillaume Amonton (1663–1705), but these approximations are rarely applicable.

2.2.1 Static coefficient of friction

Assuming that the body is motionless and that there is a tangential force F_t operating on it, F_f is equal and opposite to F_t. If F_t increases until the body starts to move, changing its name in F_T, then the Static Coefficient of Friction CoF_s is defined as:

$$CoF_s = \frac{F_T}{F_N} \tag{2.2}$$

F_T is the critical static force.

In general, CoF_s is independent from the nominal area of contact.

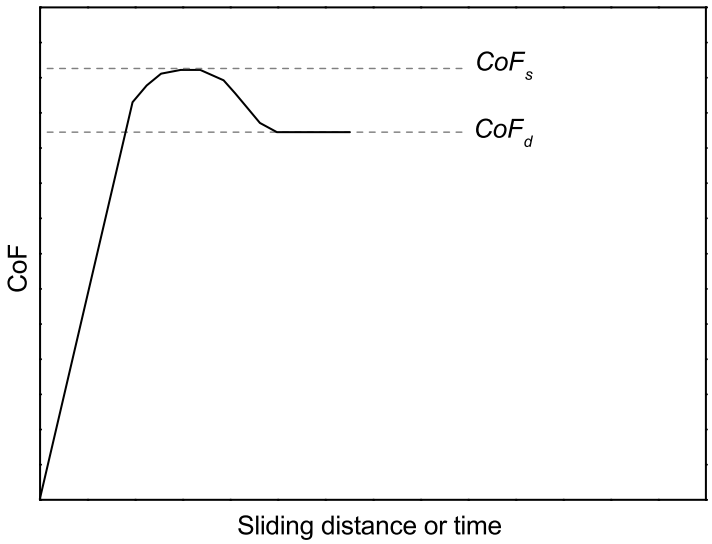

Figure 2.3: Definition of static and dynamic coefficient of friction [6].

2.2.2 Dynamic coefficient of friction

If the body is in motion, F_f is defined as the force that opposes the motion. In this case the Dynamic Coefficient of Friction CoF_d, often called simply Coefficient of Friction, is defined in the 2.1.
Dynamic CoF is always lower than *Static CoF*. This because when the body is motionless it creates more bonds with the surface, because of Van der Waals forces, and start moving is harder than keep it going. In this way also the real area of contact increases as shown in the figure 2.2 [5]. The difference between the two values of CoF could generate a phenomenon on the motion called *Stick-Slip*. The CoF_d is independent from the nominal area of contact while it may depend on the sliding speed (specially at high speeds). If two bodies in contact are subjected to sliding with a velocity v, the junctions tend to continuously break off and then reform in other points. A dynamic equilibrium is thus reached characterized by the same rate of formation and breaking of the junctions [6].

2.3 Stick-Slip

Stick-Slip is the process that happens when a system changes its state periodically from static to dynamic. Generally the static friction coefficient is 20-30% higher than the dynamic one [6]. In static phase system accumulates potential energy that releases in

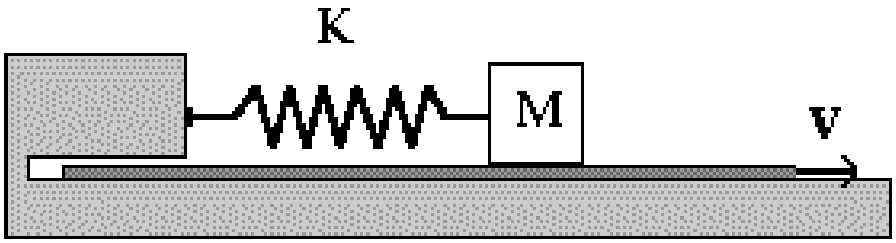

Figure 2.4: *Stick-Slip* mechanical model [10].

dynamic phase. The intensity and periodicity of this process is highly variable and the probability of happening increases with increasing the the CoF_s-CoF_d difference and the probability that happens increases with the increase of the difference between static and dynamic CoF. *Stick-Slip* is a multiscale phenomenon that could interest macroscopically the whole system, only the single contact and in the Prandt Tomlinson model comes out in atomic friction. There are different types of *Stick-Slip*: periodic, random and stepped [7]. Many apparently different natural events show the *Stick-Slip* phenomenon. Examples of *Stick-Slip* processes are the motion on a surface of mass with elastic propriety, the hiss of a plaster, mechanism of sound emission of a violin [8], it is found in the sound producing apparatus of spiny lobster species (Palinuridae) [9], earthquakes...
Understanding the *Stick-Slip* is a long-standing challenge for engineers and physicists.

2.3.1 Mechanical model of Stick-Slip process

The most simple example of a system with *Stick-Slip* process is a block of mass M linked to a fixed spring with elastic constant k, that slides with a friction over a surface moving beneath it at constant velocity v. The system is shown in figure 2.4.
$x(t)$ is the position of the block and $x(0) = 0$. At $t = 0$ the spring is in the rest position and the surface starts to move. So in this situation the motion equation is:

$$x(t) = vt \tag{2.3}$$

The equation of the elastic force is:

$$F_{el} = -kx(t) = -kvt \tag{2.4}$$

and at the instant t_1 it is equal to the critical static force F_T, and from 2.2:

$$F_T = CoF_s F_N = CoF_s Mg \tag{2.5}$$

Where $F_N = Mg$ is the normal force, CoF_s the static CoF. At this point the spring attracts the block and so the block is subjected to the dynamic friction force F_d and the elastic force. If F_d is constant with speed, the motion equation for the *Slip* phase is:

$$M\ddot{x} = F_d - kx(t) \tag{2.6}$$

$$\begin{cases} x(t_1) = \dfrac{CoF_s N}{k} \\ \dot{x}(t_1) = v \end{cases}$$

Solving the differential equation with the following change of variable:

$$y(t) = x(t) - \frac{F_d}{k} \tag{2.7}$$

and imposing the initial condition, the following solution is obtained:

$$x(t) = \frac{CoF_d Mg}{k} + \frac{(CoF_s - CoF_d)Mg}{k}\cos(\omega t - t_1) + \frac{v}{\omega}\sin(\omega t - t_1) \tag{2.8}$$

with $\omega^2 = \dfrac{k}{M}$. For the low sliding velocity range:

$$\frac{v}{\omega} = v\sqrt{\frac{M}{k}} << \frac{(CoF_s - CoF_d)Mg}{k} \tag{2.9}$$

The solution for the *Slip* phase can be approximated as:

$$x(t) = \frac{CoF_d Mg}{k} + \frac{(CoF_s - CoF_d)Mg}{k}\cos(\omega t - t_1) \tag{2.10}$$

The difference between the two regimes is not very significant, but in the low sliding velocity regime there is a clearer passage between the two phases. Solutions are plotted in figure 2.5.
The dynamics of the block change with increasing sliding velocity. If the speed increase the duration of *Stick* phase decrease. The duration of the *Stick* phase is $T_{Stick} = t_{end} - t_{start}$, therefore:

$$x(t_{end}) = x(t_{start}) + v \cdot (t_{end} - t_{start}) = x(t_{start}) + vT_{Stick} \tag{2.11}$$

The *Stick* phase ends when the elastic force is equal to the friction force and the *Stick* phase begins when the *Slip* phase ends. The *Slip* phase is no longer a half period of oscillation (π):

$$x(t_{end}) - x(t_{start}) = \frac{CoF_s Mg}{k} - \frac{(2CoF_d - CoF_s)Mg}{k} = \frac{2(CoF_d - CoF_s)Mg}{k} \quad (2.12)$$

Finally the duration of *Stick* phase is:

$$T_{Stick} = \frac{2(CoF_d - CoF_s)Mg}{vk} \propto \frac{1}{v} \quad (2.13)$$

If the sliding velocity increase the duration of *Stick* phase decrease. This is in accordance with common sense, for instance the squeaking sound of the door disappears if it is opened quickly.
In general, F_d can be not constant with the speed, the solution has a damping factor which makes it tend asymptotically to a stationary solution. It is possible to see it with a simple example in which F_d linearly depends on $\dot{x}$:

$$F_d = F^* - \alpha \cdot \dot{x}_{rel} \quad (2.14)$$

with F^* and α opportune constants and $\dot{x}_{rel} = \dot{x} - v$. In this case the equation 2.6 becomes:

$$M\ddot{x} = F^* - \alpha(\dot{x} - v) - kx(t) \quad (2.15)$$

that in some specified conditions could be solved by:

$$x(t) = \frac{F^* + \alpha v}{k} + e^{-\frac{t}{\tau}} A \sin(\omega t + \phi) \quad (2.16)$$

with the characteristic time $\tau = \dfrac{2M}{\alpha}$. This solution, for $t \to \infty$, tends to:

$$x(t) = \frac{F^* + \alpha v}{k} \quad (2.17)$$

2.4 Prandtl Tomlinson model

Stick-Slip phenomenon is also used at the atomic scale in order to explain the atomic friction. This is done with the Prandtl Tomlinson model in which an atom, modeled as a point mass, slides on a surface with an atomic force profile. The surface is modeled by a periodic potential, the atomic force by a spring of elastic constant k that moves at velocity v_0 (Fig. 2.7). The periodic potential $V(x)$ has amplitude N and periodicity a. The point being damped proportional to its velocity by a damping factor η:

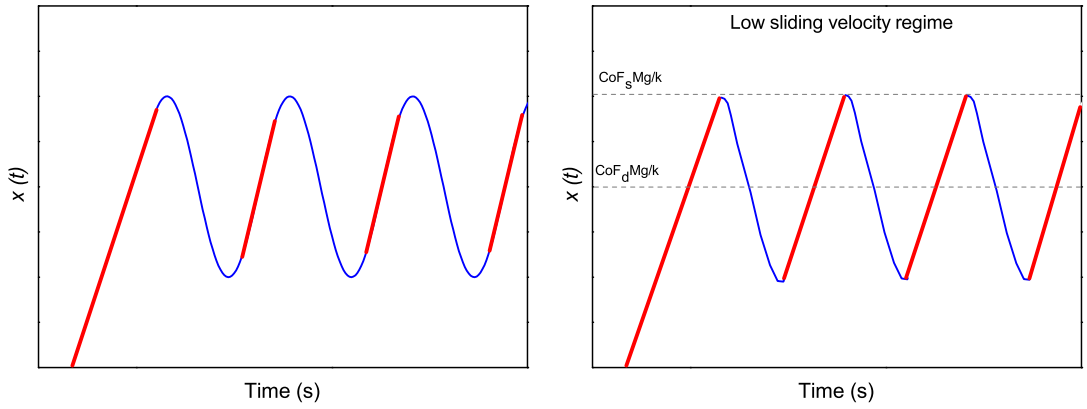

Figure 2.5: Solution of *Stick-Slip* model. In red the stick phase, in blue the slip phase [10]. The left graph shows the general solution.

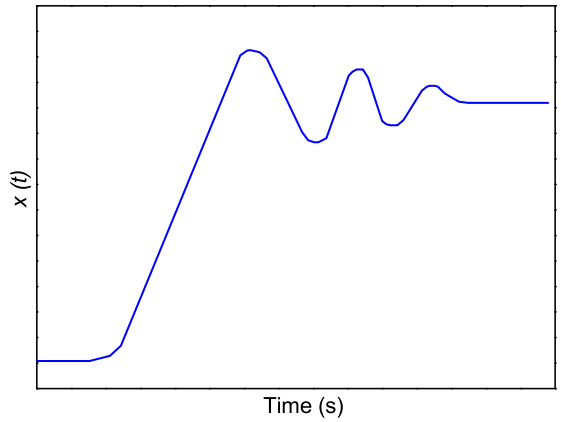

Figure 2.6: Damped solution of *Stick-Slip* model.

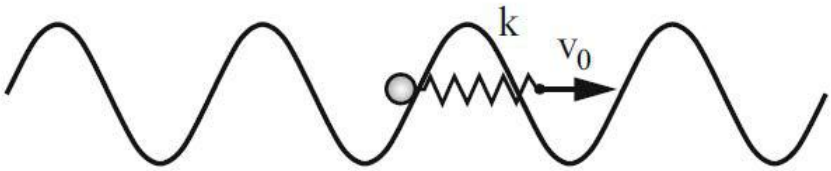

Figure 2.7: Prantl Tomlinson model [11].

$$m\ddot{x} = k(v_0 t - x) - \eta\dot{x} - \frac{dV}{dx} \tag{2.18}$$

$$m\ddot{x} = k(v_0 t - x) - \eta\dot{x} - N\sin(2\pi x/a) \tag{2.19}$$

In this model there is a potential to overcome in order to start the movement. This could be connected to the static friction force necessary to start the motion. The dynamic friction force could instead be linked to the damping velocity factor. Without the potential there will not to be the static friction force, without the damping factor there will not to be the dynamic friction force [11]. This model describes many properties of dry friction. Prandtl Tomlinson model can describe the tip movements of the atomic force microscope on a smooth surface.

2.5 Multiscale friction

Friction force is generated from different mechanisms that act on diverse scales (Fig. 2.8). All this mechanisms are dissipative process and often the total effect can be described by CoF. The most important mechanisms of friction are adhesion of the surfaces, plastic and elastic deformation, wear of surface, wetting, third body effect (Fig. 2.9, [16]). If this process results in a linear dependence of friction force upon normal force, the use of the single constant parameter CoF is allowed. Even if these processes are not linear, they can be approximated as linear, assuming small parameters in the system; linearity of the friction is a consequence of the interface forces being small compared to the binding forces acting in the bulk of the body [12].

The phenomena that govern friction depend on the sliding speed (Fig. 2.10). Macroscopic friction experiments are difficult to analyse in terms of a universal theory. In recent years a lot of work has been done in studying Hertzian contact (Fig. 2.13), studying the single behavior of an asperity. The macroscopic system is described using a statistical approach of the asperity interaction [5].

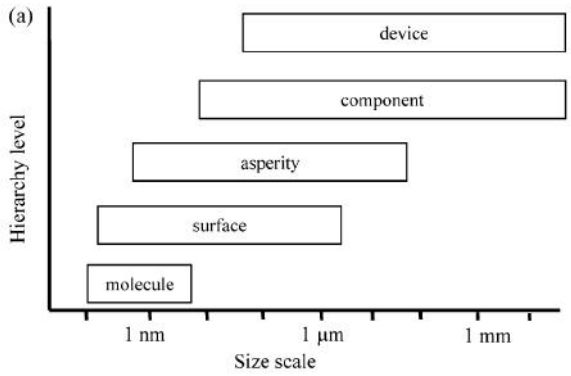

Figure 2.8: Hierarchy of friction force [12].

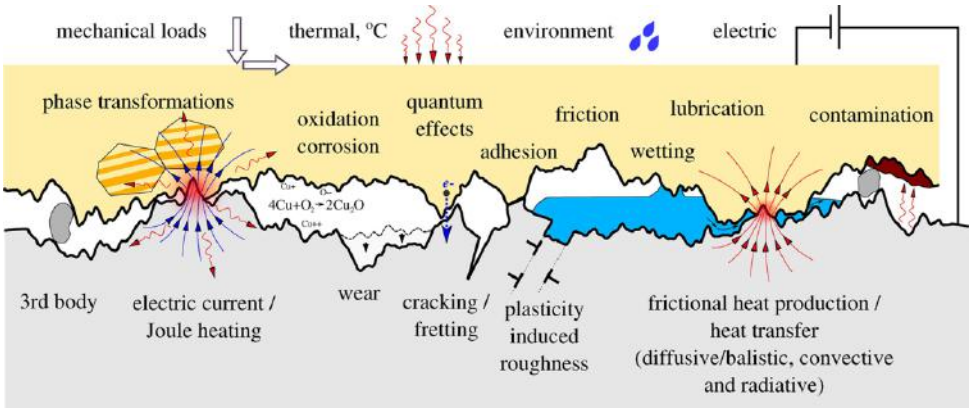

Figure 2.9: Friction force mechanisms [14]. All these chemical-physical phenomena are involved in the brake pads.

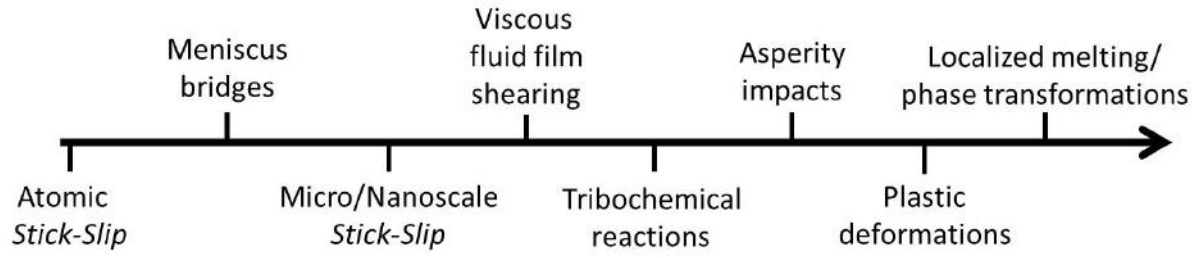

Figure 2.10: Dominant friction mechanism as a function of sliding velocity [5]. The sliding velocity increases from left to right.

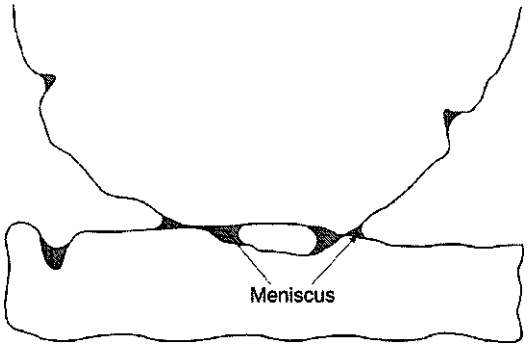

Figure 2.11: Condensation from liquid vapor on the surfaces at the interface [5].

2.6 Humidity effect on friction

A liquid that wet, as the water does, will condensate in cracks and pores on surfaces and around the contact zone if two objects are in contact; see fig. 2.11. This condensation creates adhesive bridges and menisci that could increase the adhesion between the two bodies. These adhesive forces can be split into meniscus forces due to surface tension and viscous forces [5]. The increase of adhesion is translated in an increase of friction force, especially for the static one. This increases the difference between static and dynamic CoF and then, as described above in this chapter, the probability of *Stick-Slip* events. As shown in figure 2.12, there are different regimes of humidity. In the first three the adhesion increases because of the increase of water adhesion forces. In the fourth a thick film of water is present and it serves as lubricant and the friction force decreases (aquaplaning effect).

2.7 Topographic effect on friction

When a body is sitting on a surface, not all the surface area is in contact but only a part of it due to the fact that the surface is not really flat but has asperities. Area in contact is called real area of contact (Fig. 2.13). An increase of the real area of contact generally corresponds linearly to a increase of friction force due to the formation of stronger bonds. The real area of contact can be also approximated to depend linearly on normal force [12]. From these considerations and from the Eq.2.1 the CoF is independent of the normal load. Not only the amount of the real area of contact matters, but also its conformation, which can be quantified as the average slope of the asperities. In fact to start the motion, from the balance of the forces on the inclined plane with an angle θ from the floor, a tangential force equal to

$$F_T = F_N \cdot \tan\theta \tag{2.20}$$

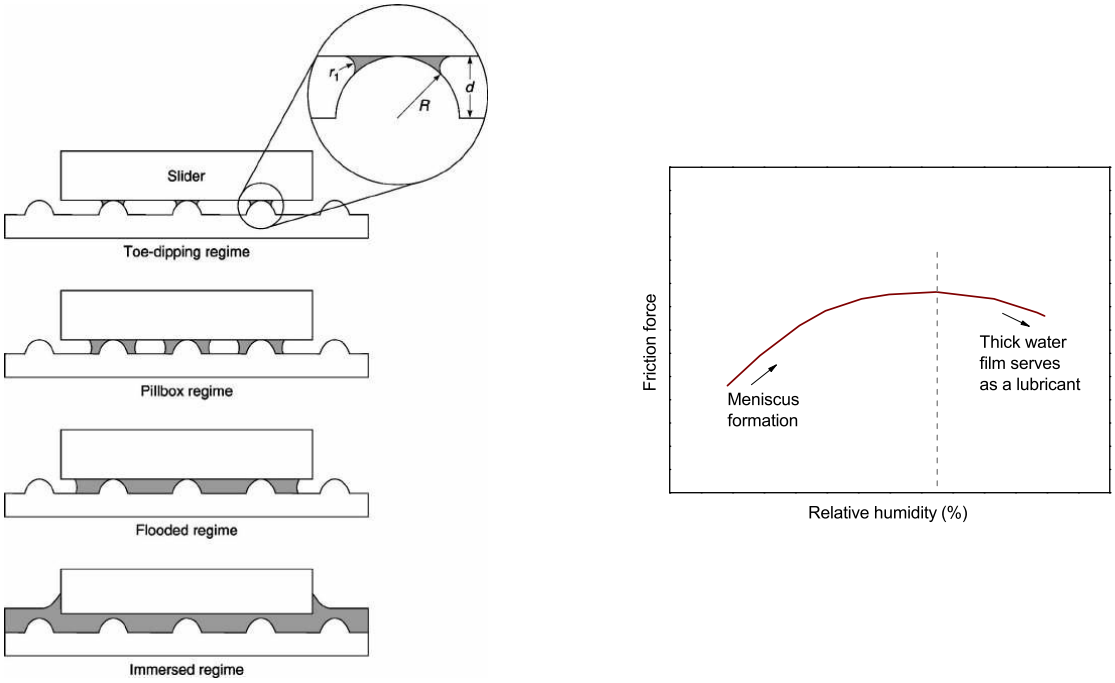

Figure 2.12: Different regimes of humidity. [5]

is necessary. From this equation and from 2.1 it may be concluded that

$$CoF = |\tan\theta| \tag{2.21}$$

Another effect can be liked to the asperities conformation. This is also linked to the presence of humidity. In fact, if the real area of contact is the same, the number N, the mean peak radius R_p and the peak-height distribution $p(z)$ can influence the menisci formation and force and so the friction force [5]. In particular for a rough surface in contact with a smooth surface, the total menisci force F_m is given as

$$F_m = 2\pi R_p \gamma_l (1 + cos\theta) N \int_{d-h}^{\infty} p(z) dz \tag{2.22}$$

where γ_l is the liquid surface tension, θ the angle contact for the liquid, h the liquid film thickness and d the interplanar separation. The maximum meniscus force is:

$$F_m = 2\pi R_p \gamma_l (1 + cos\theta) N \tag{2.23}$$

setting h to a very large value. The surface parameters can be measured with the optical 3D profilometer. The Skewness and Kurtosis impact on meniscus force. For instance, Bharat Bhushan [13] demonstrates that the meniscus force is high if the Kurtosis is equal 3 and the Skewness is lower than zero (see appendix A).
Another topographic influence is linked to the presence of grooves on the surface [15].

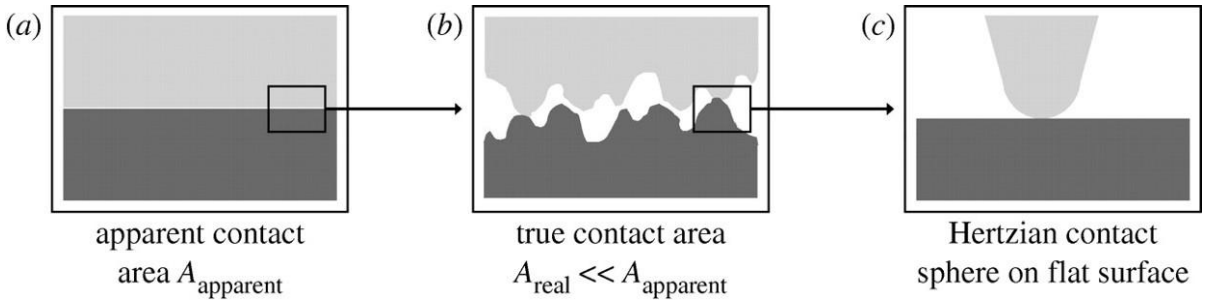

Figure 2.13: Apparent and real area of contact [16].

This is explained as follows: a friction induced torque makes the pressure distribution between the contact surface not uniform and this effect is more present in presence of grooves. But the real contact area has not a linear dependence on the pressure, specially at high pressure, as shown in figure 2.14. But since the CoF depends on the real contact area, a grooved surface has a minor CoF than a flat surface.

2.8 Surface of brake pad

Surface of a brake pad is very complex. Its complexity is due to the significant amount of different raw materials with different mechanical properties. During a brake not all the surface is in contact but only a small part of it. This part is named plateau of contact. There are two different kinds of plateaux of contact, the primary and the secondary. The former are composed by fibers and are hard and resistant. Their formation is linked to their hardness, in fact they are the pad parts that wear less. The latters indeed are composed by compacted debris, and are situated before of the primary. The debris compact due to the high pressure and temperature that allows compaction and sintering [17]. Around this plateau there are other debris that are not involved in the brake. Figure 2.15 shows an image of the pad surface done with the scanning electron microscope. Figure 2.16 shows a schematic of plateau formation.
The presence of plateau with different chemical composition and zone of no contact creates a brake pad surface with high dispersion of friction coefficient. This could be one cause of CoF vibration and so brake noise generation as will be illustrated below.

The chemical composition and distribution of plateaux play a fundamental role in *Stick-Slip*. For instance, the iron and iron oxide, present on the contact point, generates friction instability. The different chemical species that are formed have different propensities to *Stick-Slip*. H.J. Noh, H. Jang [18] demonstrated that ferrous debris and iron oxide increase *Stick-Slip* amplitude and velocity range for friction instability. In literature there are several simulations on the distribution of the contact plateaux, the numerical analysis [19] shows that the brake pad surface with few huge plateaux produce

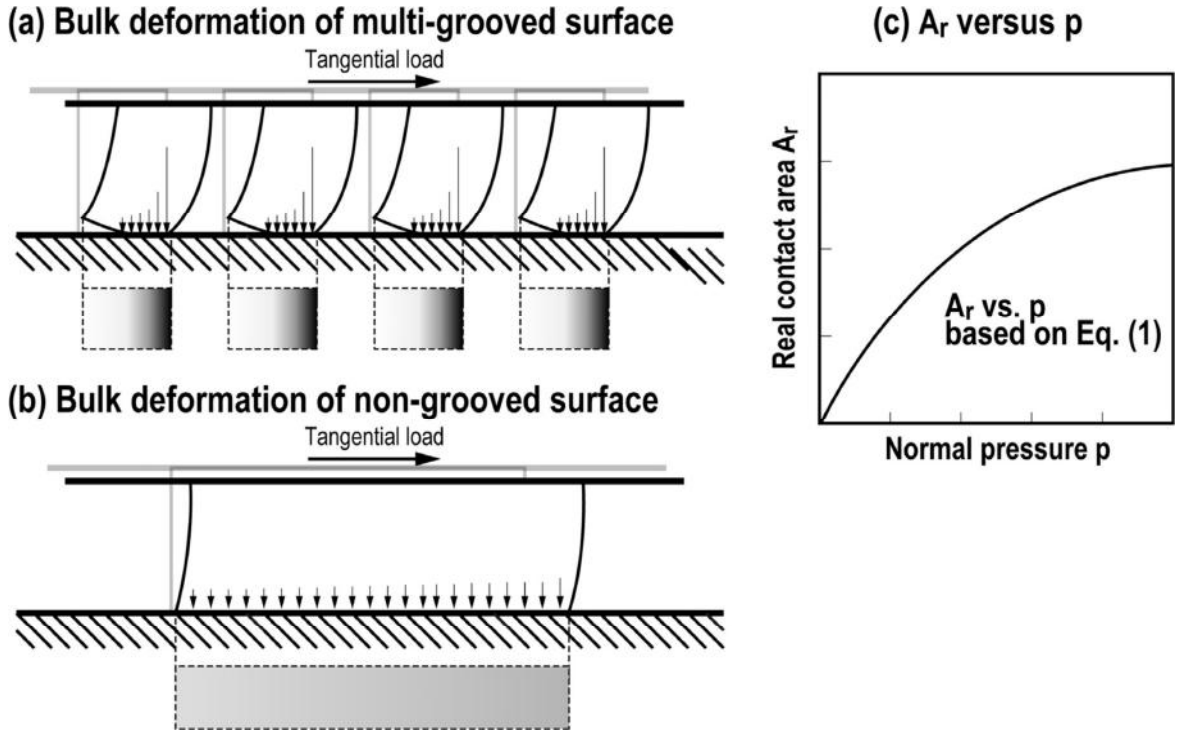

Figure 2.14: Pressure distribution on grooved (a) and not grooved (b) surfaces and contact area dependence on pressure (c) [15].

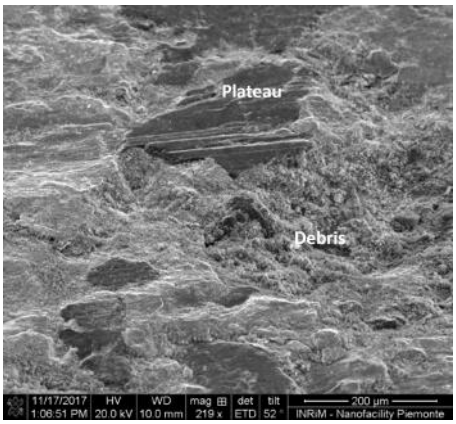

Figure 2.15: Contact plateau and debris view with SEM.

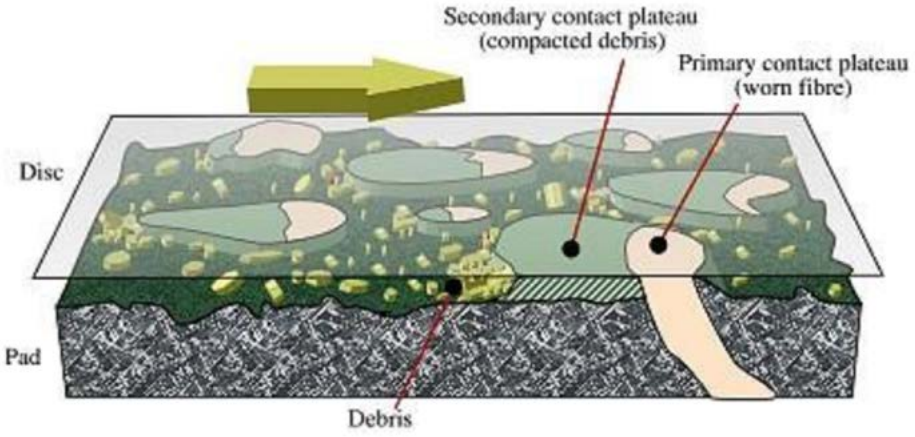

Figure 2.16: Schematic of contact plateaux formation and debris [17].

larger *Stick-Slip* amplitude than one with several tiny contact areas.

2.8.1 Surface energy of brake pad

The surface of a brake pad is complicated and chaotic. A simple model is proposed which describes the potential energy on the surface at the microscale. Let us suppose that a ball runs on the one-dimensional surface of the brake pad, it will have to overcome valleys of different heights, slopes and chemical compositions. Once a representative area of the surface has been chosen, it can be imagined that it will be repeated over the whole surface of the brake pad.

The energy for low sliding velocity is:

$$E(x) = \sum_{i,j=0}^{n} A_{ij} B_{ij} cos(\omega_i x) sin(\omega_j x) \tag{2.24}$$

A_{ij} is a roughness parameter and B_{ij} is a parameter of the chemical species on the surface and ω is the frequency; n grows exponentially with the number of raw materials inside the mix. Let us suppose that that the ball moves at a constant speed along the x axis, when it is in a relative minimum it has to overcome an energy barrier ΔE in order to run on the surface. The force to maintain constant speed will have *Stick-Slip* phases with different amplitudes. Different mixtures will have an energy that will produce more or less vibration of the force and therefore more or less propensity to mechanical vibration. By changing the chemistry and morphology of raw materials, parameters A_{ij}, B_{ij} and ω are modified. Asperities can be symmetric and asymmetric. Temperature and humidity

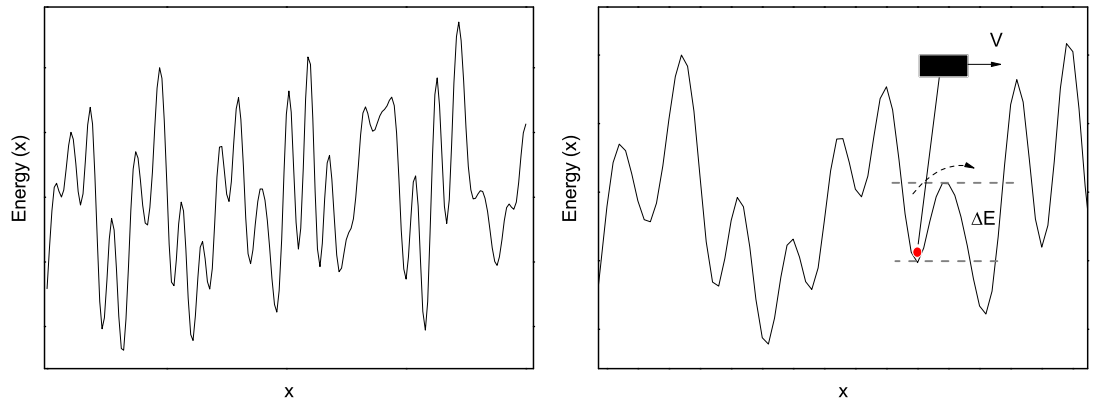

Figure 2.17: Model of energy surface of brake pad.

can strongly change the energy barrier ΔE of individual peaks.
The real world is much more complex, as it is not a ball to flow but an entire surface. Therefore, there are the energy functions for the two surfaces; parameters A and B respectively will take into account the mutual roughness and chemical affinity between the two surfaces. Three-dimensionality makes the problem even more complicated.

2.9 Linear stationary system

The effect of a linear stationary system on an input signal $x(t)$ is described by the impulsive response $h(t)$. The output signal $y(t)$ of the system is described by:

$$y(t) = f(t) \otimes h(t) = \int_{-\infty}^{+\infty} f(\tau)h(t-\tau)d\tau \tag{2.25}$$

This system can be studied in the frequency domain with the use of the Fourier transform. Calling $X(\omega)$ the Fourier transform of $x(t)$ and $H(\omega)$, called transfer function, the one of $h(t)$, the output $Y(\omega)$ in the frequency domain can be written as:

$$Y(\omega) = X(\omega) \cdot H(\omega) \tag{2.26}$$

If there are two systems with output functions $Y(\omega)$ and $Z(\omega)$ and two constant input signals X_1 and X_2 such that

$$X_1 > X_2 \tag{2.27}$$

the four relative output signals $Y_1(\omega)$, $Y_2(\omega)$, $Z_1(\omega)$ and $Z_2(\omega)$ are such that

$$Y_1(\omega) > Y_2(\omega) \quad \forall\omega \tag{2.28}$$

$$Z_1(\omega) > Z_2(\omega) \quad \forall\omega \tag{2.29}$$

With constant inputs, in order to sort form the greater to the lower the relative outputs of different linear stationary systems, it is sufficient to sort the outputs of one.
Different friction materials, in presence of *Stick-Slip* phenomenon, generate different vibrations (input signals). Assuming that these input signals are constant in the frequency domain, in order to sort the materials according to the propensity to produce an high output vibration on all the systems, it is sufficient to study only one system. Tribometer, chassis dynamometer and vehicle are assumed to be linear stationary system and so the materials studied are comparable with diverse instrumentation.

Chapter 3

Theoretical outline on noise propagation

3.1 Polymers

Polymers [20] ("*polymer*" many units, from Greek) are high molecular weight macromolecules made up of repeating monomers. They consist of a carbonaceous skeleton in which the carbon atoms are joined together by covalent bonds and the functional groups are linked to the main chain. Polymers are characterized by ramifications and cross-links[1], between the macromolecules there may be chemical bonds (cross-linked) and/or physical bonds (*e*ntangled); chemical bonds have higher energies [21], for example the bond energy of a single carbon-carbon covalent bond is 330 kJ/mol. Physical bonds are of different nature, they can be hydrogen bonds (30-40 kJ/mol), dipole-dipole bonds (10-20 kJ/mol, present in polar molecules that do not have hydrogen bonds), induction forces and London dispersion forces (1 kJ/mol, there are no permanent dipoles). They organize themselves into linear, branched, crosslinked and entangled structures.

[1] A polymer is said to be crosslinked if there are at least two different paths to connect any two points of its macromolecule.

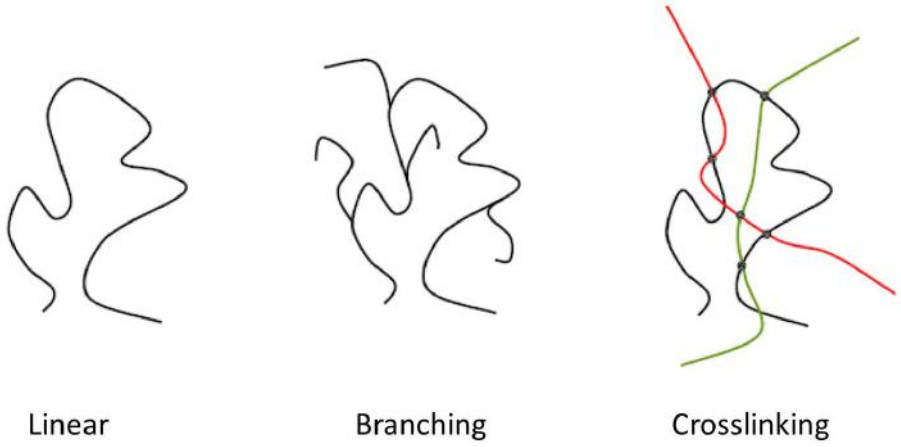

Figure 3.1: Polymer architecture, it strongly influences the characteristics of the material [21].

Polymers can be divided into the following classes:

- **Thermoplastics**, they have physical bonds and are not crosslinked, increasing the temperature it is possible to deform their structure (reversible process) and bring them to a viscous behavior. They are found both in ordered crystal structures and in amorphous unordered structures.
- **Thermoset**, they have chemical bonds and are therefore crosslinked (1 cross-link for 20 atoms in the chain), increasing the temperature they are melted without breaking the chemical bonds, the high crosslinking makes the mobility of the macromolecule very low. They are present only in a disordered and amorphous structure.
- **Elastomers**, they have chemical bonds but a less crosslinked structure than thermosets (1 cross-link per 1000 atoms in the chain). They have an amorphous structure. The elastomers are still divided into two subclasses, thermoplastic or thermosetting elastomers.

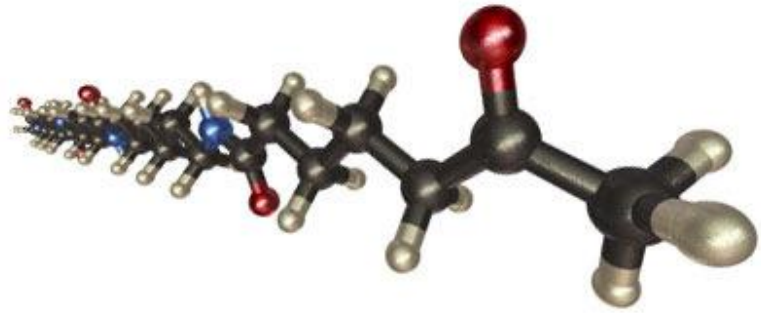

Figure 3.2: Representation of a macromolecule, the figure shows carbon atoms in dark gray, hydrogen atoms in light gray and other colors for different functional groups [30].

3.1.1 Mechanical properties

The mechanical properties [21] at a certain temperature depend on the molecular mass, degree of crystallinity, ramifications and crosslinking. The mechanical characteristics are used to ensure the performance, durability and safety of a material. The following is a list of the definitions of the fundamental mechanical properties of a material:

- **Normal strain**, following a stress σ a strain ε of the material is obtained:

$$\sigma = \frac{F}{A} \tag{3.1}$$

  F is the normal force.

$$\varepsilon = \frac{\Delta l}{l_0} \tag{3.2}$$

  Δl is the elongation and l_0 is the initial length.

$$\sigma = E\varepsilon \tag{3.3}$$

  The ratio between stress and strain is the **Young's modulus** E (also known as Elastic modulus).

- **Shear strain**, where the force F is applied parallel to the surface:

$$T = \frac{F}{A} \tag{3.4}$$

  T is the stress, meanwhile the strain is defined as follows (Fig. 3.3):

$$\gamma = \frac{\delta}{l_0} \tag{3.5}$$

the stiffness modulus G is:

$$T = \frac{G}{\gamma} \tag{3.6}$$

- **Poisson's ratio (ν)**, it is defined as the negative of the ratio of the lateral strain to the axial strain for a uniaxial stress state [21].

$$\begin{aligned} E &= 2(1+\nu)G \\ \nu &= -\frac{\varepsilon}{\gamma} \end{aligned} \tag{3.7}$$

Poisson's ratio is dimensionless and usually $0 < \nu < 0.5$.

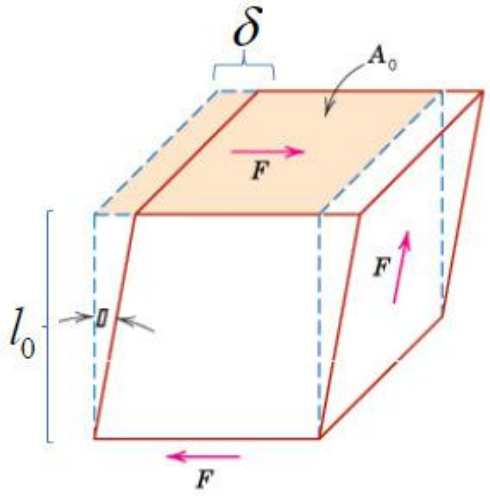

Figure 3.3: Shear strain [21], l_0 is the initial length and F is the parallel force.

- **Torsional strain**, a torque M is applied and the torsion modulus C is evaluated:

$$M = C\phi \tag{3.8}$$

ϕ is the rotation angle.

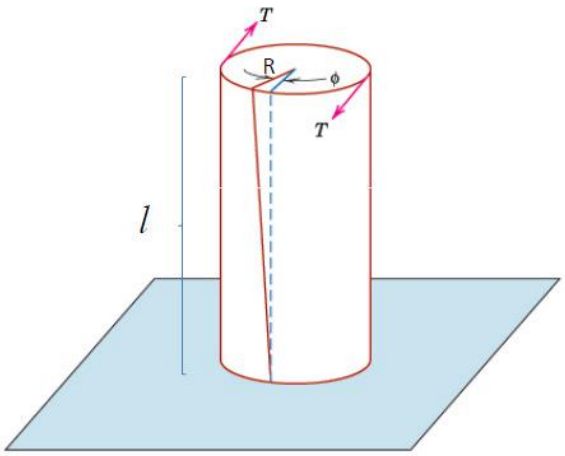

Figure 3.4: Torsional strain [21].

In the real solids the reversible deformation zone may not be linear, Young's modulus is therefore not constant. Deformations can be **elastic** (reversible) or **plastic** (irreversible). Elasticity is described by Hooke's law, while for plasticity the concept of **viscosity**[2] is introduced. For viscous liquids:

$$\begin{aligned} T &= \frac{F}{A} && \textit{shear stress} \\ \Gamma &= \frac{\Delta x}{\Delta y} && \textit{shear} \\ \frac{d\Gamma}{dt} &= \frac{d}{dt}\left(\frac{dx}{dy}\right) = \frac{dx}{dt}\frac{1}{dy} = \frac{dv}{dy} && \textit{shear rate} \end{aligned} \tag{3.9}$$

stress and strain follow Newton's law:

$$T = \eta \frac{dv}{dt} = \eta \frac{d\Gamma}{dt} \tag{3.10}$$

the shear stress is proportional to the deformation speed according to the dynamic viscosity of the fluid (η). The fluids that follow Newton's law (eq. 3.10) are called Newtonian fluids, while for non-Newtonian fluids the viscosity depends on the deformation speed $\eta = f\left(\frac{d\Gamma}{dt}\right)$.

[2]Resistance of a fluid to flow.

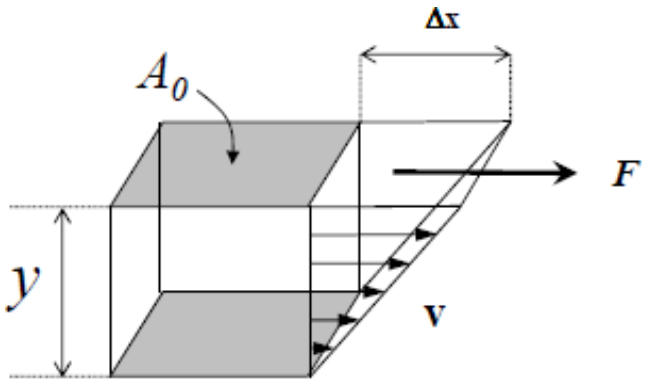

Figure 3.5: Schematic representation of viscosity. The adjacent fluid layers flow between them [21].

3.1.2 Material states and transition regions

Polymers exhibit three different behaviors [20]:

- **Elastic**, instantaneous and completely reversible process;
- **Viscous**, time-dependent and irreversible process;
- **Viscoelastic**, time-dependent but reversible process.

If the material is subject to a stress the elastic behavior consists of a change in the atomic distance and a change in the instantaneous bond angles, once the stress is removed it immediately returns to the equilibrium condition; the viscous material instead, after removing the load, returns more slowly to its initial state. Viscoelastic behavior is a combination of the two behaviors, when the load is removed there is a relaxation time (τ) in which the material returns to its initial state. The properties of the polymer [28] are defined on the basis of the temperature dependence, the main states in which the material can be found are the **glassy state**, **rubbery** and the **liquid** state or **melted**. The glassy state is characterized by high elastic modules and high fragility, does not allow for contortion and rotation movements between the segments of the molecules, there is sufficient energy only for vibrations of the atoms around the equilibrium positions, the rubbery state, on the other hand, is characterized by high viscosity. There is a transition between two different states, the transition from elastic to rubbery is called **glass transition**, a transition of a kinetic nature [21], linked at the case in which rotational and translational movements of the macro molecule occur. Figure 3.7 shows the different phases of the polymer expressed in a variation of the elastic modulus as a function of temperature; the transitions can be described in terms of free volume, below T_g the free volume is assumed to be constant) which is connected to the

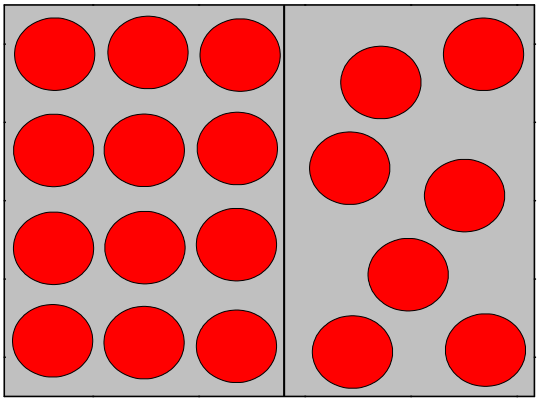

Figure 3.6: The free volume is highlighted in gray, decreasing the temperature the free volume decreases until it reaches the glass transition below which it is constant. The occupied volume (in red) represents the space occupied by atoms, also taking into account vibrations and interactions. The image on the left represents a crystalline solid, characterized by less free volume (less possibility of movement and therefore greater elastic modules), on the right an amorphous solid with greater free volume.

molecular mobility, the amorphous systems are characterized by a fraction of free volume that allows molecular motions.

Starting from low temperatures and increasing the temperature there is *gamma* transition, which makes possible localized movements (curvature and elongation of the bonds), further increasing the temperature there is the β transition where groups of atoms in the chain main can move; reached the glass transition temperature (T_g) many segments can move, it is dependent on the molecular weight, the T_g marks an important transition for the physical characteristics of the material. Then there is the rubbery zone, i.e. with high viscosity, then reaching the melting temperature of the polymer (T_m). At low temperatures the material is characterized by an elastic type behavior, as the temperature increases it has a more viscous behavior, the transition between the two states is not clear. The module that describes the viscous part of the polymer has a peak around the glass transition.

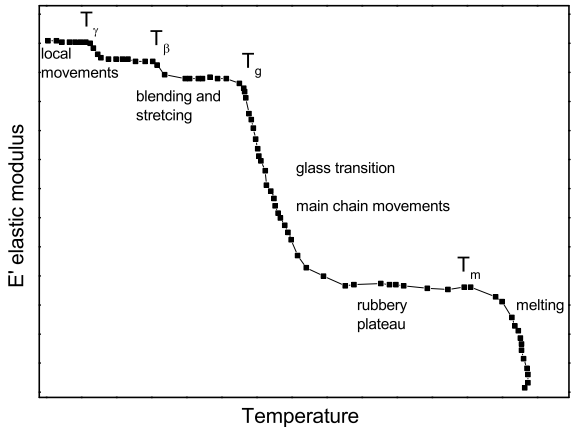

Figure 3.7: Theoretical variation of the elastic modulus as a function of the temperature in a polymer [28].

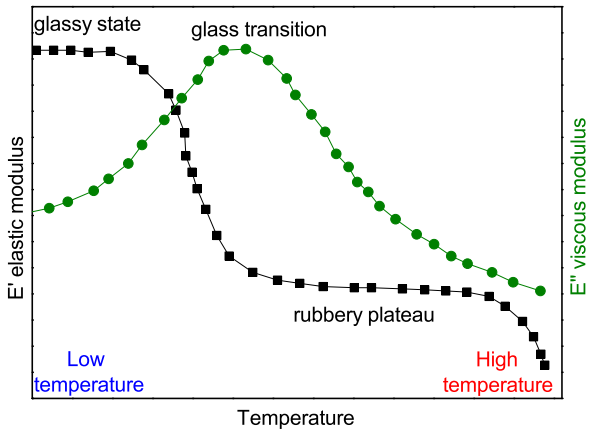

Figure 3.8: Theoretical variation of the elastic and viscous modulus as a function of temperature in a polymer [28].

3.2 Equation of Williams-Landel-Ferry

3.2.1 Maxwell model for polymers

The WLF equation [29] (Williams-Landel-Ferry) describes a well-known phenomenon in polymers, their behavior as a function of temperature and frequency: **Time-Temperature superposition**. The simplest viscoelastic model consists of a spring and a shock absorber (it contains an ideal fluid with viscosity η). The spring describes the elastic behavior while the shock absorber describes the viscous behavior of the material.

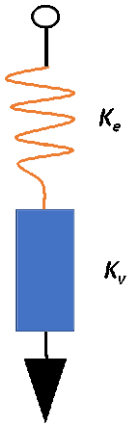

Figure 3.9: Maxwell model, it consists of a spring and shock absorber in series.

The force applied to the system (time dependent) is the same for both the spring and the shock absorber:

$$F = K_e X_e = K_v \frac{dX_v}{dt} \tag{3.11}$$

K_e and K_v are the elastic and viscose constants, respectively, X_e and X_v are the movement of the spring and the shock absorber; the total displacement X_0 is given by the sum:

$$X_0 = X_e + X_v \tag{3.12}$$

solving the equation to obtain the force as a function of time, condition $X_v = 0$ at $t = 0$:

$$\begin{aligned} K_e X_e &= K_v \frac{dX_v}{dt} \\ \frac{K_e}{K_v} dt &= \frac{dX_v}{(X_0 - X_v)} \\ \frac{(X_0 - X_v)}{X_0} &= e^{-\frac{K_e}{K_v} t} \\ F(t) &= K_e X_0 \, e^{-\frac{K_e}{K_v} t} \end{aligned} \tag{3.13}$$

the force decreases exponentially for a constant stress with a Maxwell relaxation time λ:

$$\lambda \equiv \frac{K_v}{K_e} \tag{3.14}$$

At $t = 0$ the force is equal to the force of the spring $F(t = 0) = K_e X_0$ and then it exponentially decays to zero, $F(t = \infty) = 0$.

3.2.2 Equation of Williams-Landel-Ferry

The deformation speed of the Maxwell model is given by the sum of the deformation speed of the spring and the heat sink as they are in series (the stress in the two elements is the same, but the deformation is the sum of the deformations of the two elements):

$$\begin{aligned} \gamma &= X_e + X_v \\ \left(\frac{d\gamma}{dt}\right)_{tot} &= \left(\frac{d\gamma}{dt}\right)_{molla} + \left(\frac{d\gamma}{dt}\right)_{diss} \end{aligned} \tag{3.15}$$

if Hooke's law is applied to a harmonic stress $\gamma(t)$ with frequency ω:

$$\gamma = \gamma_0 \sin(\omega t) \tag{3.16}$$

$$\left(\frac{d\gamma}{dt}\right)_{molla} = \frac{1}{E} \frac{d\sigma}{dt} \tag{3.17}$$

E is the Young's modulus, σ is the stress and γ is the strain; Newton's law which describes the energy dissipated in the strain process:

$$\left(\frac{d\gamma}{dt}\right)_{diss} = \frac{\sigma}{\eta} \tag{3.18}$$

substituting these terms in the equation 3.15, the following differential equation is obtained:

$$\left(\frac{d\gamma}{dt}\right)_{tot} = \frac{1}{E}\frac{d\sigma}{dt} + \frac{\sigma}{\eta} \tag{3.19}$$

the ratio between η and E is defined as relaxation time τ:

$$\eta\left(\frac{d\gamma}{dt}\right)_{tot} = \tau\frac{d\sigma}{dt} + \sigma \tag{3.20}$$

and solving the equation for a harmonic strain:

$$\eta\gamma_0\omega\cos(\omega t) = \tau\frac{d\sigma}{dt} + \sigma \tag{3.21}$$

the solution is:

$$\frac{\sigma}{\gamma_0} = E'\sin(\omega t) + E''\cos(\omega t) \tag{3.22}$$

by defining E' and E'' as follows:

$$\begin{aligned} E'(\omega) &= E\frac{(\tau\omega)^2}{1+(\tau\omega)^2} \\ E''(\omega) &= E\frac{\tau\omega}{1+(\tau\omega)^2} \end{aligned} \tag{3.23}$$

The relationship between the viscous and elastic component is defined as phase shift:

$$tan\,\delta = \frac{E''}{E'} = \frac{1}{\tau\omega} \tag{3.24}$$

the meaning of angular phase shift δ will be clarified in the paragraph 4.9. Assuming the constant Young's modulus, the elastic modulus E' and the dissipative modulus E'' depend on the product of the relaxation time and stress frequency, this is the principle of **Time-Temperature superposition**.
The elastic modulus for a frequency ω_0 and temperature T_0 (which corresponds to a relaxation time τ_0) is equal to:

$$E'(\omega_0, T_0) = E\frac{(\tau_0\omega_0)^2}{1+(\tau_0\omega_0)^2} \tag{3.25}$$

now suppose to change the temperature T characterized by a new relaxation time τ, the material is supposed to have the same elastic modulus in correspondence to a new frequency ω:

$$\begin{aligned} \tau_0\omega_0 &= \tau\omega \\ \omega &= \omega_0\frac{\tau_0}{\tau} \equiv \frac{\omega_0}{a_T} \end{aligned} \tag{3.26}$$

once the reference temperature has been set, the parameter a_T depends only on the temperature, a_T is defined as **shift factor**. Note the dependence of a_T on temperature allows the knowledge of the dependence of the rheological parameters of the polymer, the WLF equation [32] describes this dependence:

$$\log a_T = -\frac{C_1(T - T_0)}{C_2 + (T - T_0)} \tag{3.27}$$

C_1 and C_2 depend on the effects of free volume and on the coefficient of thermal expansion. The variation of a mechanical quantity obtained by varying the temperature at a fixed frequency can be obtained by varying the frequency by keeping the temperature fixed, this is the **Time-Temperature superposition**. To derive the WLF equation, the exponential dependence between viscosity and the fraction of free volume is assumed (Doolittle equation [33]):

$$\begin{aligned} \eta &= A\exp\left[B\left(\frac{1}{f(T)} - 1\right)\right] \\ \ln\eta &= \ln A + B\left(\frac{1}{f(T)} - 1\right) \end{aligned} \tag{3.28}$$

A and B are constants and $f = \dfrac{V_f}{V}$, V_f is the free volume of the system and V is the total volume; taking as reference the glass transition temperature[3] T_g the volume fraction can be written as a linear relationship:

$$f = f_g + \alpha_f(T - T_g) \tag{3.29}$$

f_g is the fraction of the free volume at the glass transition temperature and α_f is the thermal expansion coefficient of the free volume; replacing the expression of $f(T)$ in the equation 3.28:

[3]Below the temperature of the glass transition an amorphous material acts as a glass solid, the energy involved allows the movements of the atoms around equilibrium positions and movements of a few atoms in the main chain.

$$\begin{aligned} \ln \eta(T) &= \ln A + B\left[\frac{1}{f_g + \alpha_f(T - T_g)} - 1\right] \qquad T > T_g \\ \ln \eta(T_g) &= \ln A + B\left[\frac{1}{f_g} - 1\right] \qquad\qquad T = T_g \end{aligned} \tag{3.30}$$

subtracting the two equations and replacing the natural logarithm with the decimal one:

$$\log \frac{\eta(T)}{\eta(T_g)} = \frac{-B/2.303 f_g(T - T_g)}{(f_g/\alpha_f) + (T - T_g)} \tag{3.31}$$

The TTS principle is valid for thermoreologically simple materials. In this case, it is assumed that a variation in temperature corresponds to a variation equal to the same factor, of all relaxation times τ_i or that all relaxation times of the same system have the same temperature dependence. The relaxation times τ_i at the temperature T_0 are translated by the same factor of *shift* considering a temperature T.

$$\tau_i(T) = a_T \tau_i(T_0) \tag{3.32}$$

the Rouse model [22] schematizes the polymer with masses (viscose component) and springs (elastic component) placed in series, the modules are translated by a factor:

$$E'(T) = E'(T_0)\frac{T_0 \varrho_0}{T \varrho}$$

$$a_T = \frac{\eta T_0 \varrho_0}{\eta_0 T \varrho} \sim \frac{\eta(T)}{\eta_0(T_0)} \tag{3.33}$$

$$\log a_T = \frac{-B/2.303 f_g(T - T_g)}{(f_g/\alpha_f) + (T - T_g)}$$

ϱ is the density, ϱ_0 is the density at reference temperature T_0 and $C_1 = B/2.303 f_g$ and $C_2 = f_g/\alpha_f$, with the boundary condition $T_g = T_0$. Considering temperatures far from the glass transition of the polymer $T > T_g + 100°C$ the empirical model used is that of Arrhenius:

$$\log\ a_T = \frac{-\Delta E}{2.303 R}\left(\frac{1}{T} - \frac{1}{T_0}\right) \tag{3.34}$$

R is the universal constant of perfect gases and ΔE is the activation energy.

3.2.3 Damping of Maxwell model

Now, if a sinusoidal force is applied to the Maxwell model (Eq. 3.11):

$$F = F_0 cos(\omega t) = K_e X_e = K_v \frac{dX_v}{dt} \tag{3.35}$$

the total displacement of the system (Eq. 3.12) is the sum of the elastic and viscous part:

$$X_e = \frac{F_0}{K_e} cos(\omega t) \tag{3.36}$$

$$X_v = \int_0^{X_v} dX_v = \frac{F_0}{K_v} \int_0^t cos(\omega t) dt = \frac{F_0}{K_v} \frac{1}{\omega} sin(\omega t) \tag{3.37}$$

hence the total displacement is:

$$X_0(t, \omega) = F_0 \Big[\frac{1}{K_e} cos(\omega t) + \frac{1}{K_v \omega} sin(\omega t) \Big] \tag{3.38}$$

the second term of the equation increases the displacement between force and displacement. If the frequency increases the weight of the second term decreases.

Figure 3.10 shows an example of a theoretical calculation of force and displacement for three different frequencies. As expected, if the frequency increase the phase shift between force and displacement decrease. In the calculation all the other parameters are kept constant. If the stress frequency increases, a material intrinsically responds in a more elastic way (Eq. 3.23). The tan δ tends to zero is the frequency tends to ∞ (Fig. 3.11).

3.2.4 Time-Temperature superposition (TTS)

The mechanical behavior of the material can be studied by stressing it at different frequencies and/or at different temperatures; there is an equivalence in the frequency and temperature study. The low frequencies provide time for the material to respond and relax and therefore exhibit a viscous behavior (greater free volume), analogously at high temperatures; while the high frequencies are dominated by an elastic behavior as for low temperatures, where the polymer chains do not have time to react to the stress (see Figure 3.12).

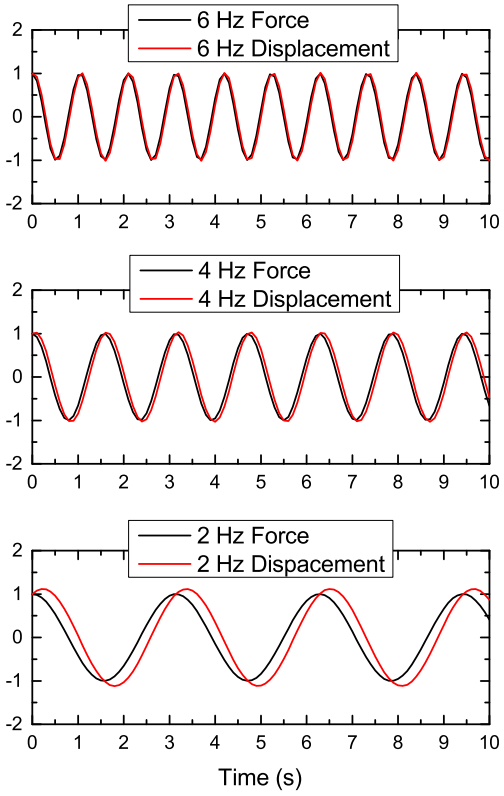

Figure 3.10: Force and displacement for different stress frequencies.

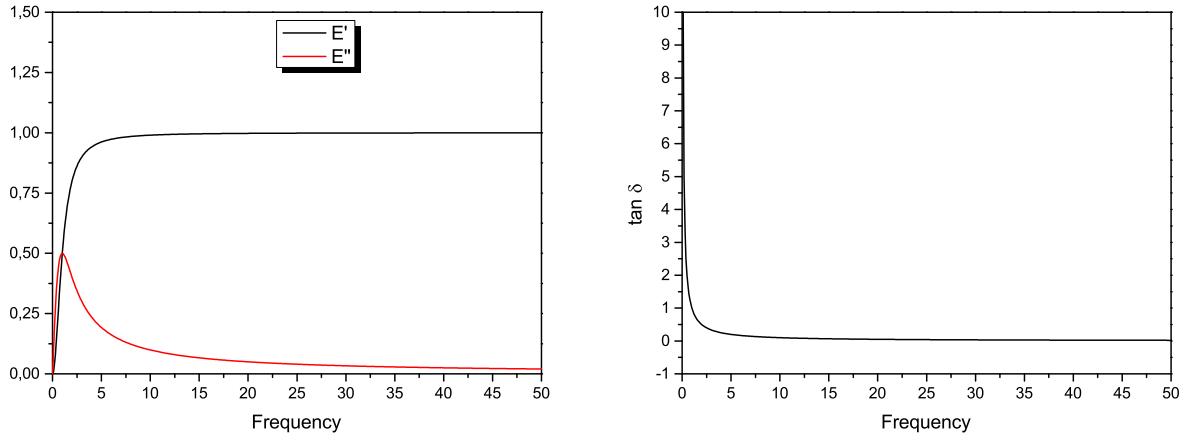

Figure 3.11: On the left, the elastic and viscous modulus as a function of frequency. On the right, the damping as a function of frequency.

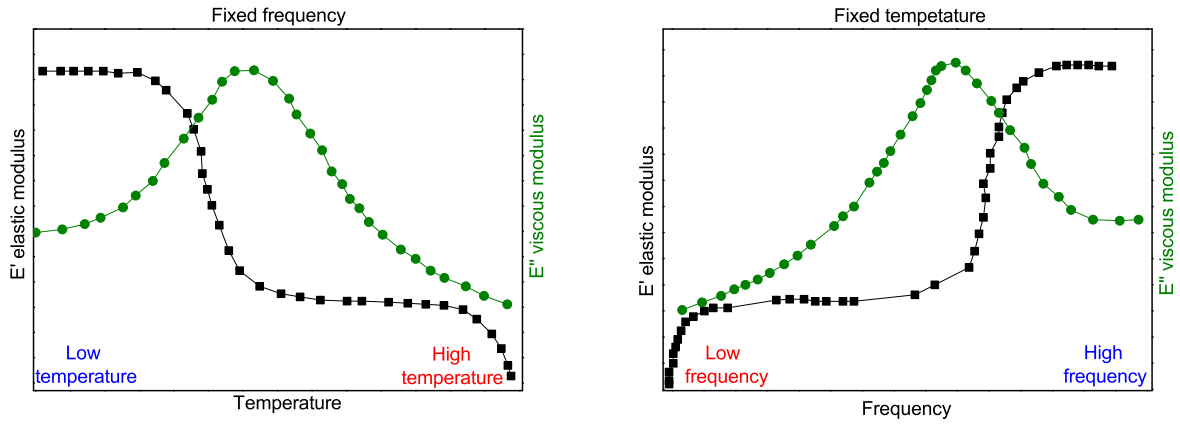

Figure 3.12: Theoretical representation of the TTS of the modules as a function of frequency and temperature.

Chapter 4

Measurements tools

4.1 Introduction

Friction force is strongly connected to the contact surface, as seen in the chapter 2. For this reason in order to understand better the friction force, a combined tribological and surface study of friction materials is an optimal choice. In order to characterize the tribology and the surface of friction materials, several tools and techniques are used. For the tribological characterization, the instruments traditionally used by ITT are vehicle and chassis dynamometer also called dyno. With these instruments the study is done on the whole or part of brake system, and not only on friction material. This is very important for the final characterization of the material before selling the final product. However these instruments have some limits. In particular the vehicle brake could not be always the same because depends on the test driver. The dyno test setup depends on the project (dyno test parameters employed for dyno tests are selected depending on the vehicle e.g. inertia), so the general behavior of brake pad can be influenced by the brake disc and brake caliper. The main tool utilized in this work is a tribometer. The tribometer is a new instrument for the ITT laboratory, and it allows to study friction material only, and to characterize it from a tribological point of view. Other advantages of using tribometer are the possibility of humidity regulation, a better instrument sensibility and a reduction of economic, energetic and time costs. This allows to do more measurements and to have a better statistics. Also the dyno has a climatic chamber (temperature and humidity regulation), but the cost is high. For a topographical characterization the instruments more utilized in brake pads studies are optical microscope, SEM, EDX, FIB and 3D optical profilometer. The synergetic application of these instruments allows the tribological features of the brake surfaces to be studied from different points of view such as the chemical composition, the height distribution, the growth of the third body layer and the morphology of the surface.
The viscoelastic characterization is done with the Dynamical mechanical and thermal

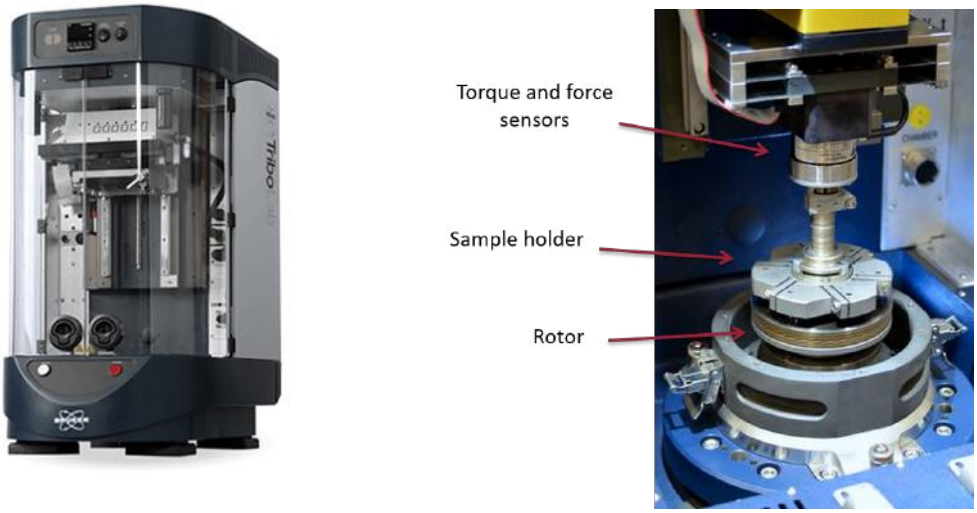

Figure 4.1: Bruker's UMT-TriboLab [23].

analysis and Frequency response function method, these techniques provide the damping properties of the materials studied as a function of temperature and stress frequency. The results will be compared with the dyno noise test results.

4.2 Tribometer

The instrument used for the tribological characterization is the tribometer. The tribometer allows the CoF to be measured at different values of normal force and sliding velocity, in different environmental condition (temperature and humidity). The one used was installed at ITT at the beginning of this thesis and then a consistent part of the work was defining a protocol of measure. The model of tribometer used is the *Bruker's UMT-TriboLab* (Fig. 4.1). The tribometer has a sample holder in which it is possible to fix samples derived directly from pads friction material. Via software it is possible to set the sample holder to apply a normal force against the disc that rotates at a specified speed. The sample holder can not rotate but only go up and down. In order to obtain the samples, friction material is detached from the pad metal back plate and then it is grinded at 7.5 mm. Then it is cut in samples of area 1x1 cm suitable for the tribometer sample holder (Fig. 4.2). The sample holder has to hold three samples of the same materials in order to better distribute the pressure. The disc is made of cast iron and it is obtained from a truck disc. From the torque measure $T_z(t)$ (dependent variable) and the normal force $F_n(t)$ (independent variable) experienced by the sample holder it is possible to calculate the CoF with the following formula:

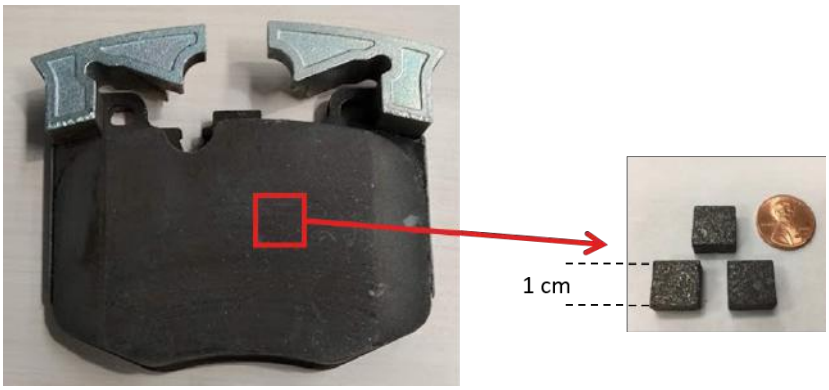

Figure 4.2: Samples for tribometer obtained from a brake pad.

Table 4.1: Bruker's UMT-TriboLab technical specification

Rotor speed min	0,01 RPM
Rotor speed max	5000 RPM
Normal force sensibility	0,01 N
Normal force max	1000 N
Torque sensibility	0,01 Nm
Torque max	11 Nm

$$CoF(t) = \frac{T_z(t)}{F_n(t) \cdot r_{eff}} \tag{4.1}$$

$$CoF(t) \propto \frac{T_z(t)}{F_n(t)} \tag{4.2}$$

where r_{eff} is the effective radius of the sample holder (Fig. 4.3).

This tribometer has the possibility to work in a climatic chamber which allows the control of the relative humidity, from 10% to 90%. This is very useful because as seen in the chapter 2 the humidity influences the CoF, especially the static one.
Torque sensor works using a Wheatstone bridge (Fig. 4.4). $R1$, $R2$ and $R3$ are resistors of known values, while Rx is a resistor that could changes its value depending on the value of the torque. A direct voltage is supplied from Vg and the output is the current measured by C. With a null torque Rx is such that the bridge is in equilibrium and the current measured is zero. In presence of a torque experienced by the sensor, Rx change its value and the bridge is not more in equilibrium. Calibrating the sensor, from the current measured in C it is possible to have a measure of the torque. The torque sensor is fixed on a shock absorber that isolates it from external vibrations. The temperature can be measured inside the friction material and on the disc with a sliding thermocouple.

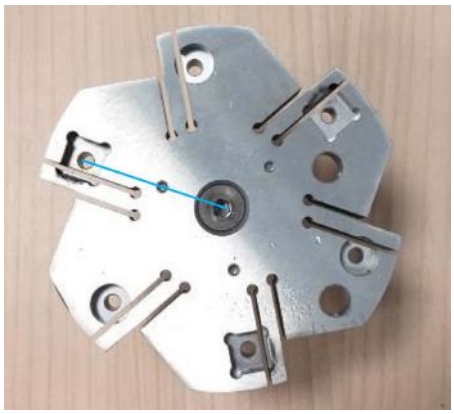

Figure 4.3: Tribometer sample holder with effective radius highlighted in blue (r_{eff} = 38.1 mm).

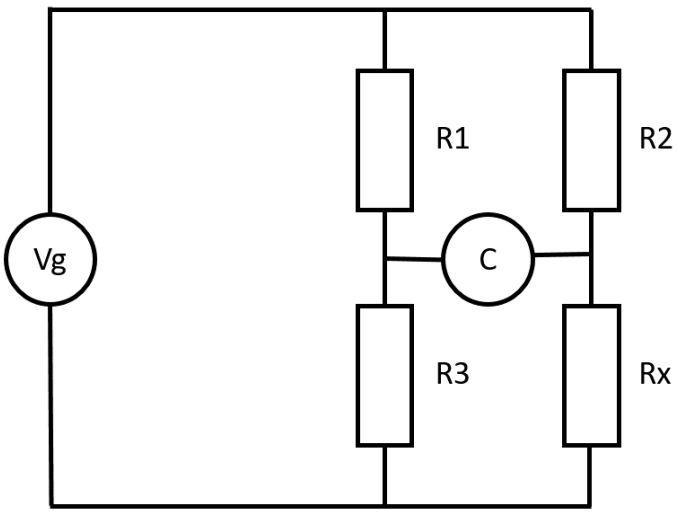

Figure 4.4: Schematic of a Wheatstone bridge.

4.3 Chassis dynamometer

Chassis dynamometer is an instrument that is used to simulate and study the vehicle during diverse brake conditions. It is composed of a brake system (brake caliper and rotor, there is no the chassis) that is equal to the one on a vehicle and the brake pads and the disc used are the same used in the particular project studied. The vehicle motor is simulated by an electric motor that is set to work at its same engine torque. The vehicle inertia is simulated by a system of flywheels that can be added in order to obtain the same inertia. The different conditions are obtained changing the environmental temperature and humidity, and there is a cooling system that simulate the cooling effect due to the real vehicle speed. The dynamometer measures the braking torque $T_b(t)$ with a torque meter and the pressure $P(t)$ inside the piston. From the equation 2.1 it is possible calculate the CoF knowing that the friction force is:

$$F_f = \frac{T_b}{r_{eff}} \tag{4.3}$$

with r_{eff} the effective radius i.e. the distance between the center of the disc and the center of the pad, and the normal force is

$$F_N = 2PA \tag{4.4}$$

with A the area of the piston and the number 2 because there are 2 brake pads per disc. The final CoF equation for the dynamometer is:

$$CoF(t) = \frac{T_b(t)}{r_{eff} 2AP(t)\eta_{caliper}} \tag{4.5}$$

$$CoF(t) \propto \frac{T_b(t)}{P(t)} \tag{4.6}$$

$\eta_{caliper}$ is the efficiency of the brake caliper, it is usually considered equal to 1. This parameter can be different to 1, this is an example of how the tribometer is an excellent tool for studying the tribological properties of the brake pad. The brake can be controlled by pressure and so the independent variable is $P(t)$ or controlled by the torque, with $T_b(t)$ as independent variable. The geometrical factors depend on the particular project. Other important parameters that can be measured, depending on the test requirement, are the pads or disc temperature with a thermocouple or a pyrometer, the noise with a microphone, acceleration with an accelerometer (Fig. 4.5). There are two kind of dynos that are used for different purpose: noise and performance test. For the *Stick-Slip* test the performace dyno is used (Figure 4.5).

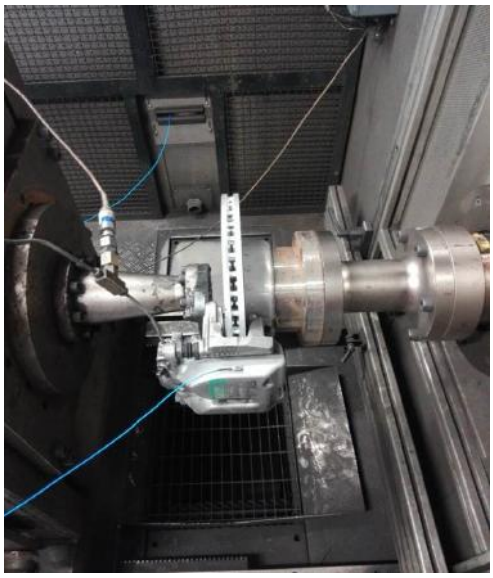

Figure 4.5: Chassis dynamometer equipped with disc, caliper, brake pad and accelerometer.

4.4 Vehicle

Tests on the vehicles provide the final validation of brake pads. The vehicles used are the same of the commercial ones, but are equipped with sensors for the brake pads characteristic evaluation (accelerometer, microphone, pressure gauge, thermocouple)(Figure 4.6). There are research and standard tests on the vehicle. The standard tests are divided into security tests (for evaluate wear tests, CoF, thermal resistance, etc.) and noise tests.

4.5 Optical 3D Profilometer

In order to study the topography of the tribological surfaces an optical 3D profilometer was used. It allows a non-invasive analysis of the surface morphology. The profilometer used exploit the Chromatic Confocal technique. This technique uses white light that passes through a series of lenses with a high degree of chromatic aberrations. In this way, the focus length will be a function of the wavelength and only at a certain distance, the object will be on focus. Thanks to the confocal system, only the focused wavelength will pass through the pin hole filter to reach the CCD spectrometer. Every different wavelength measured correspond to a vertical position (Fig. 4.7). In this way it is possible to measure the altitude of a surface point. Then with two different motors it is possible to change the position of the sample, scanning all the surface. The profilometer used is the *Nanovea PS50* [24] in figure 4.8. Profilometer technical specification are in table

Figure 4.6: Vehicle instrumentation. There is the manometer for measure the pressure, thermocouples inside the brake pad, solenoid valves to exclude the front or rear axle, fonometer, binaural headphones and SQuadriga II (accelerometer signal acquirer).

Table 4.2: Nanovea PS50 profilometer technical specification.

x and y resolution	1,6 μm
x and y scan area	$5x5$ cm
z resolution	2.5 nm
z range	300 μm

4.2. With the profilometer it is possible obtain the altimetric map of the surface, from this, it is possible obtain some important surface parameters that allows to characterize them. The parameter used in this work are the roughness (Sq), the skewness (Ssk) and the Kurtosis (Sku). These parameters could be obtained either for the whole surface or for only a particular profile. The definition of these parameter are in the appendix A. Another statistical instrument used to describe the surfaces is the Abbott-Firestone curve that is the cumulative distribution function of the heights. The software used for the data analysis of the optical 3D profilometer is the *Nanovea Professional 3D*.

4.6 SEM-EDS

A scanning electron microscope (SEM) is a microscope that produces images of a sample by scanning the surface with a focused beam of electrons. This is done scanning the whole surface with a focused electrons beam. The electrons interact with atoms producing signals that contains topography and composition information of the sample. In the most common SEM mode, the signals detected derive form the secondary

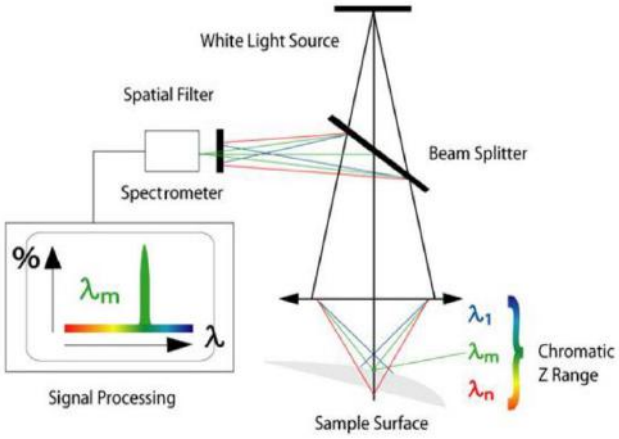

Figure 4.7: Optical 3D profilometer functioning [24].

Figure 4.8: Nanovea PS50 profilometer [24].

electrons emitted by atoms excited by the electrons beam. Another signal often used is the back-scattered electrons beam (this mode gives information on the atomic number). SEM works in high vacuum in order to increase the number of electrons detected. High vacuum is also necessary in order to not ionize the air with the high voltage necessary to create the electrons beam.
Energy-dispersive X-ray spectroscopy (EDS) is an analytic technique used for elemental analysis or chemical characterization of sample. It works with the study of the characteristic X-rays emitted by atoms in the sample. In order to stimulate the X-rays emission it is possible to use different probes, such an high energy beam of electrons, protons or X-rays. SEM often are equipped with EDS spectrometer that allows to use EDS technique with the same electrons beam used in the SEM analysis. The coupling of the two allows to chemical characterize the sample with high spatial precision. The SEM used in this work is the model LEO 1450 VP [25] and allows EDS analysis. The electrons source is a tungsten filament and the SEM chamber works around $10^{-4} : 10^{-5} bar$.

4.7 Focus ion beam

The Focus ion beam, also called FIB, is used to remove the first micrometers under the surface in order to study the morphology (SEM) and composition (EDX) of the cross section; by with this technique it is possible to investigate how primary plateau grows and know more details about the chemical composition. The third body layer thickness rarely exceeds 10 μm. The model used is the Quanta 3D [26] (INRiM nanofacility Piedmont [27]). FIB operates in a similar way to a SEM, but FIB system uses a finely focused beam of ions (gallium) that can be worked at high beam currents (from 1 to 7 nA) for site precise sputtering or at low beam currents (from 30 to 100 pA) for imaging. The chamber works around 10^{-8} bar of pressure. The sample is fixed on the stage, in the same chamber there is the FIB and SEM, the stage can be tilted 52 degrees, if the procedure of alignment is done, the FIB and SEM are focused in the same point (eucentric position). When the sample is in the eucentric position, the FIB excavation can begin, the SEM is used to monitor its evolution. Thanks to the stage inclination, it is also possible to have information on the z axis (e.g. third body layer thickness measurement).

4.8 Optical microscope

The optical microscope (OM) is a type of microscope that uses visible light and a system of lenses to magnify images of samples. It is the oldest design of microscope. Modern OM captures images with charge-coupled device (CCD) camera that allows to have digital images. Optical microscope has a resolution limit related to the nature of the probe used, the visible light. At very high magnifications point objects are seen as

fuzzy discs surrounded by diffraction rings. The *resolving power*, that is the possibility to distinguish two different structures depend on the diffraction extent and magnitude. The resolution d is defined as

$$d = \frac{\lambda}{0.61 \cdot NA} \tag{4.7}$$

where λ is the wavelength of light and NA the numerical aperture of the objective lenses. With conventional lenses d is about 200 nm. The optical microscope used for this thesis is the stereo microscope Nikon SMZ25. A stereo microscope allows the vision of surfaces in 3D.

4.9 Dynamic-mechanic and thermal analysis

Dynamic mechanical and thermal analysis (DMTA) is a technique for the characterization of materials, widely used for the study of the viscoelastic behavior of polymers. Dynamic mechanical and thermal analysis [34] consists of applying an oscillatory deformation to a specimen (forced vibration) and measuring the resulting stress due to the characteristics of the material. This technique allows the *storage modulus* to be calculated E', which represents the elastic part of the material, where the result is a completely reversible deformation, the *loss modulus* E'' is the viscous part (the energy dissipated in heat during the load) and tan δ dimensionless quantity which indicates the phase difference between *stress* σ and *strain* ε, valued as the ratio between E'' and E'. The strain applied is:

$$\gamma(t) = \gamma_0 sin(\omega t) \tag{4.8}$$

This strain generates normal stress in the material:

$$\sigma(t) = E\gamma_0 sin(\omega t) \tag{4.9}$$

E is the Young's modulus. The studied materials show both elastic and viscous behavior, a tangential stress originates, out of phase by 90°:

$$\begin{aligned} \varepsilon(t) &= \eta \frac{d\gamma(t)}{dt} = \eta\gamma_0\omega cos(\omega t) \\ \varepsilon(t) &= \eta\gamma_0\omega sin(\omega t + \frac{\pi}{2}) \end{aligned} \tag{4.10}$$

η is the viscosity. These quantities provide information at the molecular level to understand the behavior of the polymer. The physical quantity evaluated is the complex module $|E^*|$:

$$|E^*| = \frac{\sigma}{\varepsilon} \tag{4.11}$$

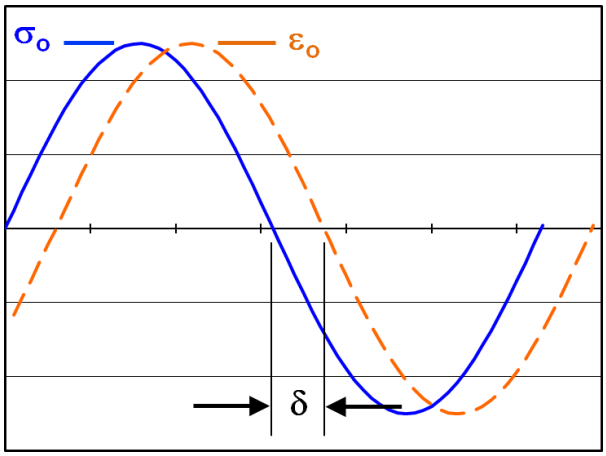

Figure 4.9: The figure shows the behavior of *stress* σ and *strain* ε. δ is their phase difference [31].

The term E^* can be considered complex thus defining a phase difference between elastic and viscous behavior (see eq. 3.24); $|E^*|$ is the root sum squared of the *storage modulus* (real part) and *loss modulus* (imaginary part):

$$|E^*| = \sqrt{E'(\omega)^2 + E''(\omega)^2} \tag{4.12}$$

$$E'(\omega) = |E^*|cos(\delta) \tag{4.13}$$

$$E''(\omega) = |E^*|sin(\delta) \tag{4.14}$$

$$tan\ \delta = \frac{E''(\omega)}{E'(\omega)} \tag{4.15}$$

If the material is perfectly elastic, the *stress* and *strain* are in phase (δ=0°), for a perfectly viscous material the phase difference is 90°. High values of tan δ meaning that the material is not elastic, instead for low values of it the material tends to be elastic.

The analysis is performed on a 3-point bending geometry, two lateral supports and the load is applied to the center; the rubbers are analyzed with the parallel plate setup. (see Fig.4.10).
The elastic and viscous modulus for a specimen with height h, length L and thickness b (three-point flexion set up) are [34]:

$$
\begin{aligned}
E' &= \left[k\ cos\ \delta + 2\pi^2\omega^2 m\right]\frac{24L^3}{bh^3\pi^4} \\
E'' &= \left[k\ sin\ \delta\right]\frac{24L^3}{bh^3\pi^4}
\end{aligned}
\tag{4.16}
$$

k is the stiffness modulus [N/m], δ is the phase angle, m is the mass of the sample [kg], ω is the stress frequency [Hz]. If the phase angle is zero, the viscous component is zero and the elastic modulus is maximum, on the contrary if the phase angle is 90° the viscous part has a maximum. The 3-point bending setup is suitable for stress frequencies up to about 50 Hz, above this frequency geometric resonance phenomena occur. The modules for the parallel plates setup for a cylindrical specimen are [34]:

$$
\begin{aligned}
E' &= kF_c(h/S_e)\ cos\ \delta \\
tan\ \delta &= \frac{E''}{E'} \\
F_c &= \frac{1}{1+2(S_e/Sl)^2} \\
S_e &= \pi(\phi/2)^2 \qquad Sl = \pi\phi h
\end{aligned}
\tag{4.17}
$$

S_e is the stressed surfaces of the sample [m^2], Sl is the lateral surface of the sample [m^2], F_c is the corrective form factor, ϕ is the specimen diameter [m].

DMTA is a technique that allows to evaluate the glass transition temperature of the polymers. The analysis can be performed at a constant stress frequency (varying the temperature), at constant temperature (varying the frequency) or a combination of the two methods. The range of temperatures that can be analyzed is from -150 to 450 °C and the range of frequencies is from 1 to 200 Hz.

The specifications of the instrument are:

Model		METRAVIB DMA+150
Temperature		-150/450 °C
Frequency		1-200 Hz
Static	Force	150 N
	Displacement	6 mm
Dynamic	Force	72 N
	Displacement	6 mm

Table 4.3: Specifications of the DMTA.

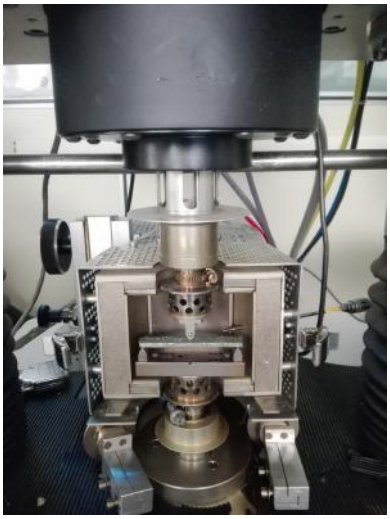

Figure 4.10: The figure shows the DMTA setup. On the left the 3-point bending set up, the oven is closed to perform temperature measurements; the temperature is acquired by a thermocouple placed near the sample. On the right the parallel flat plates setup for the measurement of rubber.

4.9.1 DMTA measurement routine

DMTA allows the behavior of materials in a wide range of frequencies to be calculated, outside of those that can be experimentally analyzed, using the time-temperature superposition principle explained in the paragraph 3.2.4. The measurement procedure takes more than 10 hours, the two preliminary phases are used to remain in the field of elastic and non-plastic deformations of the material:

- **Static analysis**: the elastic modulus is calculated for static loads from 40 to -400 μm. Once the elastic modulus has been measured, in order to remain in the elastic deformation zone, the last point in which E' is unchanged is considered, as its variation would be due only to the value of load and not to the intrinsic properties of the material;

- **Dynamic analysis**: the procedure consists in applying the static load obtained in the previous phase, and adding a dynamic load between 1 and 100 μm. Also in this case E' is obtained as a function of the dynamic load and the last value in which E' does not vary is selected. Once the static and dynamic loads have been selected such that the deformations are elastic, the next measurement phase can begin. Figure 4.11 shows an example of the E' as a function of static and dynamic displacement;

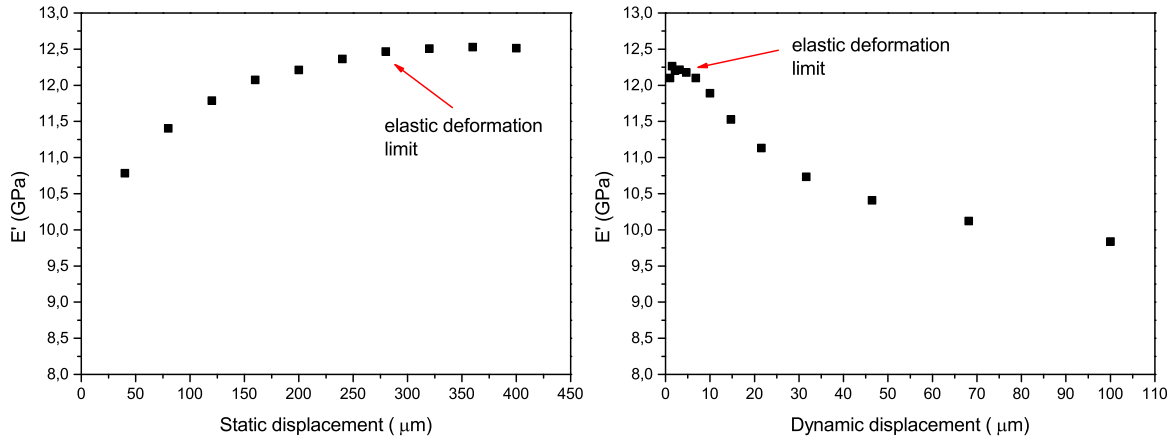

Figure 4.11: Static and dynamic analysis.

- **Temperatures ramp at different stress frequencies**: the measurement procedure starts from -60 °C up to 150 °C at step of 10 °C and the chamber conditioning time is 5 minutes. For each isotherm the elastic and viscous modulus is calculated as the stress frequency of the mechanical probe changes: 1, 1.8, 3.2, 5.8, 10.5, 18.9, 23, 34, 45, 60 Hz. The tan δ (T,ω) (damping) is obtained from the ratio of E"(T,ω) and E'(T,ω).

4.9.2 Master Curve generation

Using the principle of time-temperature superposition it is possible to study the behavior of the material in a large scale of stress frequencies. The WLF theory (see Par.3.2) allows to calculate the **shift factor**; once a reference temperature has been chosen, it is possible to translate the isotherms (of the E' and the E") into a range of frequencies that cannot be analyzed by the instrument, but which are very interesting for mechanical and acoustic vibrations. The curve obtained is the so called **master curve** (Figures 4.13 and 4.14). From the WLF theory, the *shift factor* a_T is calculated considering the elastic (or viscous) modules equal but at different temperatures and stress frequencies (Figure 4.12):

$$E^*(T_i, \omega_i) = E^*(T_j, \omega_j = a_{(T_i,T_j)} \cdot \omega_i) \tag{4.18}$$

Considering the complex modulus:

$$E^* = E'(\omega) + iE''(\omega) = |E^*|e^{i\delta(\omega)} \tag{4.19}$$

Using the Kramers-Kronig relationship that join the real and imaginary part of a complex function:

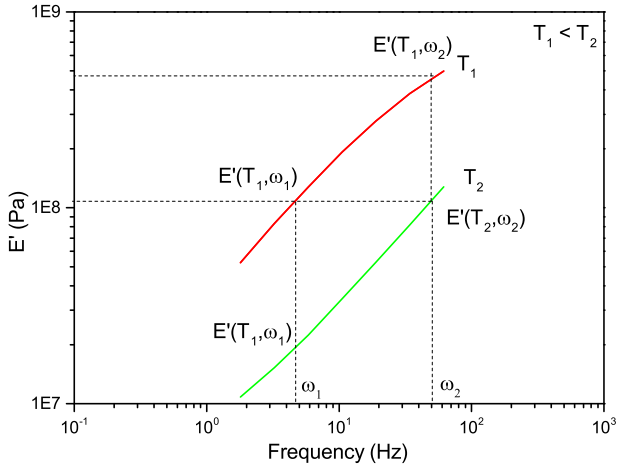

Figure 4.12: Green and red lines are the two isotherms at different stress frequencies, the selected points allow to calculate a value of δ between the two isotherms. This is the overlap zone.

$$\begin{aligned} E'(\omega) &= \frac{1}{\pi} P \int_{-\infty}^{\infty} \frac{E''(u)}{u-\omega} du \\ E''(\omega) &= -\frac{1}{\pi} P \int_{-\infty}^{\infty} \frac{E'(u)}{u-\omega} du \end{aligned} \tag{4.20}$$

P is the Cauchy principal value [35]:

$$\begin{aligned} log|E^*(\omega)| - log|E^*(\infty)| &= -\frac{2}{\pi} \int_0^{\infty} \frac{u \cdot \delta(u) - \omega \cdot \delta(\omega)}{u^2 - \omega^2} du \\ \delta(\omega) &= \frac{2\omega}{\pi} \int_0^{\infty} \frac{log|E^*(u)| - log|E^*(\omega)|}{u^2 - \omega^2} du \end{aligned} \tag{4.21}$$

simplifying the expression of $\delta(\omega)$ and verifying the result experimentally [35], it is obtained:

$$\delta(\omega) = \frac{\pi}{2} \frac{dlog(|E^*(\omega)|)}{dlog(\omega)} \tag{4.22}$$

the algorithm for evaluating a_T [36] starts by calculating, for two frequencies ω_i and ω_j, the average between the two angles measured at the two frequencies:

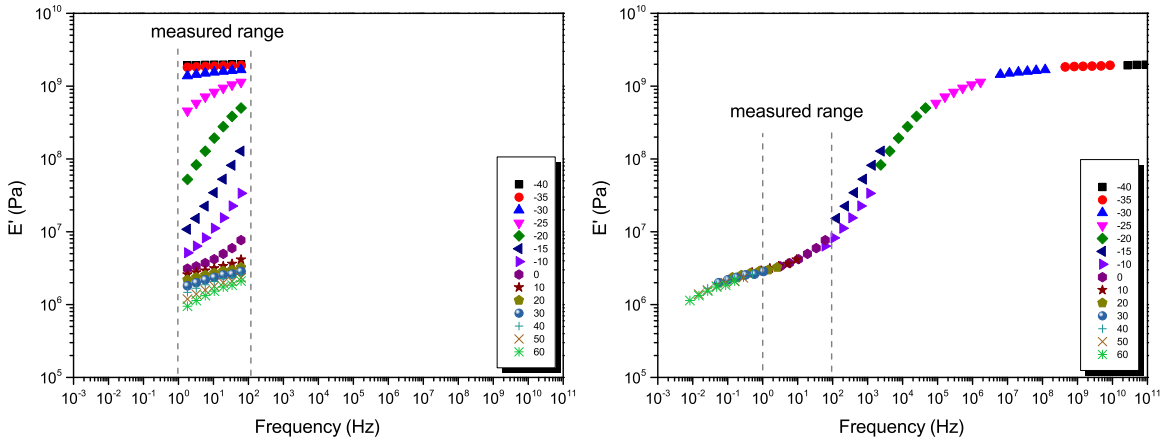

Figure 4.13: On the left, the different isotherms of the elastic modulus for the frequencies measurable by the instrument. On the right, the master curve of the isotherm of 0 °C.

$$\delta_{average}(\omega_i, \omega_j) \cdot \frac{2}{\pi} = \frac{log(|E^*(T, \omega_j)|) - log(|E^*(T, \omega_i)|)}{log(\omega_j) - log(\omega_i)} \tag{4.23}$$

The time-temperature superposition principle allows to evaluate the same quantity by keeping the frequency fixed and varying the temperature.

$$\delta^{(T_1,T_2)}_{average}(\omega_2) \cdot \frac{2}{\pi} = \frac{log(|E^*(T_1, \omega_2)|) - log(|E^*(T_2, \omega_2)|)}{log(a_{(T_1,T_2)})} \tag{4.24}$$

$a_{(T_1,T_2)} = \dfrac{\omega_2}{\omega_1}$ such that $|E^*(T_1, \omega_1)| = |E^*(T_2, \omega_2)|$. Since the measurement is performed for different isotherm $T_1, T_2, ...T_i...., T_n$, the master curve is processed respect to a T_{ref}, between 1 and n. The different shift factors for the different isotherms are evaluated, considering the isotherm T_i:

$$log(a_{(T_i,T_{ref})}) = \sum_{j=i}^{j=ref} log(a_{(T_j,T_{j+1})}) \tag{4.25}$$

finally is possible to write the following equation:

$$log(a_{(T_i,T_{ref})}) = \sum_{j=i}^{j=ref} \frac{log(|E^*(T_j, \omega)|) - log(|E^*(T_{j+1}, \omega)|)}{\delta^{(T_j,T_{j+1})}_{average}(\omega)} \cdot \frac{\pi}{2} \tag{4.26}$$

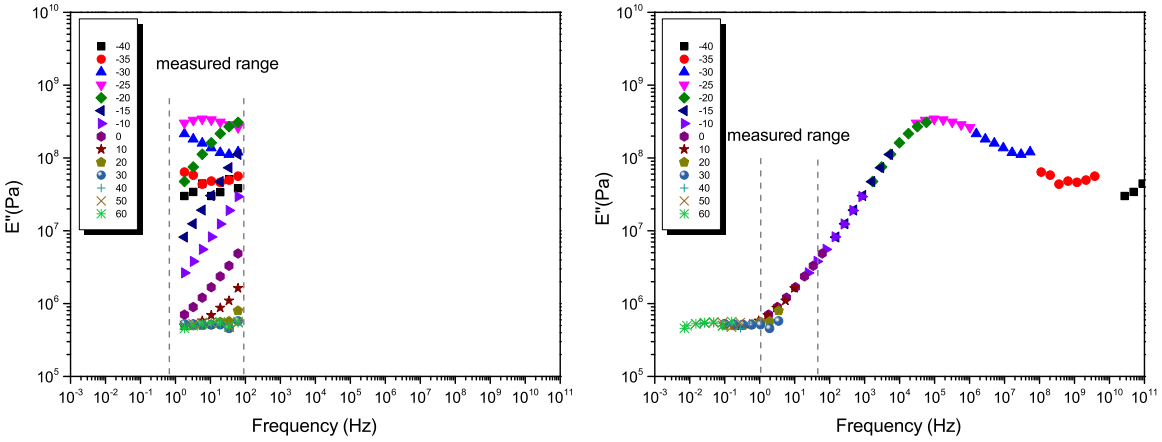

Figure 4.14: On the left, the different isotherms of the viscous modulus for the frequencies measurable by the instrument. On the right, the master curve of the isotherm of 0 °C.

4.9.3 Specimen for DMTA analysis

The DMTA technique is used to study underlayer (UL) samples, as their composition is strongly influenced by rubber, and therefore the above-mentioned theories concerning polymers are used. The molds for the underlayer samples are made in a HIT press (*hot isostatic press*); the press is used for prototypes, it is not a production press. A quantity of UL from a specific batch is taken, it is weighed and deposited in the mold of the press. The UL samples were molded on a circular 90 mm diameter disc, the thickness of UL depends on the initial weighing. There are several parameters of the press to mold the samples:

- Press pressure;
- Press temperature, the temperature is normally 150 °C, such as to have the peak of the phenolic resin crosslinking reaction (the reaction is exothermic therefore during molding the temperature increases). The temperature is set using electrical resistances;
- Cycle mode and duration of the molding, press and release phases are alternated to allow degassing, during crosslinking reaction the phenolic resin releases ammonia and water;

During the molding phase cracks can occur, i.e. the presence of gas bubbles that did not come out during the degassing phase (water and ammonia), this is a problem; mold parameters can be varied to optimize and minimize this phenomenon. ULs have this

Figure 4.15: On the left, there is a grinding pad to 3 mm from the metal back plate, the figure shows the underlayer distribution. On the right, the circular underlayer mold ($d = 90$ mm) and below this is the specimen for the analysis of DMTA.

problem because they contain a strong organic component. Molding parameters are an industrial secret.

The circular underlayer sample is milled and cutted for the DMTA test. The DMTA sample has the dimensions of 70x10x3 mm.

4.10 Frequency Response Function (FRF)

The FRF analysis aims to study the specific vibration frequencies of the pad and the damping. The vibrational modes of a body are determined by the intrinsic properties of the material (mass, geometry and composition). The system used consists of a micro-hammer with load cell, pad and accelerometer (see Fig.4.16).

The mechanical model can be simplified as excitation and response. The excitation is an impulse and the response is the frequency spectrum of the brake pad. Assuming that the system is linear and constant parameters [37], the relationship between input $f(t)$ and output $x(t)$ is:

$$x(t) = f(t) \otimes h(t) \tag{4.27}$$

$h(t)$ is the response function, in the frequency domain the convolution integral is reduced to the simple algebraic expression:

$$X(\omega) = F(\omega) \cdot H(\omega) \tag{4.28}$$

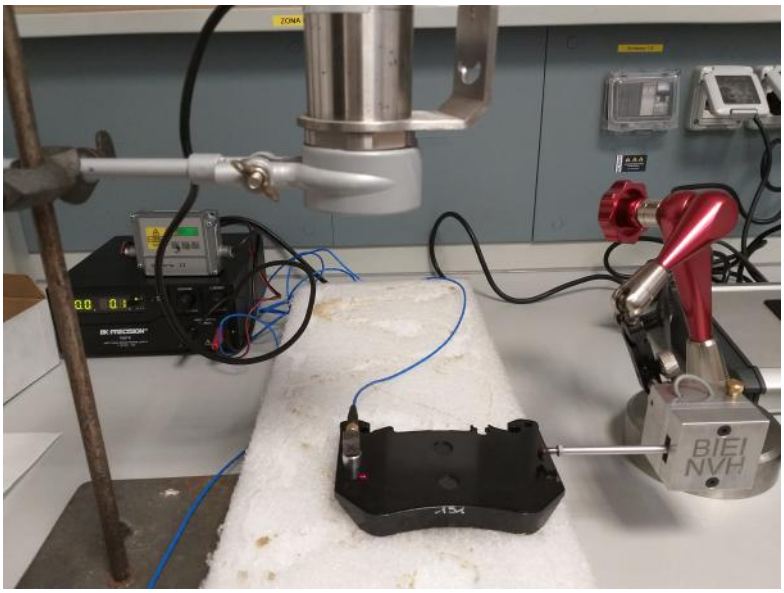

Figure 4.16: FRF setup, the sponge isolates the brake pad from external vibrations. The accelerometer is fixed by a screw on a magnetic base.

It is important to have a frequency content that covers the range of interest (up to 15 kHz), theoretically using an impulsive method the frequency information is complete:

$$F(\omega) = \int_{-\infty}^{+\infty} \delta(t) e^{-i\omega t} dt = 1 \tag{4.29}$$

FRF analysis is performed at temperatures of -30 °C, -25 °C, -20 °C, -15 °C, -10 °C, -5 °C, 0 °C and 25 °C, the brake pad is cooled in the freezer at -35 °C for more than 12 hours. The temperature is measured with an infrared thermometer on the metal back plate. At lower temperatures the modal frequencies of the pad are higher and have lower damping, this fact is due to the stiffening of the material. The Figure 4.17 shows the frequency responce function. Note for frequencies above 15 kHz there is noise not due to the material but to the non-impulse of the method, above this frequency there is no more information. The frequency spectrum is the average of five acquisitions, five hammer hits are performed with a two seconds pause. The height of the peak is valued as g/N, where g is the acceleration of the accelerometer and N is the force that gives the load cell to the micro-hammer. The natural frequency of vibration of the brake pad is valued at the local maximum of the FRF spectrum.

Damping (ξ) is defined by the single peaks with the **half-power band method** [37], the amplitude at -3 dB is:

$$\xi = \frac{\omega_2 - \omega_1}{\omega_0} \tag{4.30}$$

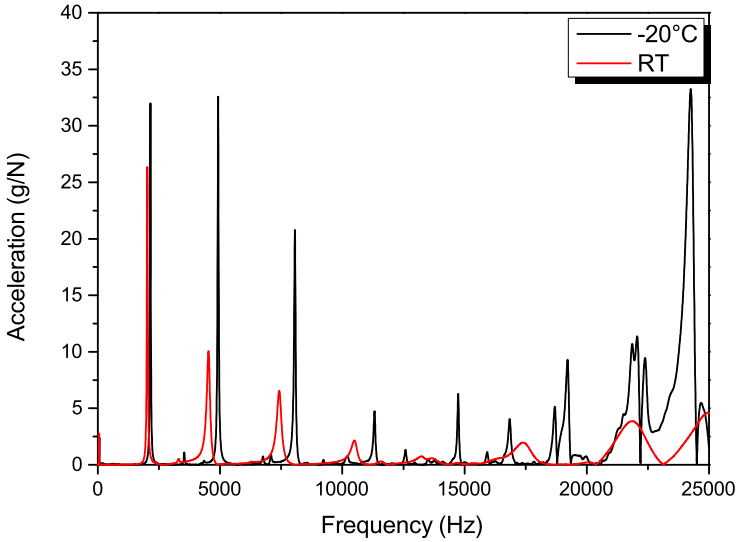

Figure 4.17: Example of FRF of a brake pad, FRF at -20 °C (black line) and FRF at 25 °C (red line).

The frequency range between ω_2 and ω_1 is called the **half-power band**, the average power dissipated by the effect of viscosity is approximately half of that dissipated in the phase resonance condition.

The measurements are done on a pad with the same geometry and friction material, the only difference is the underlayer.

4.11 Dyno test for Cold noise

Generally the dyno test allows all the information on the characteristics of a brake pad in the real application to be obtained. There are different types of tests, depending on the parameter that you want to evaluate; there are tests for wear, friction measurement, efficiency, particulate emission and acoustic measurements.
The test simulates the braking system of a motor vehicle, the system consists of a rotor, two brake pads (piston side and reaction side), caliper, pressure transmission circuit with oil and the *chassis*. Noise tests are performed inside an anechoic chamber, equipped with microphones and accelerometers for measuring mechanical vibration. Microphone acquisition is triggered with braking. Braking is defined as noisy if its amplitude exceeds 70 dB.

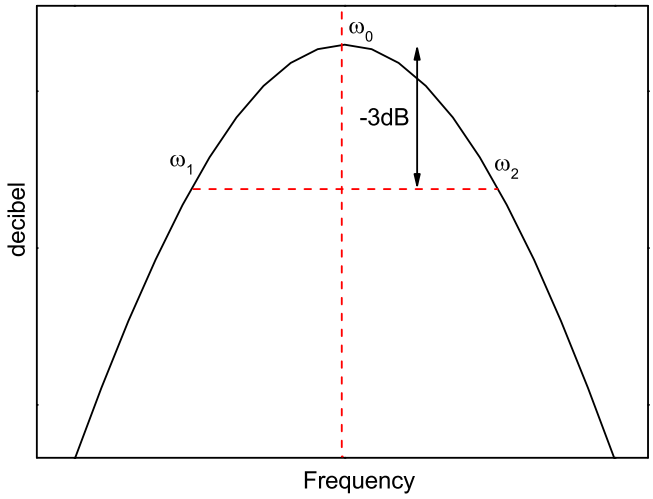

Figure 4.18: Damping calculation, the y axis is in decibel. ω_0 is the peak of the geometric resonance frequency.

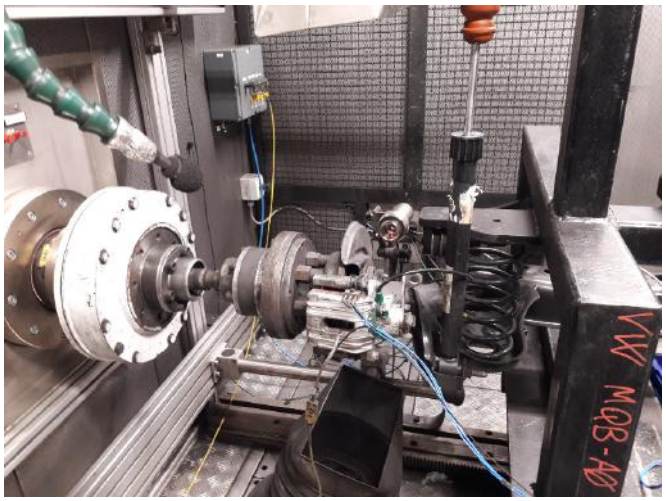

Figure 4.19: The figure shows a dyno test setup. There is a microphone for acquiring the acoustic signal, pyrometer for acquiring rotor temperature and the *chassis* (including shock absorber).

The dyno tests for the study of Cold Noise are of two types, the first procedure has an initial cooling of the chamber and a step increase in temperature and the second procedure has only the cold part.

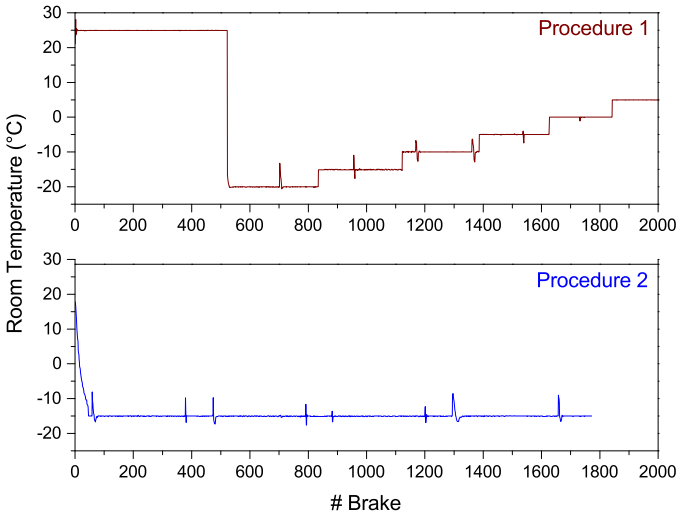

Figure 4.20: Thermal profile of the climatic chamber during the dyno test. In the first procedure 2034 braking are performed and in the second procedure 1772.

The temperatures of the rotor (infrared thermometer) and the pad (thermocouple 3 mm from the metal back plate) are measured. Procedure one maintains the temperature of the rotor at lower temperatures, performing low pressure brake, while the second procedure performs braking at higher pressures, which greatly heat the rotor and the brake pad, Fig. 4.21 shows the thermal profile of the rotors.

The result of the dyno noise test allows to obtain the characteristic acoustic frequencies of the brake pad according to all the physical parameters that influence the braking: pressure, rotor and pad temperature, relative humidity and speed.

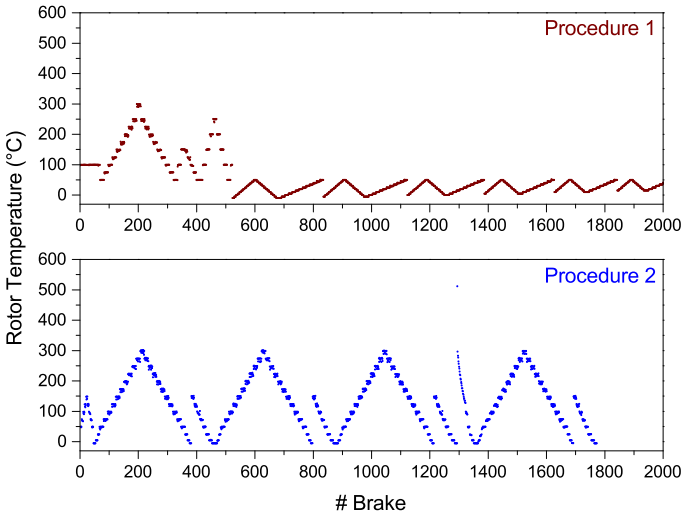

Figure 4.21: Thermal profile of the rotor during the dyno test. It is worth noticing that the rotors have different temperatures due to the braking pressures.

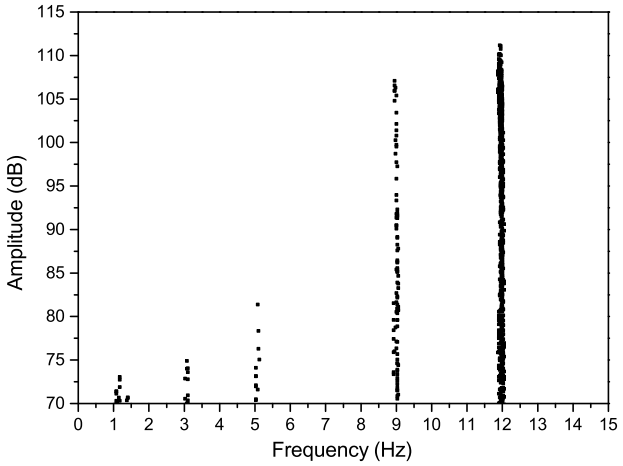

Figure 4.22: The figure shows an example of a dyno test result. The two critical frequencies for this project (different projects have different brake pad geometries) are 9 and 12 kHz. Any noisy braking (>70 dB) is a black dot in the graph.

The figure 4.22 shows the *Cold Noise* issue.

Figure 4.23: Thermocouple to measure the temperature of the underlayer. It is fixed at 3 mm above the metal back plate.

Chapter 5

Data acquisition and analysis

5.1 Tested materials: Noise generation

The first tested materials are all part of a project born in collaboration with *BMW*, with the purpose of looking for performing and comfortable materials. In particular this project aims to research a product with Low Steel materials performance but a low propensity to *Stick-Slip*, like the NAO materials. In order to do this a reference material is chosen as starting point. This material has good performances but it has an high propensity to *Stick-Slip* processes, and in particular to *Creep Groan* noise. The formulations of the other materials of the project start from the reference one, and change only some specific raw materials. In this way, it is possible to observe the effect of the single change. One NAO material was studied with these in order to see the differences between the two different families of material studied with this test. During this work these materials are studied on tribometer, on vehicle and on chassis dynamometer and the results are compared in the following chapter.

Friction material	Modification	Feature
Reference		
LS A	hydrophobicity pack	
LS B	inox steel fiber	
LS C	inorganic lamellar lubricant	particle size <100 μm
LS D	inorganic lamellar lubricant	particle size <100 μm
LS E	inorganic lamellar lubricant	particle size <50 μm
LS F	No inorganic lamellar lubricant	

Table 5.1: BMW tested materials. The main change from the reference has been indicated.

The studied materials are named with alphabetic letters (Table 5.1). The details of the formulas are industrial secrets, therefore it is not possible to give further details. The first two modifications are aimed at the effect of humidity, the latter focused on changing the distribution of the friction coefficient on the surface. LS C and D have the same type of modification, but the nature of the raw materials is different.
The second selection of materials tested are NAO and are tested on tribometer, with an opportune test. Seven materials have been tested, they are identified by alphabetic letters (from A to G). These materials were previously tested also on vehicle and on dyno. The dyno standard procedure was not able to distinguish the NAO materials and so the only way, before this study, was to directly study their performance on vehicle. From the vehicle test, *Stick-Slip* scores of the materials are delivered and so it was possible to compare the tribometer results with them. Whereas NAO materials have less propensity to *Stick-Slip*, therefore less time was spent on these materials. The mixes have not been optimized to understand the causes of the *Stick-Slip*, during the thesis only a measurement protocol was created.
The third selection is composed by samples of the same material but with different surface geometry. The samples are made of polyethylene and could be flat or patterned. These materials are part of a study, born as this work, by the collaboration of the University of Turin and ITT, that aims to correlate results of a *different shaped 3D objects friction model* and experimental results. This study is also important in order to evaluate the combined morphology and humidity effect on CoF without changing the chemical composition of the samples. In this thesis some preliminary results of this study are presented, in particular regarding the first experimental results that are carried out in the ITT laboratories.

5.2 Tribometer

Measurement method for the tribometer was entirely developed during this thesis work. Method development was driven by the tests done on chassis dynamometer, adapting their dimensions for the characterization by means of the tribometer. Changing the vehicle the brake pads and the brake system are different, hence, dynamometer tests are different for some input values, like for the brake pad and disc relative speed or pressure. These adaptations are required because of the variety of discs, wheels, inertia and brake pads dimensions used in different projects. One of the main advantage of the use of the tribometer is that these input values are systematically constant. This choice was done in order to study and to compare different friction materials, changing only them and not the whole system. During the tests, the tribometer saves as outputs CSV files that contain for each step measured the values of time, normal force, disc speed, humidity, torque and CoF. These files are analyzed with the software *Python*.

5.2.1 Bedding

After the first brakes, in which brake pads are *new*, they become *bedded*. This process, called *bedding*, happens due to the wear of the pads, the high pressure and the high temperature due to the high dissipation of energy by the friction force during the brake. This is the process that allows primary and secondary contacts plateau formation, described in the chapter 2. *Bedding process* will make CoF independent by the number of brakes. It is important to study the pads when *bedded* because in the normal applications on vehicle pads are *bedded*. In order to increase the repeatability of a particular test, a good practice is to make a *bedding process* before each test. In this way the brake pads surface is statistically the same for any test. The first step for testing materials on the tribometer is to find the right parameters to set it in order to obtain a *bedding process* suitable for it. As said in the section before, this is done adapting the chassis dynamometer *bedding process* to the tribometer dimensions. On chassis dynamometer there are a lot of different *bedding processes*, the one chosen could be resumed as follows:

- Dyno disc is accelerated until up to an equivalent vehicle velocity of 80 km/h.
- With a constant pressure of 30 bar in the pipe line of the brake system, the disc is decelerated until the equivalent on vehicle of 30 km/h. The brake duration depends on the inertia of the equivalent car and on the dynamic CoF of the brake pads, but lasts about for 4-5 seconds.
- After the brake, the system is cooled and then the brake is repeated for 80 times.

Since once *bedded* the material remains so, the aim of this adapting calculus is not to find exactly the same values scaled from the chassis dynamometer to the tribometer, but it is to find threshold values that allow to obtain the *bedding* of the tribometer samples. Once found the right parameters to set the tribometer it is possible to start measurements, with the bedding and then with other tests. A description of the calculation follows.
The most important thing is that the power dissipation surface density of the friction force of the dyno and the tribometer *bedding* are the same. It is defined as:

$$\xi = \frac{P_{ff}}{A} \tag{5.1}$$

where P_{ff} is the friction force power dissipation and A is the area of the brake pad. P_{ff} could be rewritten as:

$$P_{ff} = \frac{\int_{t_0}^{t_f} (F_f \cdot v_t(t)) \cdot dt}{T_b} \tag{5.2}$$

where F_f is the friction force of the pad on the disc, $v_t(t)$ is the relative tangential velocity between the disc and the brake pad and t_0, t_f and T_b are respectively the starting,

the final and the total time of the brake. From the equations 2.1, 5.1 and 5.2 it is possible to obtain:

$$\xi = \frac{\int_{t_0}^{t_f} (F_N \cdot CoF \cdot v_t(t)) \cdot dt}{A \cdot T_b} = \frac{p \cdot \int_{t_0}^{t_f} (CoF \cdot v_t(t)) \cdot dt}{T_b} \tag{5.3}$$

where F_N is the normal force of the pad on the disc and p is the pressure between the pad and the disc. As said before with this calculation it is necessary to find a threshold value of ξ required to have the bedding on the tribometer. So, calling ξ_d the power density of the dyno and ξ_t the one of the tribometer it is necessary that:

$$\xi_d < \xi_t \tag{5.4}$$

With geometrical calculation it is possible to find the value of normal force $F_{tribometer}$ to set on tribometer in order to have the same P of the dyno.

$$F_{tribometer} = \frac{A_{piston} 3 A_{sample}}{2 A_{brake\,pad}} P_{piston} \tag{5.5}$$

A_{piston} is the area of the piston of brake caliper, A_{sample} is the area of the sample of tribometer, the factor 3 because the test is done with 3 samples, $A_{brake\,pad}$ is the area of the brake pad (factor 2 because inside each brake caliper there are 2 brake pads) and P_{piston} is the pressure on the piston, which presses on the metal back plate of brake pad. Another important parameter is the sliding velocity, the conversion from dyno to tribometer $\omega_{tribometer}$ is done with the following formula:

$$\omega_{tribometer} = \frac{v_{wheel} R_{rotor}}{2\pi R_{wheel} R_{tribometer}} \tag{5.6}$$

v_{wheel} and R_{wheel} are respectively the speed and radius of wheel, R_{rotor} is the effective radius[1] of the brake disc and $R_{tribometer}$ is the effective radius of tribometer brake disc (see Figure 5.44).
Since the friction material and the disc on dynamometer and on tribometer are made of the same material, it is reasonable suppose that CoF is the same at the same number of brake, even if the tangential velocities are not a priori the same, for both. The duration of the brake is chosen to be the same on both the instruments. With these information and some calculations, the following relation is obtained:

$$\int_{t_0}^{t_f} v_{td}(t) \cdot dt < \int_{t_0}^{t_f} v_{tt}(t) \cdot dt \tag{5.7}$$

where $v_{td}(t)$ and $v_{tt}(t)$ are respectively the dyno and the tribometer tangential velocity. Since $v_{td}(t)$ follows a decreasing trend during the brake, if $v_{tt}(t)$ is chosen constant and

[1]The effective radius is the distance between the center of the brake disc and the center of the sample (or brake pad), friction is considered to be applied only in the central point. This is an approximation.

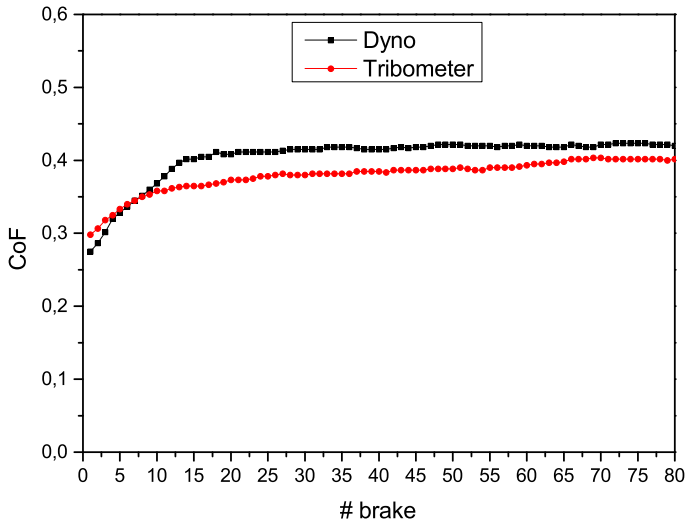

Figure 5.1: Comparison between bedding on tribometer and on dyno for the same friction material.

equal to the starting and maximum value of $v_{td}(t)$ the relation is satisfied. The geometric conversion factors are set on the tribometer, therefore the *bedding* test can start. The graph in figure 5.1 shows the result of the *bedding* on tribometer compared with the one on the dyno for the same friction material. It shows that the measurements done on tribometer give similar results, and that the calculation described before allows to pass from chassis dynamometer to tribometer. With the optical 3D profilometer it is possible to see the effect of the *bedding* on a pad (Fig. 5.2), that changes its height distribution and creates the plateaux of contact. The roughness of the randomly oriented raw materials of the new brake pad are smoothed by braking. Contact plateaux form on the brake pad and disc [59].

5.2.2 Stick-Slip: Low Steel test

The *Stick-Slip* test was again created starting from similar tests on chassis dynamometer. The tribometer test is not intended to copy the test on the dyno or vehicle but to study the phenomenon in a more accurate and repeatable way, because this should allow to understand better the *Stick-Slip* phenomenon. *Stick-Slip* phenomenon happens at low speed and it is linked to relative humidity. For these reason the measurements are done starting from a motionless situation, increasing slowly the speed, and repeating this measurements at different relative humidity values. The normal force instead is kept constant at one value for a brake and then changed at the following brake. The final

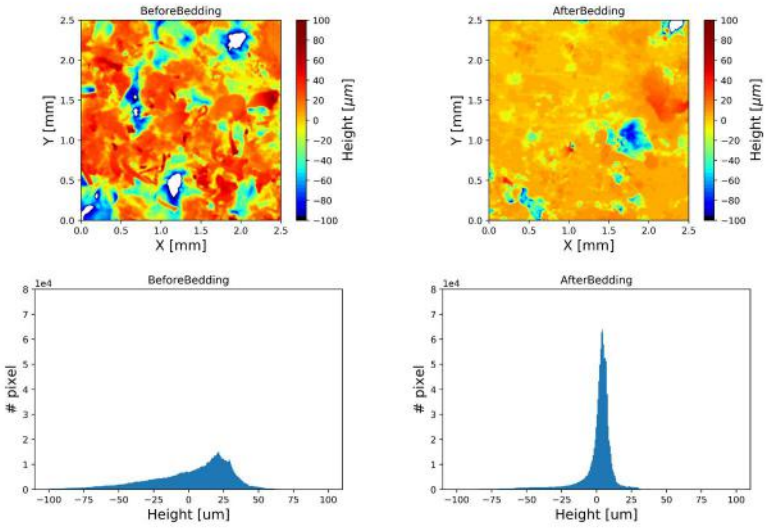

Figure 5.2: A new (left) and a bedded (right) sample. Morphological maps of the surfaces are shown on the top; on the bottom the height distributions. Range 2.5 x 2.5 mm, step 2.5 μm, total number of pixel = 10^6.

test, defined as the new protocol for the tribological characterization of the *Stick-Slip* phenomenon on Low Steel materials is the following:

- From a brake pad, considered representative of the whole batch, the samples are obtained as described in the paragraph 4.2.
- The samples are subjected to a *bedding phase*, in order to create a standard initial situation independent from the previous brakes.
- The real test starts by keeping the humidity at 20% of relative humidity for one hour, this is done again in order to create a standard initial situation.
- After that starts the real test. The humidity is kept at 20% and the normal force is set to 100 N. The disc starts from 0 RPM and it goes until 15 RPM (about 60 mm/s) in 20 s linearly increasing. The brake torque is measured only in this step, with a 2 kHz sampling frequency.
- The measure is repeated at 200 N always at 20% of relative humidity, waiting one minute between the brakes.
- The two brakes are repeated at the humidity of 40%, 60% and 80% of relative humidity. At each change of humidity value, the system is kept motionless for 10 minutes in order to condition the whole chamber and the material.

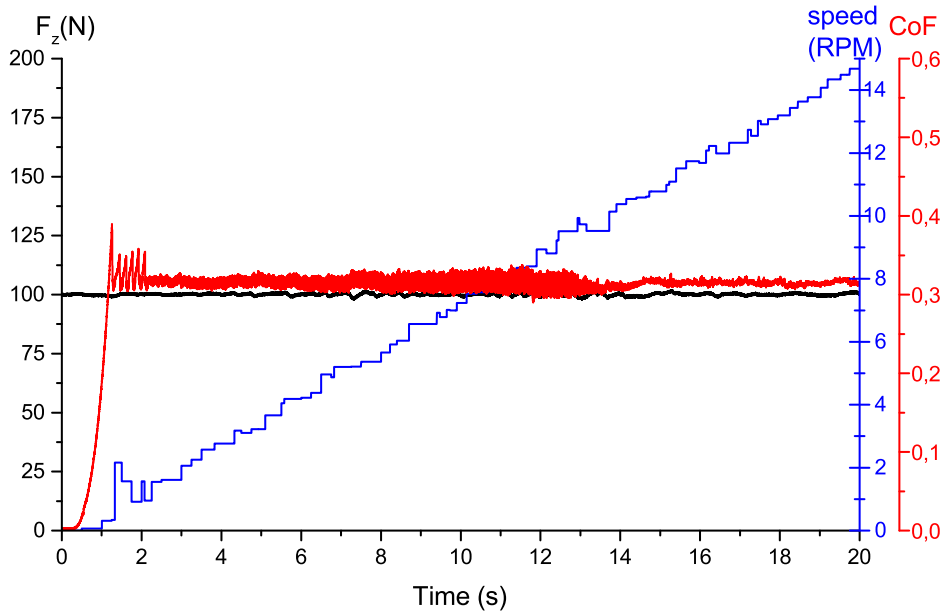

Figure 5.3: An example of one brake of the *Stick-Slip* test. The force (black) is kept constant, while the speed (blue) increases from 0 to 15 RPM. The resulting CoF is the red curve.

- All the test described, included the *bedding phase* are repeated 3 times on new samples.

The graph 5.3 shows one example of brake that composes the *Stick-Slip* Low Steel test. The graph 5.4 shows the different phases that characterize this kind of brake. Not all the phases are present in each brake, but their presence depends on humidity, on the formulation of friction material and on the normal force. In the static phase the disc is still motionless, the material stores elastic energy until the static friction force is reached. Then in the macroscopic *Stick-Slip* phase, the disc starts to move but it proceeds with jerky movements. This phase is noisy but it is not the one of interest in this test. This part will be studied in the *Stick-Slip* NAO test. The so-called *Creep Groan* phase is the interesting and most noisy part of the test. Actually the CoF vibrations of this phase are linked to a friction force instability that generates a mechanical vibration and then a mechanical noise. The frequency of this vibration is constant at 245 Hz, changing humidity, material and force, then it is reasonable to suppose that it is a resonance system frequency. The figure 5.5 shows a zoom of the macroscopic *Stick-Slip* and of the *Creep Groan* phase. In the macroscopic *Stick-Slip* the whole system changes it state from static to dynamic, instead in the *Creep Groan* phase is the single plateau that

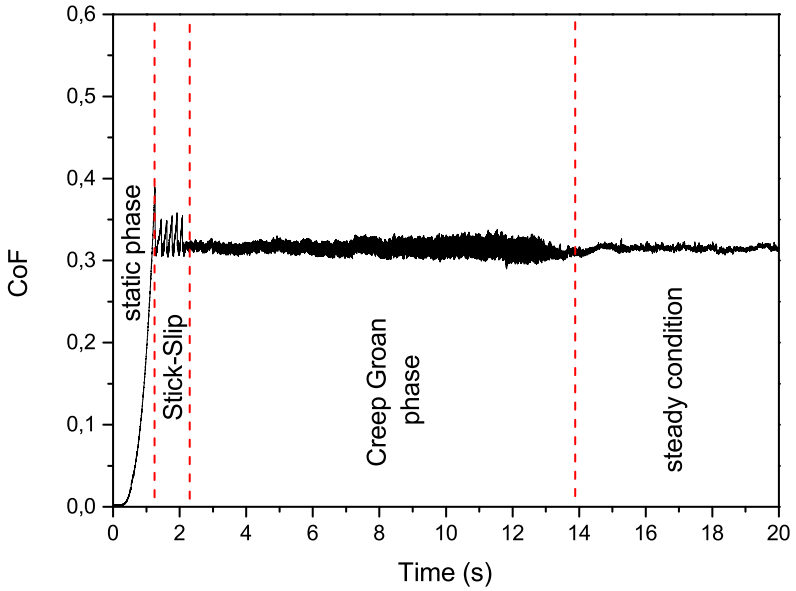

Figure 5.4: Example of CoF measured on one *Stick-Slip* brake, with the different phases.

change its state from static to dynamic generating vibrations. The curve shown in the figure 5.4 is described by the mechanical model presented in the paragraph 2.3.1. The *Stick-Slip* process is function of sliding speed; if the speed increases the duration of *Stick* phase decreases. This braking is done by accelerating, so the sliding velocity over time increases. If the friction changes as a function of speed a damping factor appears in the model solution so the amplitude of the vibration changes during the brake application. The amplitude of the vibration at low speed is high and the frequency is low (3-4 Hz), then in the second phase (creep groan) the amplitude of the vibration decrease and the frequency increase (about 245 Hz) and in the last phase a steady condition is archived due to the high sliding speed .

5.2.3 Stick-Slip: NAO test

The measurement method described in the previous section, is not able to characterize in a good manner NAO materials. This because they are more silent materials and it is very rare that they produce noise linked to the *Creep Groan* phase that, as explained in the following chapter, is the only phase analyzed with the *Stick-Slip* Low Steel test. For this reason, NAO materials show similar results for this test. However, NAO materials can produce macroscopic *Stick-Slip*. In order to emphasize this phenomenon, another test was created. The figure 5.3 shows that there are macroscopic *Stick-Slip* events at low

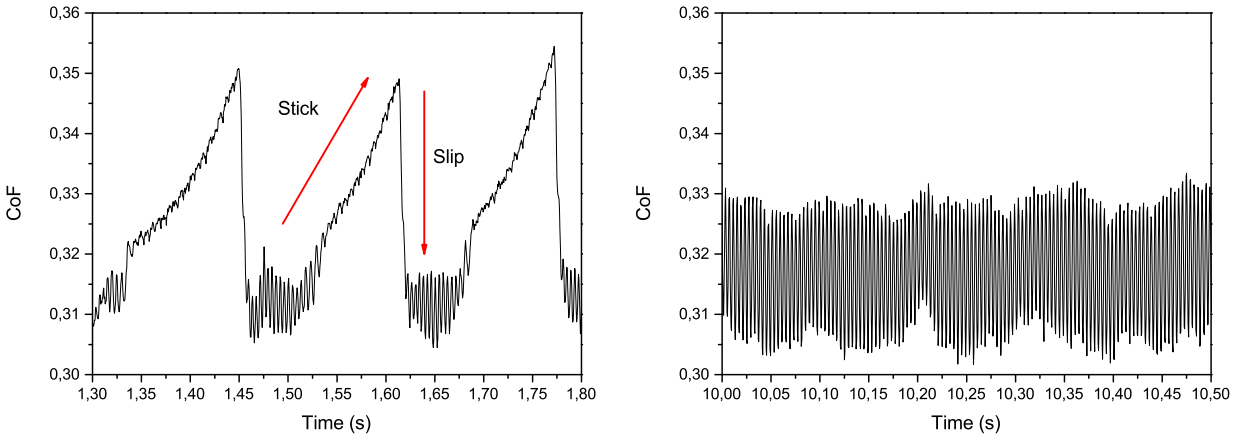

Figure 5.5: A zoom of the macroscopic *Stick-Slip* and *Creep Groan* phase.

velocities which disappear at higher velocities. So, a new test was developed, in which the velocity is fixed at 2 RPM (8 mm/s). In this way it was possible for critical NAO materials to have *Stick-Slip* events throughout the test (Fig. 5.6). In this case the brake is done either with a constant force of 200 N and changing humidity, as in the previous test (20, 40, 60 and 80% RH). The test is repeated 3 times for each material studied.

5.3 Chassis Dynamometer

A dyno procedure for the *Stick-Slip* noise study was created during the thesis. This procedure consists on various brakes at low speed and pressure at high relative humidity (60% and 90% of RH). CoF is measured with the equation 4.6, and in this case brakes are controlled under pressure, so the torque is measured. The mechanical vibrations are measured with a triaxial accelerometer (fixed by a screw Fig. 5.7) located on the caliper and the signal is analyzed, also in this case with the study of the FFT peaks. Screw fixing is the best from the mechanical point of view of the frequency response; glue, for example, changes its adhesion properties with temperature and humidity. The sampling frequency is 6 kHz.

Figure 5.8 shows an example of creep groan braking. These brakes simulate the vehicle start on a ramp (the slope is 12%) that is a critical situation for the *Stick-Slip* due to the slow speed, because the car is starting, and low pressure, because in order to start the brake is released slowly. Figure 5.9 shows a zoom on a single test brake. Looking at the CoF it is possible to see macroscopic *Stick-Slip* phenomenon before the disc start and that the CoF is not symmetric, indeed macroscopic *Stick-Slip* are present only at the disc start and not at the stop. The accelerometer signal shows when the disc starts

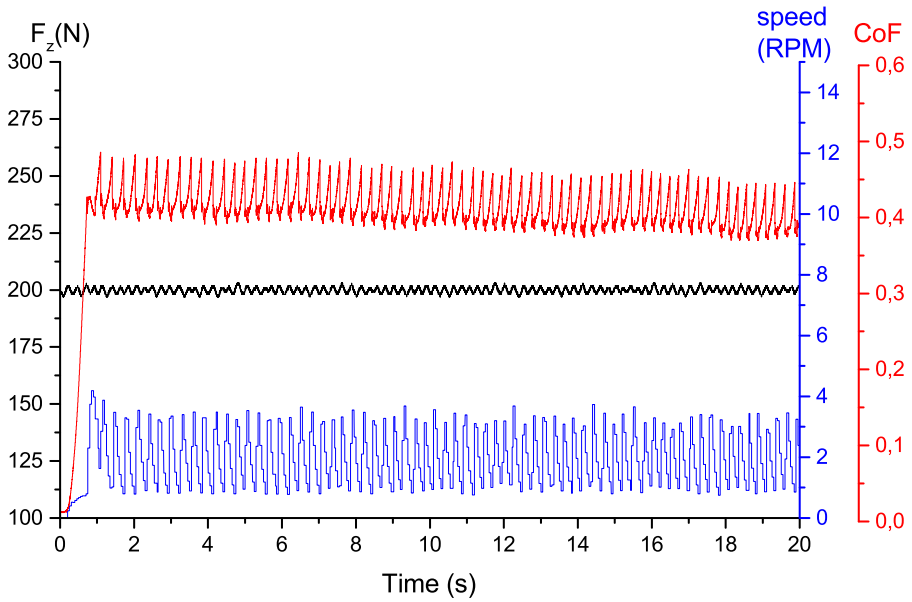

Figure 5.6: The test for NAO materials. The engine keeps the constant speed at 2 RPM.

Figure 5.7: Accelerometer is fixed by a screw on the caliper. The blue arrow indicates the position on the brake caliper.

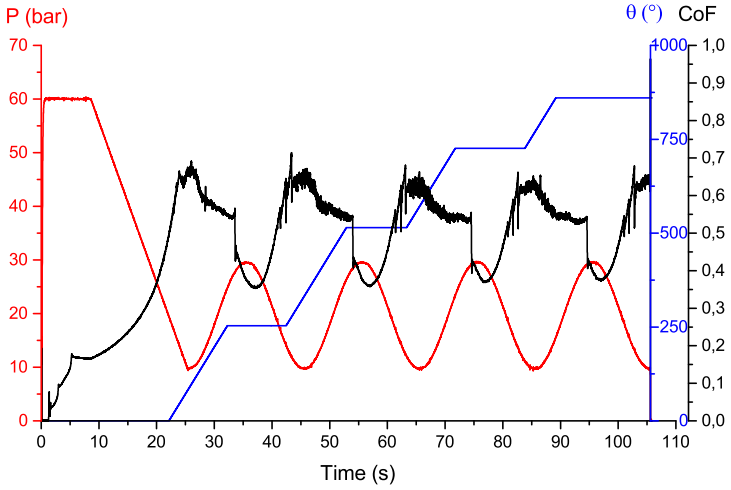

Figure 5.8: *Stick-Slip* test on chassis dynamometer. The motor delivers from the begin a torque. Initially the pressure in the brake line is high enough to keep the rotor motionless. Then the pressure, in red, decreases until the rotor starts, in blue, and after the pressure increases again to stop the rotor. The CoF value is graphed in black. The brake is repeated four times for about two minutes.

to rotate, the accelerometer mounted on the caliper starts to vibrate continuously. This is the mechanical vibration due to microscopic *Stick-Slip* phenomenon that generates the noise called *Creep Groan*. The vibration on the accelerometer is generated by a vibration of the friction force and so of the CoF.

Five brake applications are performed at 60% of RH and five applications at 90% of RH, the temperature of the chamber is keep at 10 °C. The amplitude of the pressure sinusoid is 10 bar, the pressure sinusoid frequency for the first three brake applications is 0.5 Hz, for the fourth application is 0.1 Hz and for the last one it is 0.01 Hz. The *Creep Groan* increases at a lower frequency; this procedure corresponds to a slower pedal release in the vehicle, therefore the system has more propensity to resonate. This procedure was used to compare tribometer results with dynamometer ones. The frequency response function of dyno is showed in figure 5.10, the principal frequency is 225 Hz and then there are three harmonics. The evaluation of each braking is given by the sum of the peaks of the geometric resonance frequencies. These frequencies depend on the geometry and stiffness of the dyno, the dyno system is more rigid than the vehicle. In the setup of dyno the chassis and shock absorbers were not used to emphasize the mechanical vibration.

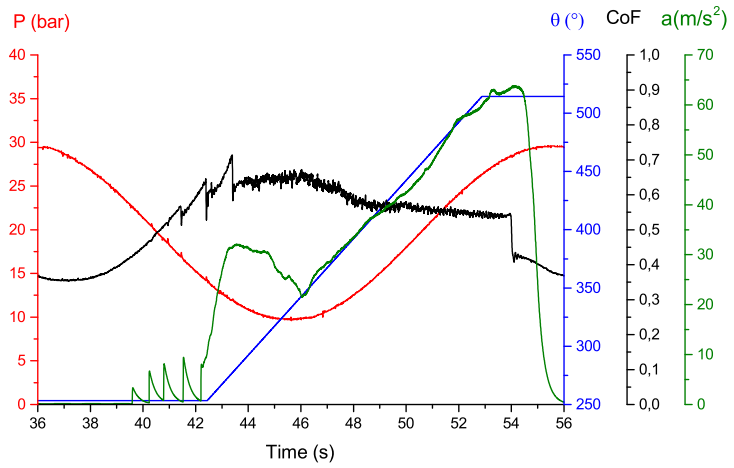

Figure 5.9: Single brake *Stick-Slip* test on chassis dynamometer. Pressure in red, disc rotation in blue, CoF value in black and the vibration acceleration in green.

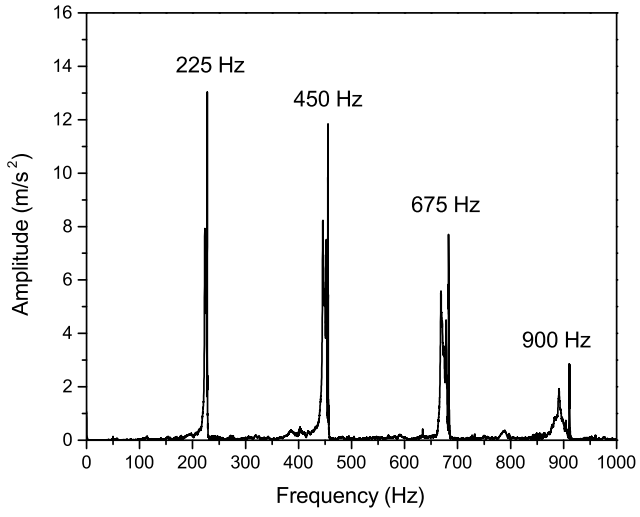

Figure 5.10: FFT on accelerometer of dyno test.

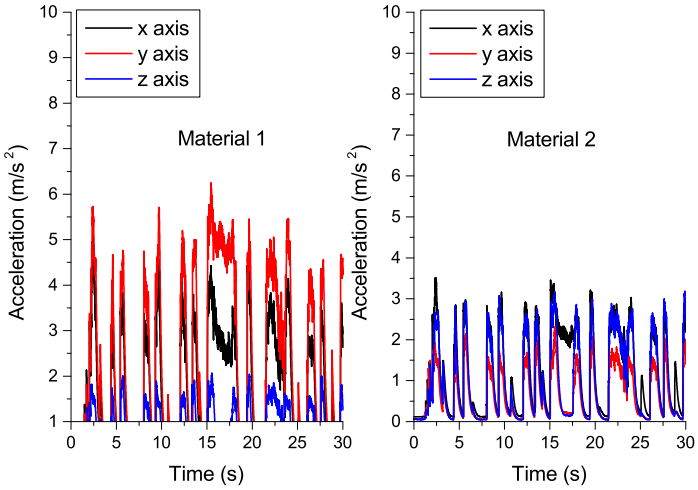

Figure 5.11: *Stick-Slip* test results on vehicle. On the left the acceleration as a function of time for material 1 (high *Stick-Slip* propensity), on the right the material 2 (low *Stick-Slip* propensity).

5.4 Vehicle

Also for the vehicle a special procedure for the *Stick-Slip* study was created. Two accelerometers are located on the car , one accelerometer is fixed on the right caliper and the other one on the left caliper, and they measure the brake vibrations with a 6 kHz sampling frequency. The output signals are analyzed with the same method used on the dyno. For each brake the driver assigns a score from 0 to 10 in order to evaluate the quality of the material. A material with 10 does not produce *Stick-Slip*. The brakes done are various and in different conditions, but all the brakes start from the stationary vehicle condition. Some examples are the starting on a ramp or different pads temperature or braking done in reverse gear. The car is located on a ramp and the driver release slowly the brake in order to start the car. This is a critical condition for the *Stick-Slip* phenomenon because vehicle speed and brake pressure are low. An example is shown in figure 5.11. The procedure for material evaluation lasts one week, more than 100 brakes are done to evaluate the material. Every day the same block of braking is repeated. For each brake application the FFT peak is calculated for left and right caliper, the average between left and right is calculated and then, the score of the day is the sum of the average values (left and right) of the FFT peaks. The final score is the average of the five days of test, the error is the standard deviation. The frequency response function of vehicle is showed in figure 5.12, the main frequency is about 80 Hz.

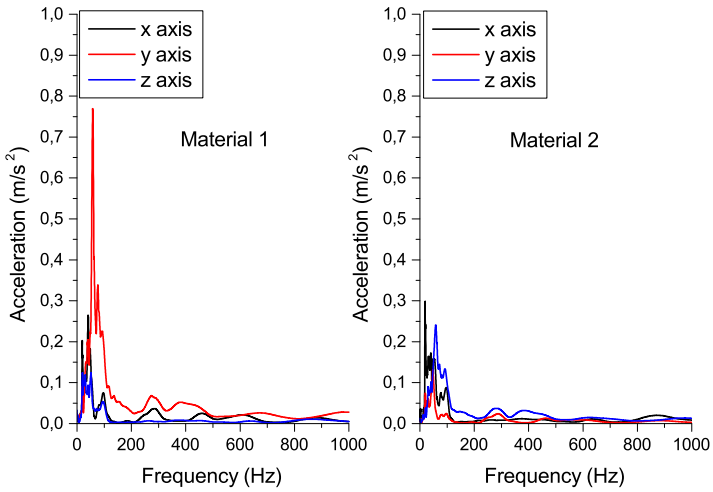

Figure 5.12: *Stick-Slip* test results on vehicle. On the left the acceleration as a function of frequency for material 1 (high *Stick-Slip* propensity), on the right the material 2 (low *Stick-Slip* propensity).

5.5 Surface measurements

In order to find a correlation between topography and *Stick-Slip*, pads surfaces are studied. First of all the pad is photographed with the optical microscope (Fig. 5.13 and Fig. 5.14). Then it is studied with the profilometer. This in order to obtain surface parameters as roughness, Kurtosis and Skewness, the altimetric map (Fig. 5.15) and the distribution of the height (Fig. 5.16) (definition of surface parameters are in appendix A). The correlation matrix (appendix C) is then performed with the *Stick-Slip* results and the surface parameters in order to understand which are the parameters that influence more the *Stick-Slip* phenomenon. The profilometer was set to scan an area of 5 x $5mm$ with a step of 5 μm. A threshold of ± 20 μm from the mean value is used to cut the data before the calculus. In this way the big holes that are not involved during the brake, are neither involved in the calculation. Then the pad is studied with the SEM. It allows to study the topography at very high resolution, to see the contact plateau (Fig. 5.17) and to study the surface chemical composition (Fig. 5.18). Finally the pad can be analyzed using the FIB.

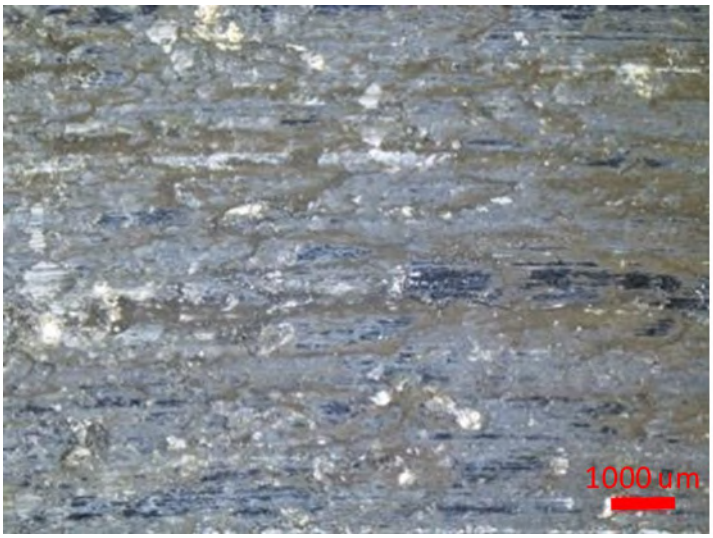

Figure 5.13: Optical image of the reference Low Steel material obtained with optical microscope. Incident light, zoom 10X.

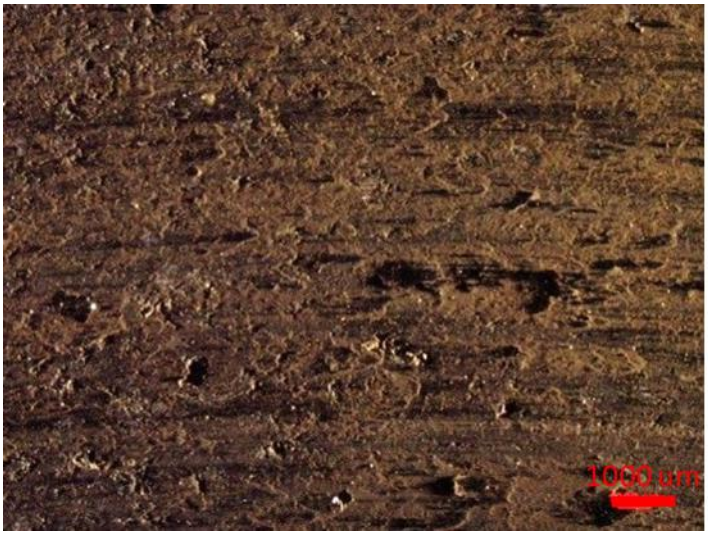

Figure 5.14: Optical image of the reference Low Steel material obtained with optical microscope. Lateral light, zoom 10X.

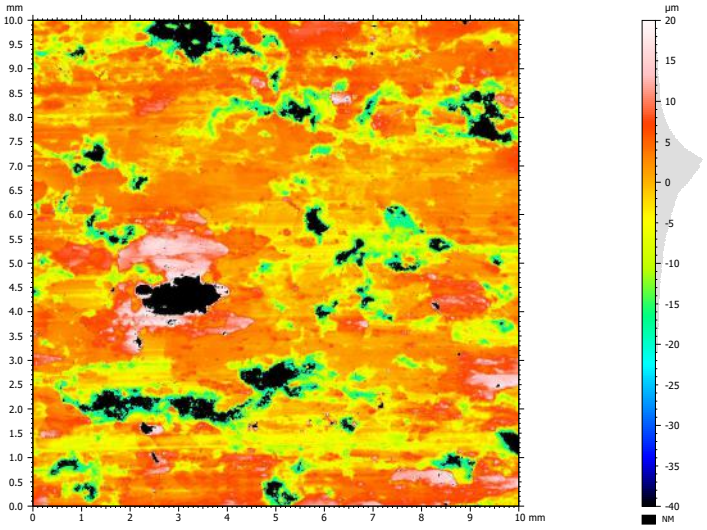

Figure 5.15: Altimetric map of the reference Low Steel material obtained with 3D optical profilometer. Scan step = 5 μm, range = $5x5$ mm. In black the points out of the threshold. To the left of the color scale is the histogram of the height distribution.

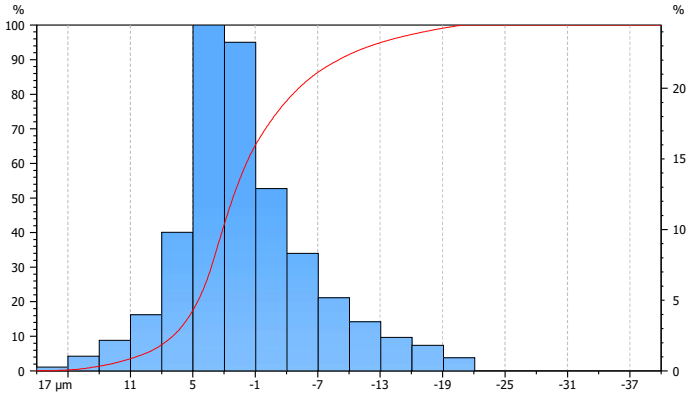

Figure 5.16: Histogram of the height of reference Low Steel material obtained with 3D optical profilometer in blue. In red the cumulative distribution of the height.

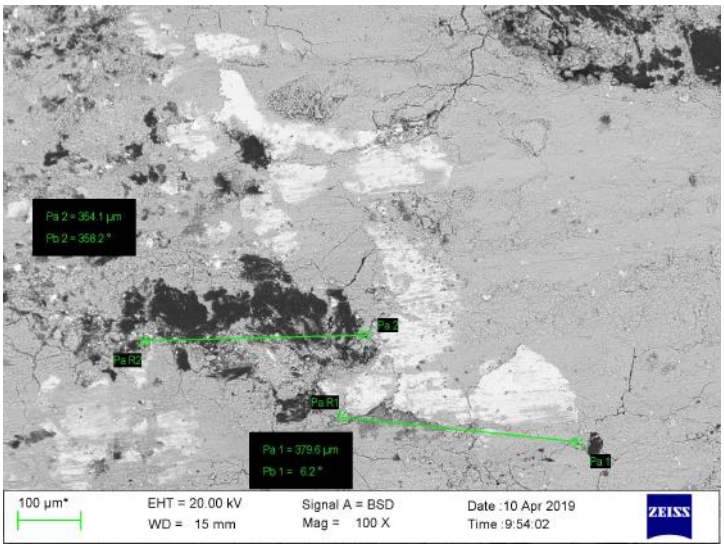

Figure 5.17: SEM image of reference Low Steel material, with graphite (black) and iron (white) outlined and measured.

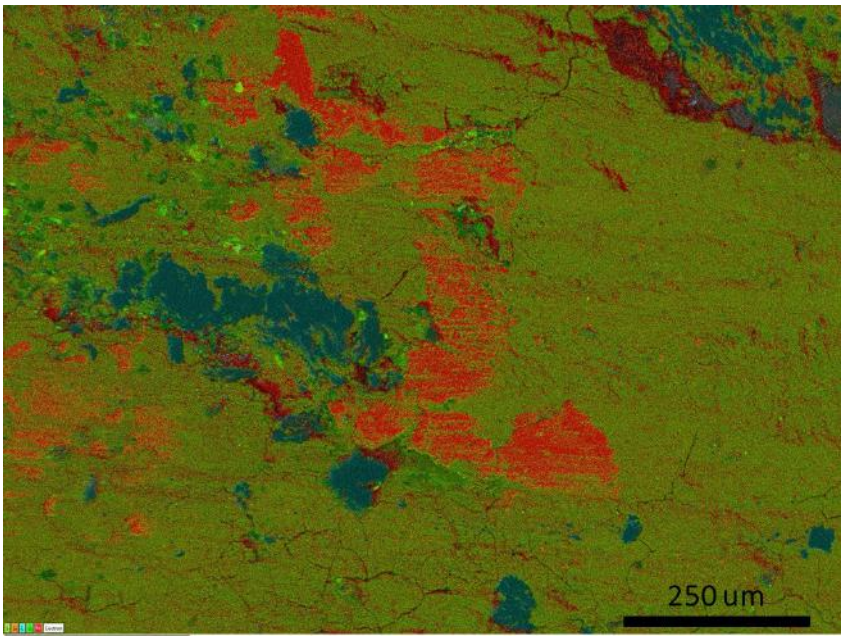

Figure 5.18: SEM mapping of reference material (fig. 5.17). In red iron, in blue carbon and in green oxygen. Magnification 100x.

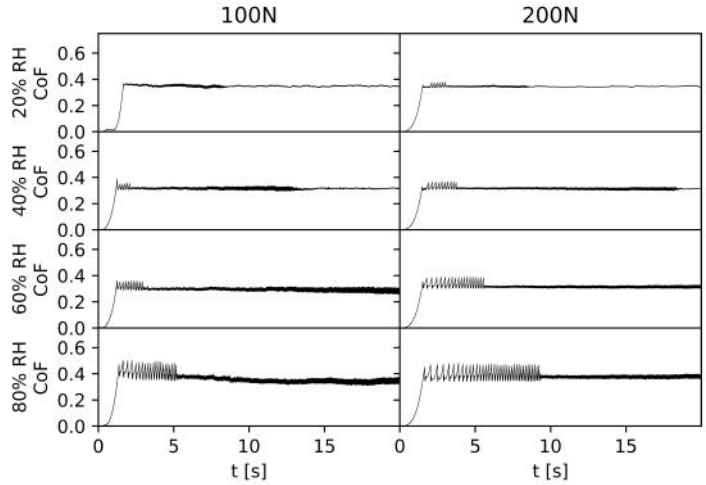

Figure 5.19: Reference Low Steel material. Ensemble of the eight brakes that compose the *Stick-Slip* test. From left to right force increase, from top to bottom the humidity increase. Every brake is done at constant normal force, with the velocity that increase from 0 to 15 RPM in 20 s.

5.6 Test on BMW materials

5.6.1 CoF vs Time

Since BMW materials are prevalent Low Steel materials, the *Stick-Slip* Low Steel test is performed on these. From the eight brakes coming from each test a graph of the CoF versus time is done. Figure 5.19 shows the graphs relative to the reference material. Moving form the left to the right on the graphs the force increase, so the number of macroscopic *Stick-Slip* events increases. Their amplitude does not increases and is almost constant. From top to bottom relative humidity increases (from 20 to 80% of RH). In this case either intensity and duration of both macroscopic *Stick-Slip* and Creep Groan phase increase. The amplitude increase of the macroscopic *Stick-Slip* means an increase of the difference between the static and the dynamic CoF. The graphs in figure 5.20 shows the result of the *Stick-Slip* test on a NAO material. The Creep Groan phase is not present for this material, and on the NAO materials in general, and for this reason a particular test was studied for this kind of material.

5.6.2 Analysis

The analysis for each material is done in the following way. First of all the Fast Fourier transform (FFT) of the whole CoF signal of each brake is performed. Then the FFT is smoothed with a Savitzky-Golay filter. It is a 51 points window filter and fit the signal

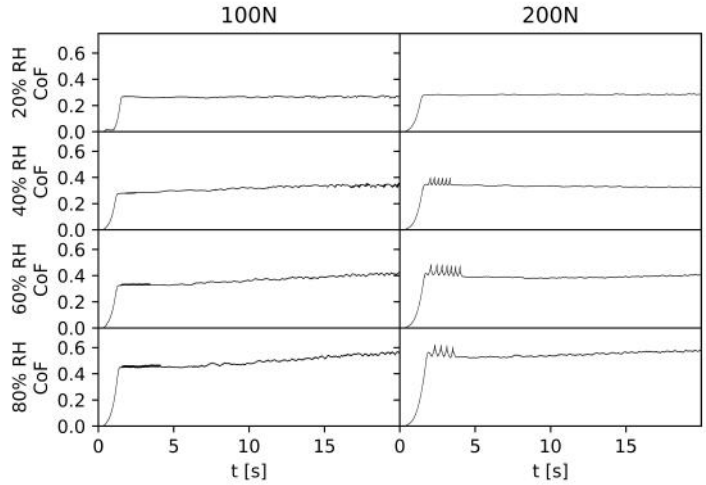

Figure 5.20: NAO material. Ensemble of the eight brakes that compose the *Stick-Slip* test. From left to right force increase, from top to bottom the humidity increase. Every brake is done at constant normal force, with the velocity that increase from 0 to 15 RPM in 20 s.

with a fifth order polynomial. Figure 5.21 shows the *FFT*, with the smoothing, of a particular brake. The peak at 245 Hz is due to the vibration linked to the Creep Groan phase and it is the only relevant in the study. The macroscopic *Stick-Slip* phase does not generate a peak in the *FFT* because its frequencies are low and not constant (the frequencies of it depends on the disc velocity that increase during the test, see paragraph 2.3.1). For this reason the NAO materials, that have a *FFT* without peaks, need another test and analysis. The height of the *FFT* peak for Low Steel materials is proportional to the Creep Groan phase vibration amplitude and duration. If the brake does not produce Creep Groan noise, the *FFT* is flat with negligible peaks. For this reason each brake is evaluated by the height of its *FFT* maximum peak. The final value used for the characterization is the mean of the eight *FFT* maximum peaks, one for each brake. The results of the different brake pads studied are resumed in the graph in figure 5.22. The best materials are the ones that have a minor amplitude that are *LS F* and *LS D*.

5.6.3 Spectrogram

The brakes are also analyzed qualitatively through the CoF spectrogram. A spectrogram is the *FFT* on time of the signal. This is done dividing the whole signal in segments and then making the *FFT* of each of them. On the x-axis there is the time, and on the y-axis there is the frequencies. The amplitudes of every *FFT* are plotted in vertical at the relative time position, with the amplitude described by the color scale. The spectrogram,

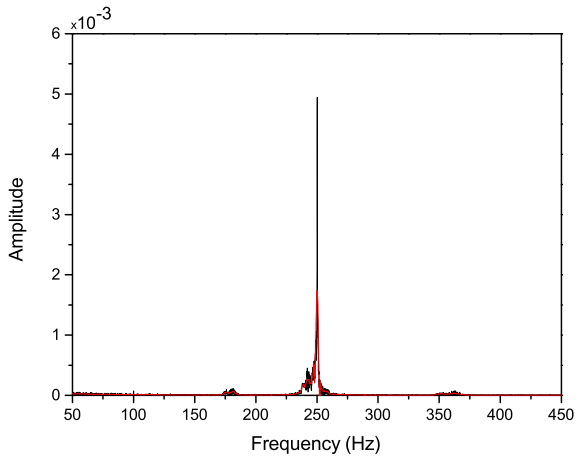

Figure 5.21: In black the *FFT* of the CoF signal of one brake and in red the *FFT* smoothed. Savitzky-Golay filter parameters: window length 51, fifth order polynomial.

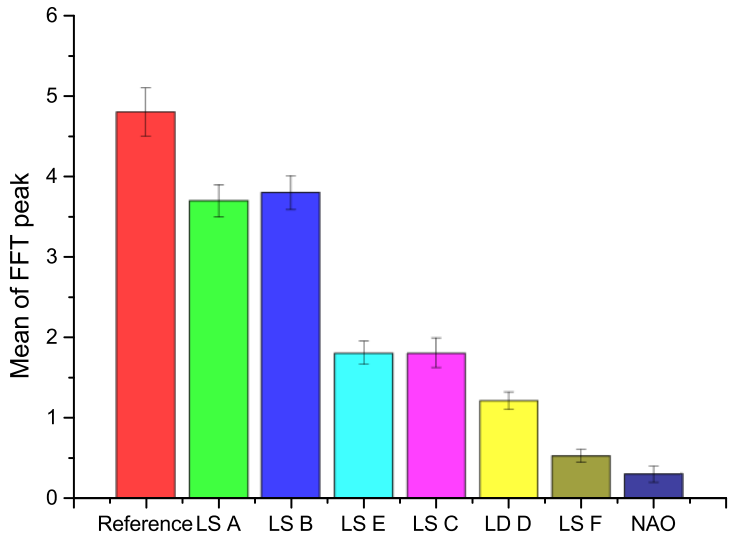

Figure 5.22: Results of the *Stick-Slip* test for Low Steel materials. Amplitude is the mean of the *FFT* maximum. For the errors standard deviations was used.

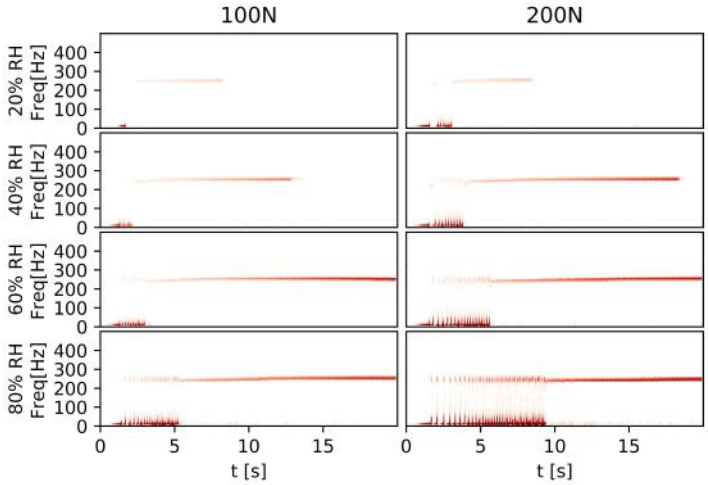

Figure 5.23: Spectrogram for the reference material. Segment time 0.128 s, overlap 0.64 s. The amplitude of the FFT is given by the intensity of the red color.

in this way, shows the evolution of the frequencies, with their amplitude, in the time domain. The spectrogram of the *Stick-Slip* test done for the reference material is in figure 5.23. In the spectrogram it is possible to see the evolution of the CoF vibration intensity and frequency. In the first part of each spectrogram there is the part linked to the macroscopic *Stick-Slip*. This part results in diverse frequencies excited because of the discontinuity between the *Stick* and the *Slip* phase. The spectrogram of the Creep Groan phase instead shows as it vibrates always at the same frequency, and that the other frequencies are not excited. Figure 5.24 shows the spectrogram done for the NAO material. As expected there are no frequencies excited.

5.6.4 Surface results

With the profilometer it was possible to calculate the roughness, the Skewness and the Kurtosis of the friction materials. The results are resumed in the table 5.2. From the correlation matrix done with the surface parameters and the results of the *Stick-Slip* test, it was possible to see the different correlations between the *Stick-Slip* amplitude and the different surface parameters. In the correlation matrix the NAO material was excluded because it has a very different chemical composition that influence more the *Stick-Slip* than the surface parameters. The correlation matrix is in table 5.3. The first matrix correlation row shows that the parameters that influence more the *Stick-Slip* amplitude are the Ssk and the Sku. The Ssk has a indirect correlation of -0.76, while Sku has a direct correlation of 0.67. For values close to 3 of Kurtosis the meniscus force increase if the Swewness decreases, as demonstrated by Bhushan [13]. Both the parameters have a

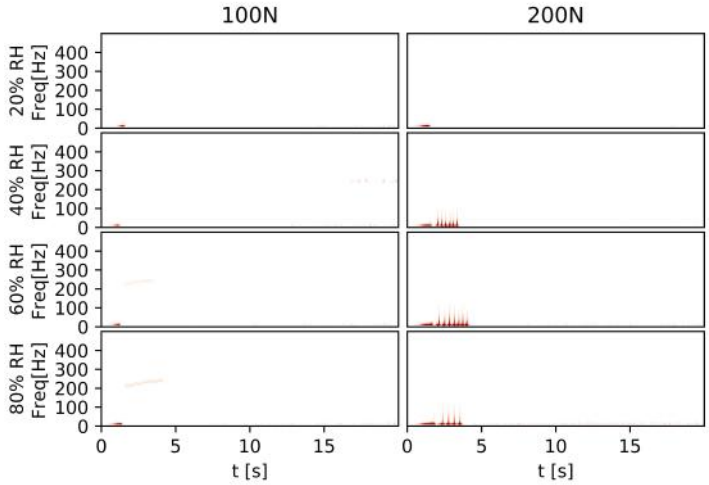

Figure 5.24: NAO material spectrogram. Segment time 0.128 s, overlap 0.64 s. The amplitude of the FFT is given by the intensity of the red color.

moderate correlation, and this means that the surface distribution parameters have an influence on the *Stick-Slip* but as expected there are also other parameters involved in this phenomenon. In order to understand better the influence of the surface, we performed a new study on polyethilene patterned surface, as reported in section 5.8.
All the BMW material are also analyzed with the SEM and the EDS in order to compare the surface and in particular the difference between the contact plateau (Fig.5.25). Excepting for the NAO material that has a very different composition, it is possible to see some differences between the three materials that produce more *Stick-Slip* (reference material, the Low Steel A and the Low Steel B) and the two that produce less *Stick-Slip* (Low Steel C and Low Steel B). The former have the graphite (in black) of the same dimension of the iron fibers (in white). The graphite is a lubricant and the iron is an abrasive, and the presence of both, of the same dimension, generate a not uniform CoF value on the surface. This could be an explanation for the friction instability that generates *Stick-Slip* phenomenon. The latter instead have small pieces of graphite and the iron fibers have debris on the surface. This makes the CoF value more uniform on the surface and it could be the explanation of the minor generation of *Stick-Slip* phenomenon. The chemical characterization of the surface was done with the EDS (Fig. 5.26). Friction materials with particle size of graphite less than 100 μm or without graphite have a low propensity to *Stick-Slip*.

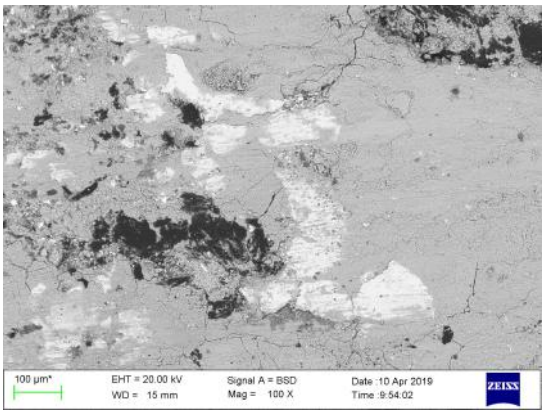

(a) Reference material

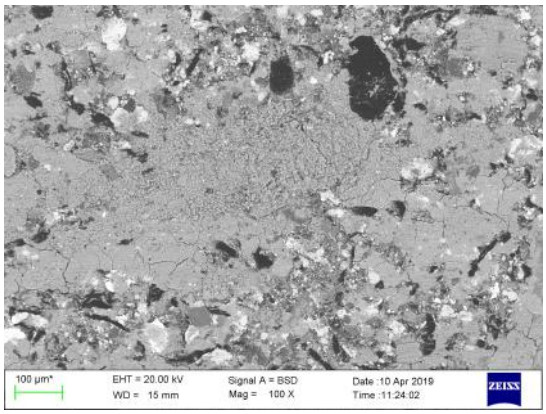

(b) NAO

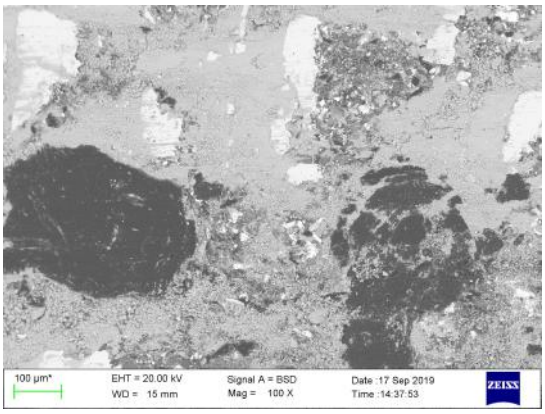

(c) LowSteel A

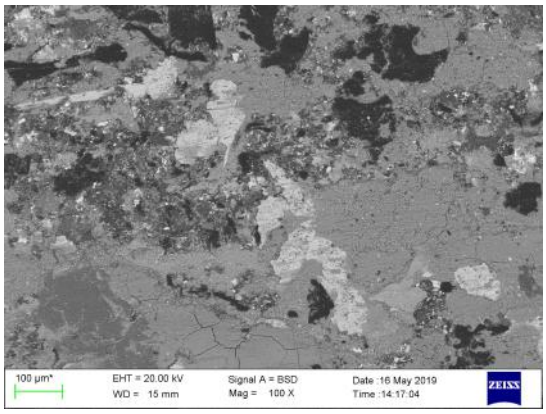

(d) LowSteel B

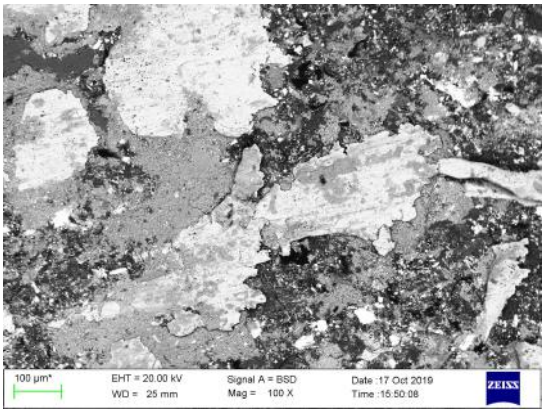

(e) LowSteel C

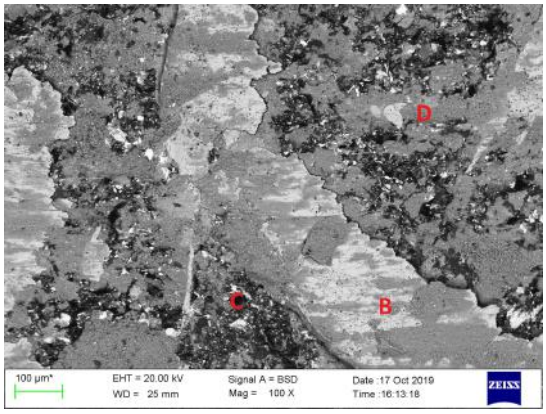

(f) LowSteel D

Figure 5.25: SEM results - 100X

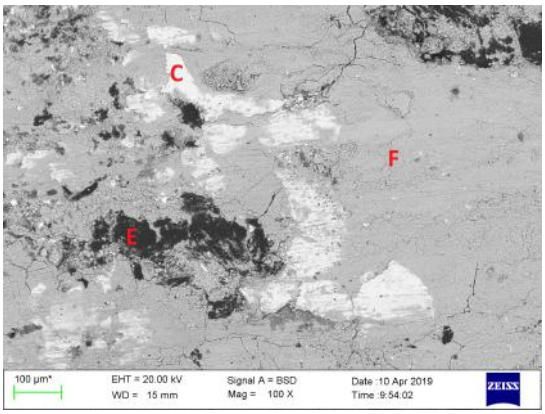

(a) EDS points.

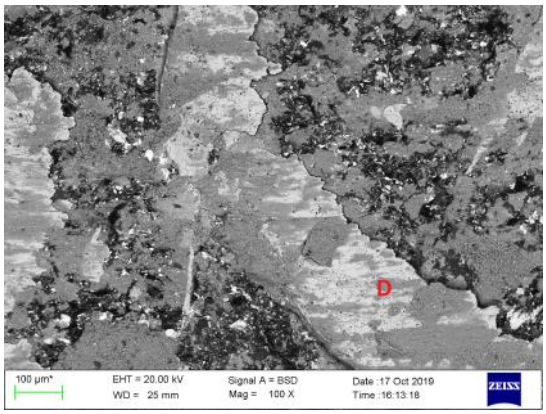

(b) EDS points.

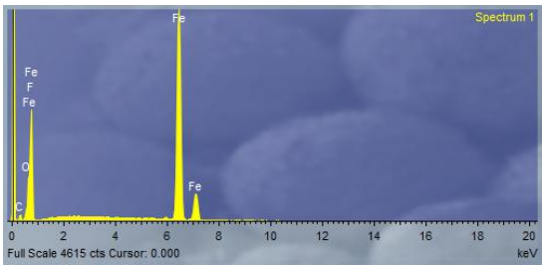

(c) EDS of fiber.

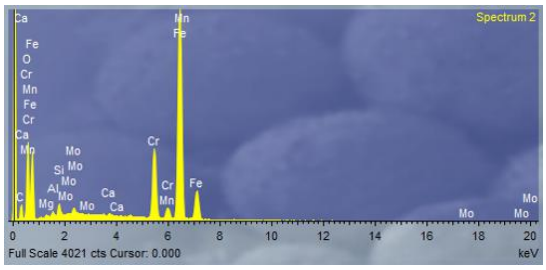

(d) EDS of fiber with debris on surface.

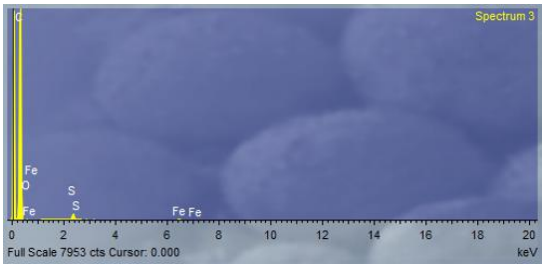

(e) EDS of lubricant.

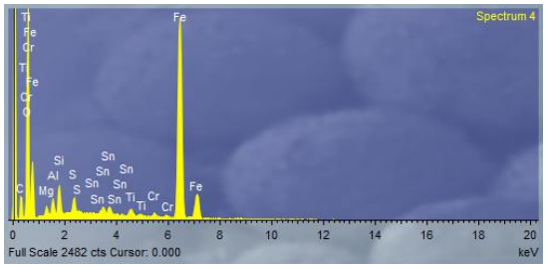

(f) EDS of debris.

Figure 5.26: Example of EDS results.

Table 5.2: Surface parameters

Material	Sq [μm]	Ssk	Sku
Reference	6.3 ± 0.3	-0.9 ± 0.2	4.2 ± 0.4
NAO	5.2 ± 0.6	-1.29 ± 0.12	5.2 ± 0.2
LS A	5.9 ± 0.8	-0.6 ± 0.5	4.6 ± 2.0
LS B	5.7 ± 1.8	-0.4 ± 0.3	4.3 ± 1.1
LS C	7.3 ± 1.1	-0.35 ± 0.07	3.2 ± 0.5
LS D	6.4 ± 0.6	-0.50 ± 0.04	3.9 ± 0.2
LS E	6.3 ± 0.8	-0.41 ± 0.04	3.7 ± 0.5
LS F	6.0 ± 0.4	-0.34 ± 0.04	3.8 ± 0.8

Table 5.3: Correlation matrix

	Amplitude	Sq	Ssk	Sku
Amplitude	1	-0.27	-0.76	0.67
Sq		1	0.13	-0.82
Ssk			1	-0.53
Sku				1

5.6.5 FIB results

Before the bedding phase, the brake pad is new, so the raw materials have random orientation, after the bedding phase the raw materials, due to the effect of pressure and temperature, have a direction given by the direction of braking. During bedding phase the third body layer grows. Figure 5.27 shows the brake pad surface after bedding process, the white areas are the primary plateau (made by iron), light gray areas are the secondary plateau (compacted debris, its chemical composition is variable), black areas are the graphite (used in the brake pad as lubricant) and finally there are the debris area, which have marginal effect on friction generation.

The primary plateaux of Low Steel material are composed by steel fiber (iron), the harder raw materials form the primary plateau, the softer materials wear more easily, therefore the different areas of the brake pad have different heights. The primary plateaux act as a point of accumulation of debris, thanks to pressure and temperature, the debris is melted and the secondary plateaus grow (Figure 5.28). Debris are the deepest points and so only at high pressures do they affect friction (the *Stick-Slip* process occurs at low pressure regime). In the debris area there are debris coming from the primary and secondary plateaux formation and fragments of raw materials.

Some FIB excavation are done on primary and secondary plateau, debris and graphite. The FIB excavation (using Ga ion) is done with the following procedure:

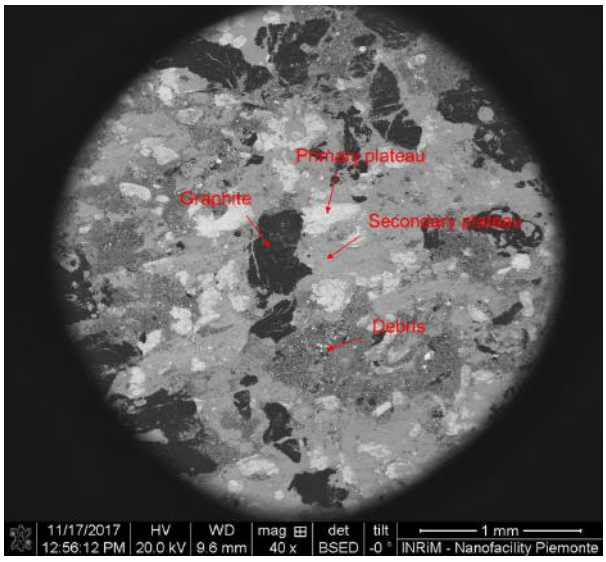

Figure 5.27: Image of brake pad surface (BSD detector).

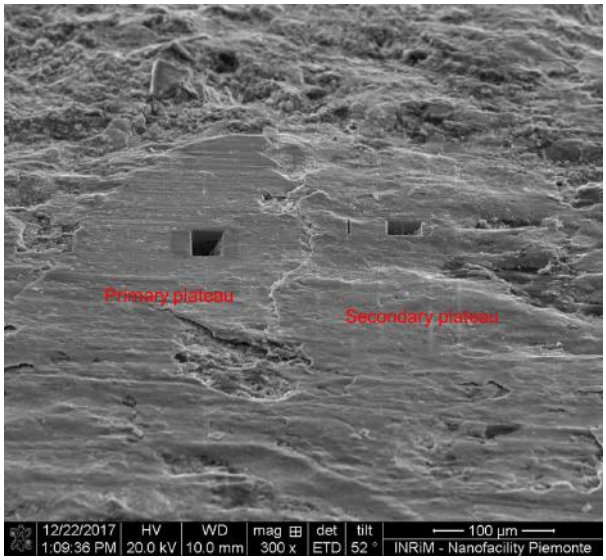

Figure 5.28: Primary and secondary plateau grow. On the left side there is the primary plateau, the secondary plateau grows during the brake process.

- step one, the emission current is 7 nA, shape of excavation: regular cross section, duration: 30-40 minutes, target: coarse excavation;
- step two, the emission current is 1 nA, shape of excavation: rectangular cross section, duration: 10-15 minutes, target: coarse cleaning of the surface of interest;
- step three, the emission current is 100 pA, shape of excavation: rectangular cross section, duration: 20-30 minutes, target: cleaning of the surface of interest;
- step four, the emission current is 30 pA, shape of excavation: rectangular cross section, duration: 20-30 minutes, target: accurate cleaning of the surface of interest;

The duration of each step depends on the type of material on the surface of the brake pad. The excavations are complex because the brake pad has a lot of raw materials with different nature and so the milling rate[2] is complex. The coefficient of friction and its stability are affected by the third body layer distribution, for instance as figure 5.17 shown, the presence of large areas of iron and graphite nearby can accentuate the *Stick-Slip*. The friction coefficient on the graphite area is very different from that in the iron area, this can cause a local friction instability. Figure 5.29 shows the FIB excavation on steel fiber, the thickness of third body layer is about 5 um, the steel fiber is stressed in the direction of braking; under the steel fiber there are the raw materials of brake pad as new. The primary plateau is compact and in the low pressure regime is the most import part of the brake pad surface.

Figure 5.30 shows the FIB excavation on secondary plateau, it is less compact than the steel fiber. The raw materials form a homogenized material, the secondary plateau composition depends by the raw materials inside the mix.

Finally, the debris area is like the new brake pad, Figure 5.31 shows the FIB excavation on debris, here the effect of pressure and temperature is negligible.

NAO doesn't have steel fiber in the mix formulation, so, the composition of primary plateau different from Low Steel. The composition of NAO primary plateau is similar to secondary plateau, the growth of this layer is important for the friction stability. If the primary plateau is compacted and the chemical composition is homogeneous the coefficient of friction is stable on it. Figure 5.32 shows a compact and homogeneous third body layer, this material has low *Stick-Slip* propensity.

The thickness of third body layer is between 4 and 10 um.

5.6.6 Humidity effect

In order to evaluate the effect of the humidity on the *Stick-Slip* process, and in particular on the Creep Groan noise, the graph in figure 5.34 was done. The graph shows the

[2]The milling rate is defined as the ratio of the volume of the milled material to the product of the beam current and irradiation time.

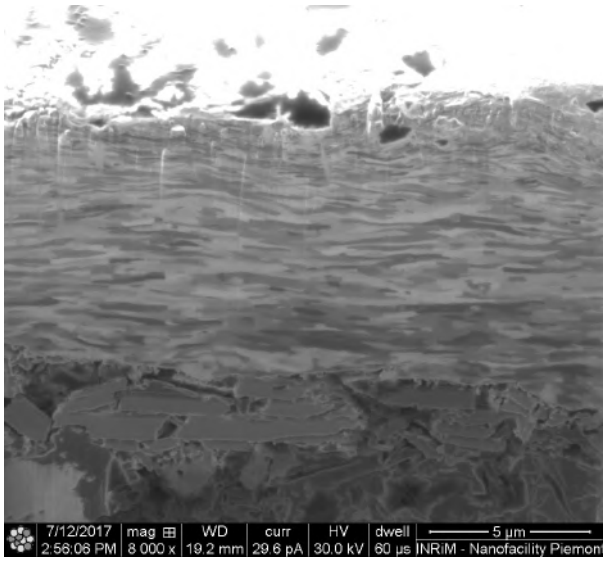

Figure 5.29: FIB section of primary plateau.

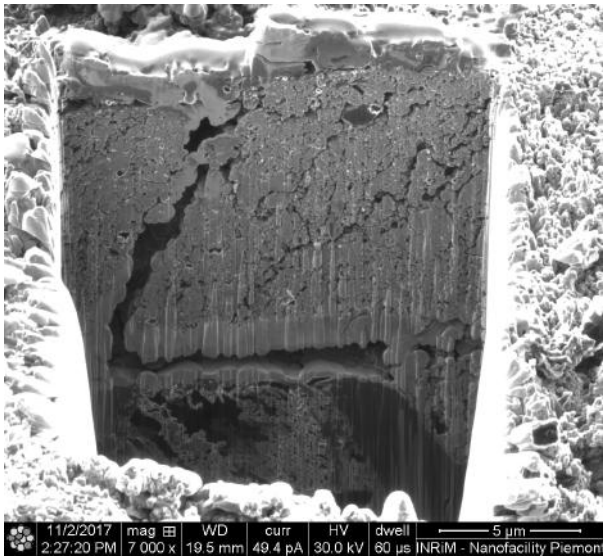

Figure 5.30: FIB section of secondary plateau.

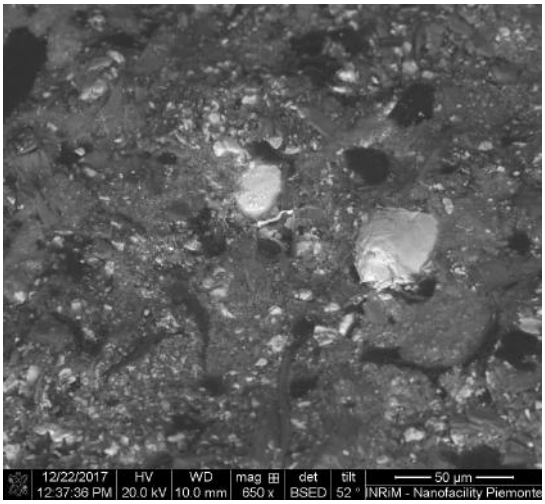

(a) Debris area.

(b) Debris FIB excavation.

Figure 5.31: Debris area, this area contributes marginally to friction.

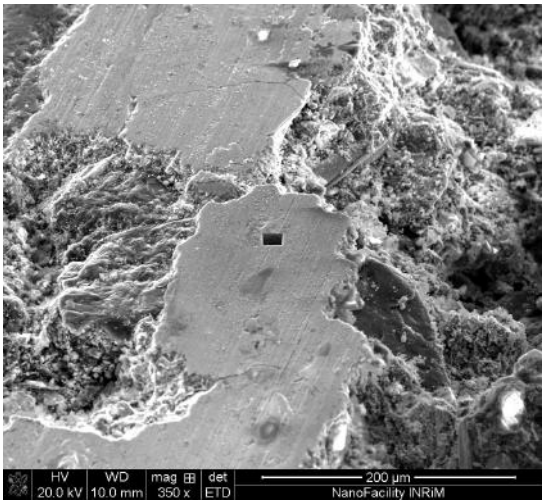

(a) Primary plateau area.

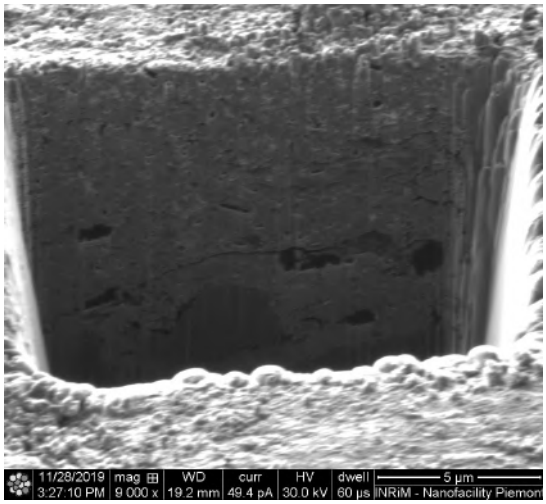

(b) FIB excavation on NAO primary plateau.

Figure 5.32: Primary plateau of NAO material.

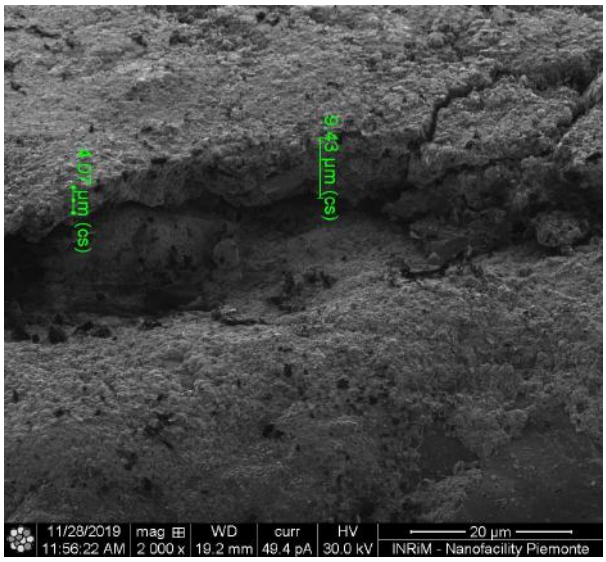

Figure 5.33: Third body layer thickness of NAO material.

increase of the maximum *FFT* peak increasing the humidity for the different materials. These trends confirm what reported in the chapter 2 about the increase of the *Stick-Slip* linked to the increase of the humidity and so of the menisci adhesive forces. It is possible to see that not all the materials have the same dependence on humidity.

5.6.7 Pads measurements comparison

The results of vehicle and dyno are compared with the tribometer ones in figure 5.35 and 5.36. From the graphs and the relative correlation index it is possible to see that a strong correlation between vehicle, dyno and tribometer exists. This is a good result and it means that, for *Stick-Slip* problems, it is fair to study friction materials on tribometer. The absolute values of the FFT mean between dyno, tribometer and vehicle are different because the rigidity of the systems are different. The braking system of a vehicle is cushioned therefore the values of the peaks of the vibration are lower. Dyno and tribometer have a simple and rigid shock absorber in order to amplify the mechanical vibration.

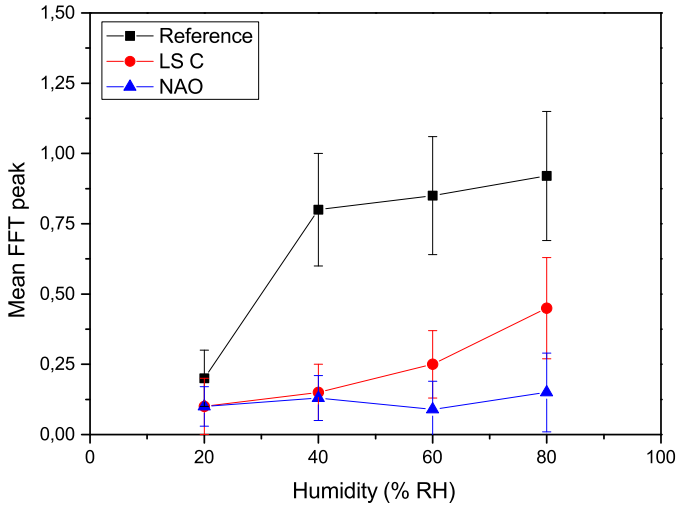

Figure 5.34: Humidity effect on *Stick-Slip* process. Amplitude is the mean maximum value of the FFT. As error is used the standard deviation. Data used for the analysis are only the ones at 100 N.

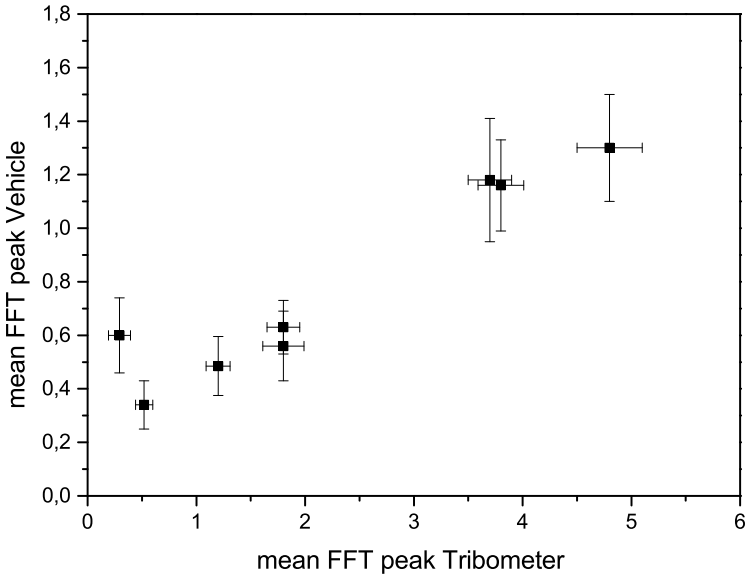

Figure 5.35: Results of tribometer compared with the ones on vehicle. The Pearson correlation index is 0.95.

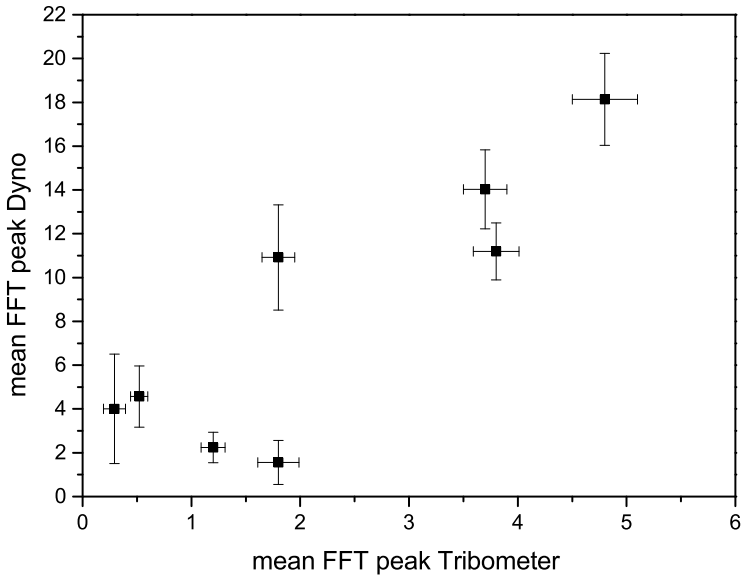

Figure 5.36: Results of tribometer compared with the ones on dynamometer. The Pearson correlation index is 0.86.

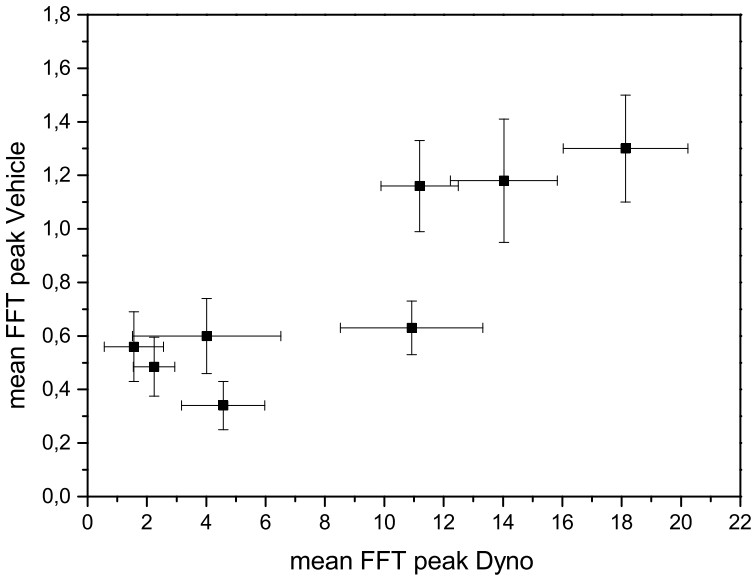

Figure 5.37: Results of vehicle compared with the ones on dynamometer. The Pearson correlation index is 0.87.

5.7 Test on NAO materials

5.7.1 CoF versus Time

From the data measured, graphs of the CoF versus time for the three different NAO materials studied were done, figure 5.38 shows three materials with significant difference in the *Stick-Slip* propensity. Going from top to bottom the relative humidity increases. Every column is relative to one material. The graphs show the *Stick-Slip* events, their numbers and amplitudes are different.

5.7.2 Analysis and results

The analysis for this test is done taking the mean amplitude of the *Stick-Slip* events, defined as the difference between the static and the dynamic CoF (Fig. 5.40). Since all the materials analyzed have *Stick-Slip* events at 80% humidity, only brakes at that humidity are analyzed and compared. At lower humidity only two materials showed *Stick-Slip* events. Figure 5.41 shows the reproducibility of the test. Sometimes the *Stick-Slip* phenomenon can appear even at 60% humidity, this obviously depends by the friction material. At low relative humidity the phenomenon is attenuated because the difference

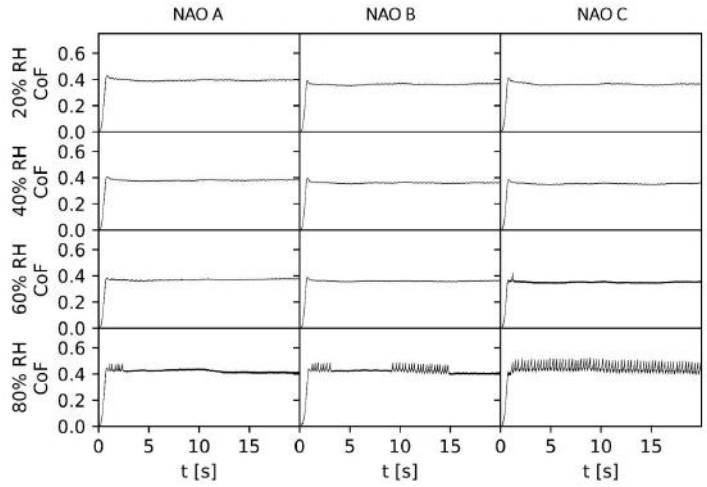

Figure 5.38: CoF versus time results for NAO *Stick-Slip* test.

between static and dynamic friction decreases as the meniscus force is lower. If the *Stick-Slip* occurs at different humidity levels, the contribution of the meniscus effects can be calculated. For instance NAO D shows *Stick-Slip* at 60 and 80% of relative humidity (Fig. 5.39), the amplitude mean of *Stick-Slip* at 80% is 0.063±0.004 (ΔCoF_{80}) and the amplitude at 60% is 0.039±0.003 (ΔCoF_{60}). From the equation 4.1 the friction force can be calculated. ΔF is the force difference between static and dynamic calculated by the ΔCoF; the difference between 80 and 60% of RH gives the information on meniscus force. Table 5.4 shows the difference between NAO D and E, NAO D creates stronger bonds with humidity. The adhesion interaction between primary plateau and the meniscus force are stronger in NAO D.

	ΔCoF_{60}	ΔCoF_{80}	ΔF_{60} N	ΔF_{80} N	ΔF_{80-60} N
NAO D	0.039±0.003	0.063±0.004	7.8±0.6	12.6±0.8	4.8±1.0
NAO E	0.040±0.004	0.051±0.002	8.0±0.9	10.2±0.4	2.2±0.9

Table 5.4: Friction force as a function of humidity.

This method can be a good indirect measurement of the effect of humidity on materials.
For each materials the mean amplitude is plotted versus its vehicle score (Fig. 5.42). Vehicle score is an evaluation from 0 to 10 that gives the driver to the material, the procedure for the evaluation of NAO is similar to Low Steel. The average and the standard deviation of five days is the final score of material. There is a good correlation

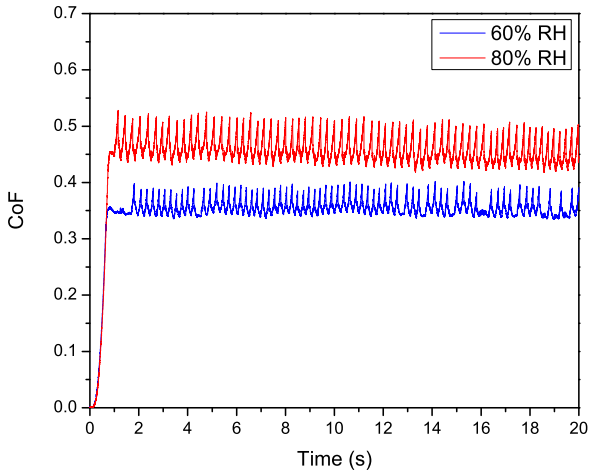

Figure 5.39: NAO D shows *Stick-Slip* events at 60 and 80% of relative humidity.

($\rho_{Pearson} = -0.95$) between this two method of analysis. Therefore, with this method, tribometer can be used in order to characterize NAO materials that until this moment are analyzed successfully only on vehicle.

5.8 Polyethylene pattern friction measurement

This work was carried out as part of the ITT-UniTo collaboration aimed at the preliminary study of the effects of a controlled morphology on friction. The work of my thesis was to create an experimental procedure for measuring the coefficient of friction in different conditions of pressure, sliding velocity and humidity. The results obtained were compared with an already existing theoretical model developed by Costagliola et al. [45]-[46] and a paper will be submitted to Tribology Internation Journal [47].

5.8.1 Introduction

Surface morphology plays an essential role in determining friction properties of surfaces in many engineering applications. For instance, in the automotive field (e.g. tires, brake pads, bearings and related technology), the surface morphology determines the static and dynamic friction [45]–[55]. Stick-slip phenomena [10] can generate mechanical vibrations leading to annoying noise; modification of surface topology can thus enable to reduce or eliminate this effect by varying the static and dynamic friction coefficients without changing the chemical composition of the surface. Surface grooves can reduce thus type of noise, as demonstrated by Wang [56]. Modification of the macroscopic friction properties

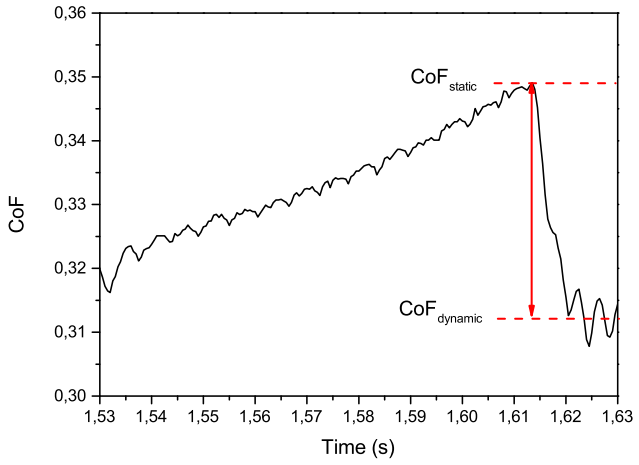

Figure 5.40: *Stick-Slip* amplitude definition (ΔCoF).

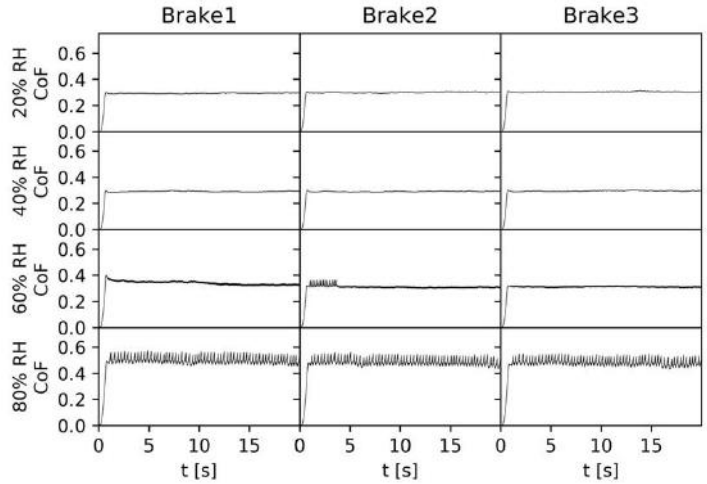

Figure 5.41: CoF versus time results for NAO *Stick-Slip* test. Three applications of the same brakes. This is the material NAO C.

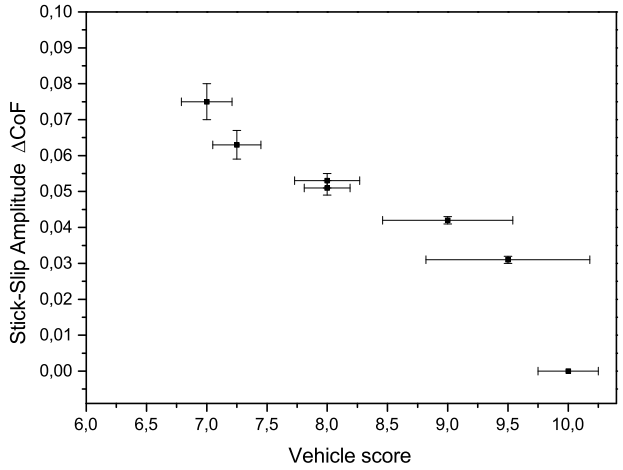

Figure 5.42: Comparison of NAO materials tested on tribometer and on vehicle.

can be observed by changing the microstructure of the surface, introducing for instance artificial patterns that allow tunability of tribological properties [45]–[55] and wear [57]. Friction surfaces work at different temperature and humidity conditions, the effect of humidity on friction was investigated (especially at high humidity regime). Maegawa et al. [15] studied the effect on kinetic friction of the number of surface grooves present on contact surfaces and found that friction decreased as the number of grooves increased. Capozza et al. [58] indicated that macroscopic surface grooves are theoretically effective in reducing static friction due to a non-uniform distribution of surface stress induced by patterning. However, since friction surfaces operate in different environmental conditions, the effect of patterning also needs to be evaluated in the presence of varying temperature and humidity. Bhushan et al. [13] have shown that there are different regimes as a function of the amount of water present between the surfaces. Hence if the surface geometry changes, e.g. in the presence of grooves or cavities, regimes can vary with the same amount of water. Meniscus forces strongly depend on the distribution of asperities and the amount of water [13]-[5].
In this section it is reported the study of the effect of surface morphology modification at the micrometer scale on both static and kinetic friction, using laser patterning to create a periodic array of cavities on the contact surface. The samples under study are of polyethilene, which is considered as a material suitable for this study, by virtue of its well-known mechanical properties, good machinability and during the test it does not change the surface of its tribological counterpart made of gray cast iron. The system is characterized experimentally using a tribometer, and the surface morphology is determined using a profilometer. The coefficient of friction is calculated as a function

of sliding velocity, normal force and relative humidity, especially in the high humidity regime. Experimental data are compared to the predictions of a numerical 2-D model developed previously by some of the authors [60]-[46].

5.8.2 Materials and methods

The chosen material for the samples is low-density polyethylene due to its well-known mechanical properties and good machinability, as well as its limited wear effects on its tribological counterpart made of gray cast iron. Two types of polyethylene samples have been tested: the first is nominally flat and the second is patterned. The geometry of the samples is circular, both have a diameter of 1 cm and a thickness of 0.7 cm. The Young's Modulus of the material is (0.38±0.08) GPa.
Surface micro-patterning was performed with a ns pulsed Nd:YAG laser (EzLaze3 by New Wave); the laser wavelength is in the infrared range ($\lambda = 1064$ nm). The pattern is a lattice of square cavities whose side is about 130 μm long. The distance between cavities is about 370 μm in x and y directions. Using two bursts for each cavity, the obtained depth is 5.2±1.3 μm. The pulse duration is 4 ns, the spot size is 23 μm and the power density is 3.65 GW/cm^2. Figure 5.43 shows the altitude map of the patterned surface and the depth profile obtained by an optical profilometer.

5.8.3 Numerical simulation background

To support the interpretation of experimental results by means of a simplifield numerical approach, the spring-block model [61] is used, which has been already adopted to investigate frictional phenomena [62][63]. In [46], the model was implemented in a 2-D formulation to model the horizontal contact plane and study the effects on friction due to the surface pattern geometry. This formulation is particularly useful in investigating static friction and the behavior at the onset of sliding, but is less effective in describing dynamic friction. In particular, results in [46] for the dynamic friction coefficient of surfaces with square cavity arrays do not match the observed experimental results in this work (e.g. figure 5.52).

For this reason, the 2-D discetization of the substrate is considered in the vertical plane, similarly to the approach adopted in [63], in order to take into account the vertical stress distribution. Since the presence of surface structures induces stress concentrations, it is expected that this may play a role in determining the dynamic friction behaviour. Although this approximation neglects the 2-D pattern geometry on the horizontal contact plane, it is preferred to avoid a computationally expensive 3-D formulation. Thus, the cavities are approximated along their vertical profile shown in figure 5.50.

The system is modelled as follows: the lower layer of the sample is discretized by means of a 2-D spring-block square mesh, in which each block is attached to its eight neighbors by means of linear springs, while the remaining bulk portion is considered as

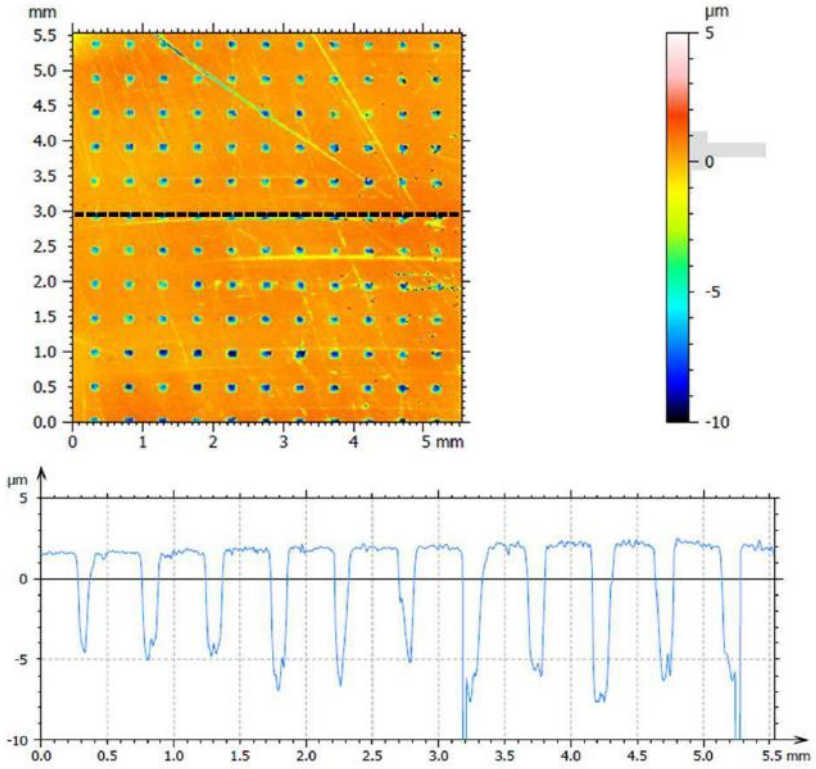

Figure 5.43: top - optical images of the patterned surface. bottom - depth profile along the black line shown in the optical image (depth profile extracted at height y of 3 mm). To the left of the color scale is the histogram of the height distribution.

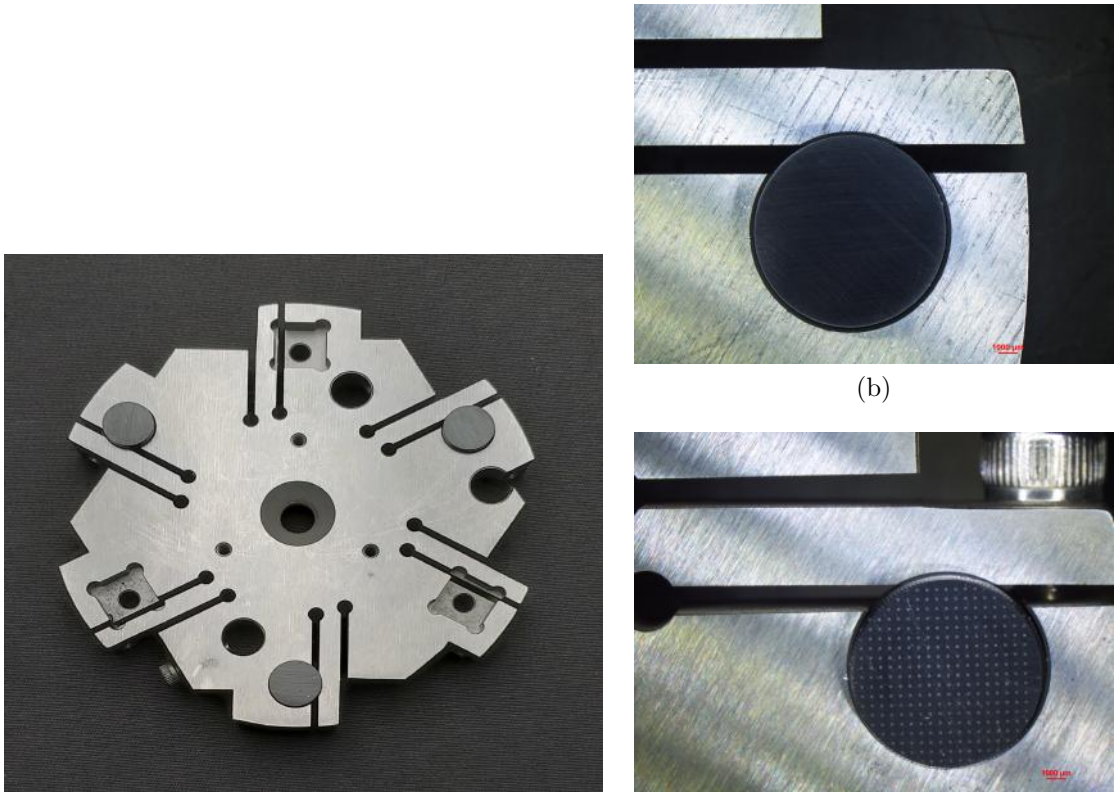

(a) (b) (c)

Figure 5.44: Tribometer sample holder (a), flat (b) and patterned (c) polyethylene sample fixed on the tribometer sample holder. The effective radius is $r_{eff} = 38.1$ mm.

a single rigid block, as shown in figure 5.45. It is assumed that in the pressure and velocity ranges considered experimentally the effects due to this bulk approximation are negligible. A uniform pressure P is applied along the vertical axis to the bulk, which moves at constant velocity v along the horizontal direction. The system slides over a rigid undeformable surface, reproducing the geometry of the experimental apparatus of a polyethilene sample sliding over cast iron.

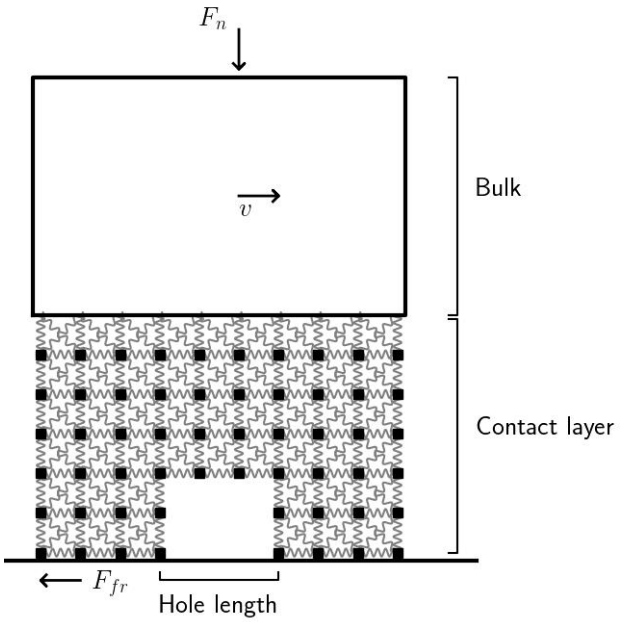

Figure 5.45: Schematic of the 2-D spring-block model adopted to approximate the experimental apparatus.

The dicretization length to $l = 10\ \mu m$ is fixed, which is small enough to take into account the cavity depth and large enough to introduce an effective friction law like on a elementary surface unit represented by the block. Qualitative behavior in not affected by this value. Given the density of the polyethylene $\rho = 0.9$ g/cm^3, the mass of each block is $m = \rho l^3$, while it is fixed to $m/2$ for blocks located on edges of the mesh and $m/4$ for those on the corners. The stiffness can be fixed by imposing the equivalence with an isotropic elastic material with Young's modulus E (For polyethylene $E = 3.8$ GPa) with the procedure illustrated in [64]. Thus, the stiffness is $k = 3/4El$ and is halved for diagonal springs. In this mesh, the value of the Poisson's ratio is fixed to $\nu = 1/3$, which is reasonably close to the realistic value.

The internal elastic force applied to a block i by its neighbor j is $\mathbf{F}_{int}^{(i,j)} = k_{ij}(r_{ij} - l_{ij})(\mathbf{r}_j - \mathbf{r}_i)/r_{ij}$, where $\mathbf{r}_i$, $\mathbf{r}_j$ are the position vectors, r_{ij} is the modulus of their distance, k_{ij} is the stiffness of the spring connecting them and l_{ij} is the modulus of their rest

distance. The springs between the upper row of blocks and the rigid bulk portion transmit the forces to all underlying blocks due to the normal pressure and the velocity imposed to the bulk portion.

Each block is subjected to viscous damping term to avoid artificial oscillations, $\mathbf{F}_d^{(i)} = -\gamma m \dot{\mathbf{r}}_i$, where γ is the damping frequency. If γ is equal to $\gamma = 10^{-2}\sqrt{k/m}$ the regime is underdamped. This choice does not affect qualitative results [63].

Thus, the only forces applied to the blocks are the elastic force due to the neighbors and the damping, except for those located on the bottom row which are subjected to a friction force. This layer is constrained to horizontal motion along the substrate. In any case, it has been verified that relaxing this condition does not lead to detachment with the chosen parameters.

A local static and a dynamic friction coefficient is assigned to each block i in contact with the substrate, namelyμ_s^i and μ_d^i, respectively. These are randomly extracted at the beginning of the simulation from a Gaussian distribution with means $(\mu_s)_m$, $(\mu_d)_m$ and standard deviations (σ_s), (σ_d).

In the standard formulation, the local friction force is determined by the classical Amontons-Coulomb (AC) friction force, i.e. a force proportional to the total normal forces acting on i due to its neighbors. In symbols, the vertical component of the total internal elastic force on i is $F_n^i \equiv \sum_j F_{int}^{ij}|_y$. Thus, if a block is at rest, the static friction force is opposite to the horizontal forces acting on i, i.e. $F_{fr} = -\sum_j F_{int}^{ij}|_x$, up to the threshold $F_{fr} = \mu_s^i F_n^i$. If the block is moving, the dynamic friction force is $F_{fr}^i = \mu_d^i F_n^i$ in modulus and opposite to its velocity.

As discussed below, this simple AC friction force is inadequate to reproduce the experimental results and needs to be modified. Whatever the adopted friction force $\mathbf{F}_{fr}^{(i)}$ is adopted, the Newton's law for a block i can be written: $m\ddot{\mathbf{r}}_i = \sum_j \mathbf{F}_{int}^{(ij)} + \mathbf{F}_{fr}^{(i)} + \mathbf{F}_d^{(i)}$. By numerically integrating the whole system of equations with a fourth-order Runge-Kutta algorithm, the time evolution and all the physical quantities can be calculated. An elementary time step $dt = 10^{-9}$ s in sufficient to avoid integration errors.

Simulations are actually performed in two steps: first the normal force is applied with velocity $v = 0$, increasing the force from zero to the chosen value in a short but finite time. This avoids numerical instabilities due to the abrupt force application. It has been found that increasing the force in an interval of $2 \cdot 10^{-6}$ s is sufficient for this purpose. Then, the force is kept constant for further 10^{-5} s, which are sufficient to damp internal oscillations and dissipate the kinetic energy of the mesh. After the system is stabilized, the velocity is switched to the experimental value v.

Pressure and velocity are the same as in the experiments, with $v = 2$ mm/s and pressure between $P = 0.65$ MPa corresponding to the experimental case of 50 N, and $P = 2.6$ MPa for the case of 200 N. The number of blocks are fixed by the elementary length l and the real experimental specimen length: the height of the contact layer is fixed to 20 blocks, corresponding to 200 μ m, which is sufficiently large compared with

the cavity depth. The length of the system is 996 blocks, so to approximately match the experimental sample length of 1 cm. In the patterned case, the length of each cavity in the mesh is 130 μm and the depth is fixed to 20 μm.

The local friction coefficients are also tuned to obtain a macroscopic behavior comparable with the experimental one. Thus, the set of four variables determining the local distribution has been adjusted once and for all in preliminary tests. These values depend on the selected friction law, so that this will be discussed in the next section.

Calculation of the effective contact area

In theoretical and numerical models, the effective contact area is usually assumed proportional to the applied load, leading to the classical AC friction law [65]. However, in the case of the patterning, there is a non-uniform vertical stress distribution on the contact surface characterized by concentrations located at each cavity edge, as shown in figure 5.46. Thus, in the flat case, stress concentrations are only located at the edges, while in the patterned case they occur all along the surface.

For this reason, it is expected that, in the presence of corrections to the linear behavior of the contact area with the pressure, these will affect much more the friction of the patterned surface than of the flat one, leading to an effect on the dynamic friction observed experimentally. To verify this scenario, the behavior of the effective contact area with the load for our polyethylene sample is investigated.

The surface profile of the flat sample before the test shown in figure 5.49 is considered. In order to calculate the effective contact area with the load, the software TAMAAS [67] is used, a freely available high-performance code based on boundary and volume integral equations [66]. A model of linear elasticity is assumed for the sample, while the only external parameters are the Young's modulus E, the Poisson's ratio ν and the sample length. The software calculates the effective contact area as a function of the applied pressure P.

Results for the flat sample are shown in the left panel of figure 5.47: a deviation from a linear behavior is observed for increasing pressure, in particular the curve saturates for pressures whose order of magnitude corresponds to that estimated with the model. These results are not affected by the scale of the sample, i.e. repeating the test for portions of the surface. Given this result, it is supposed that the effective contact area corresponding to our elementary block does not scale linearly with the load, but saturates for larger pressures. Thus, the standard friction force in the spring block model must be modified.

Therefore a linear AC friction law is assumed up to a threshold corresponding to the smallest experimental pressure: from this a law proportional to the effective contact area is assumed. In symbols, given the static or dynamic friction coefficient, the friction force is $F_f r = \mu^i F_n^i f(P)$, where $f(P) = 1$ for $P < 0.7$ MPa, while for larger pressure $f(P)$ is proportional to the deviation from the linear law of the area fraction. Since this factor is calculated numerically for a finite number of values of P, the value for a generic

pressure in the middle of a range between the calculated ones is linearly interpolated. The behavior of the $f(P)$ obtained is shown in the right panel of figure 5.47.

Once the friction law is fixed, the friction coefficient is tuned so that the dynamic friction coefficient of the flat surface is as close as possible to the experimental one. After preliminary tests, the averages of local friction coefficients is fixed to $(\mu_s)_m = 0.3$, $(\mu_d)_m = 0.27$, and their standard deviations to 5% of the average.

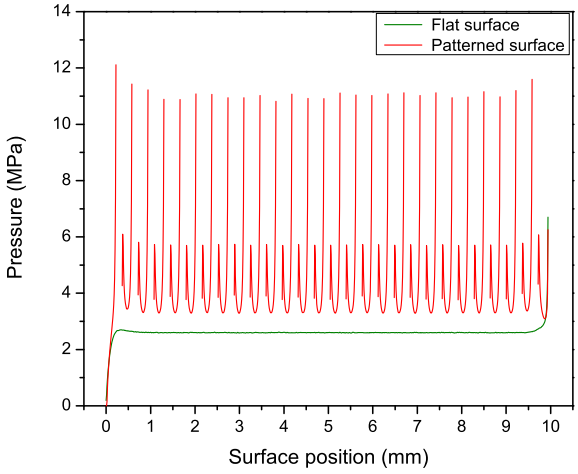

Figure 5.46: Comparison of the local pressure distribution for patterned and flat case during the sliding with a total normal force applied of 200 N.

5.8.4 Results

Friction coefficients of flat and patterned surfaces

The dynamic friction coefficient (CoF) is evaluated as a function of sliding velocity, force and relative humidity. As an example, figure 5.48 shows the output of tests performed on flat and patterned sample the CoF applying a normal force of 200 N, sliding speed of 2 mm/s and RH=15 %. Results for a flat sample are presented in table 5.5. Normal force and pressure P are related by the following relationship:

$$P = \frac{F_n}{\pi r^2} \tag{5.8}$$

where r is the radius of the tribometer sample (r = 0.005 m).

Each test is repeated three times, and the corresponding average and standard deviation is calculated for each measurement (considering CoF values between 10 and 40

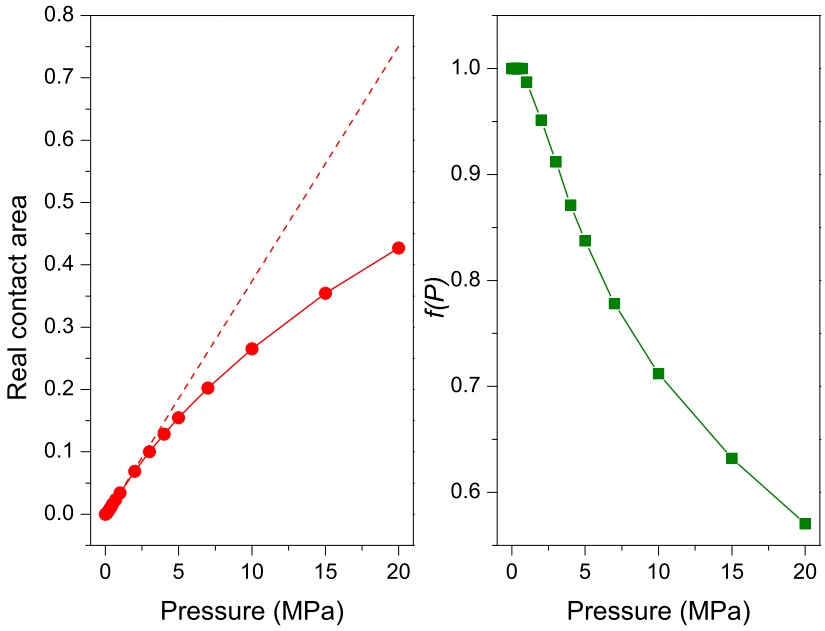

Figure 5.47: Left: Effective contact area as a function of pressure obtained with TAMAAS [67] for the flat sample surface of figure 5.49. The dashed line represent a linear behavior starting from the chosen threshold 0.7 MPa. Right: correction factor $f(P)$ to modify the AC local friction law.

seconds). Results show that the CoF increases when the sliding speed increases, and also when the relative humidity increases. Results for the patterned sample are presented in table 5.6.

The CoF of this sample always displays a smaller dynamic CoF than the flat sample. This is consistent with results by Maegawa et al. [15], who demonstrate that the number of cavities is fundamental in determining the CoF. This is due to stress accumulation at the edges of the cavities, which leads to facilitated detachment. The CoF of the patterned sample decreases by (18±3) % compared to the flat sample at 15 % relative humidity.

Altitude maps show no significant differences before and after the test in the tribometer, both for flat and patterned samples The cavity profiles are unchanged after the test (figure 5.50). The surface roughness of the samples undergoes slight changes due to the test, with the introduction of micro scratches parallel to the direction of sliding.

Normal force - Speed	15% RH	40% RH	80% RH
50 N - 2 mm/s (0.5 RPM)	0.248±0.002	0.269±0.004	0.225 ±0.02
100 N - 2 mm/s (0.5 RPM)	0.263±0.005	0.271±0.003	0.276±0.008
150 N - 2 mm/s (0.5 RPM)	0.271±0.002	0.279±0.002	0.296±0.002
200 N - 2 mm/s (0.5 RPM)	0.278±0.001	0.282±0.001	0.303±0.002
100 N - 0.4 mm/s (0.1 RPM)	0.264±0.003	0.265±0.007	0.30±0.01
100 N - 4 mm/s (1 RPM)	0.287±0.002	0.294±0.002	0.319±0.005

Table 5.5: Friction coefficient of a flat sample as a function of normal force, sliding velocity and relative humidity. All measurements are performed at room temperature.

Normal force - Speed	15% RH	40% RH	80% RH
50 N - 2 mm/s (0.5 RPM)	0.208±0.007	0.211±0.002	0.250±0.002
100 N - 2 mm/s (0.5 RPM)	0.218±0.005	0.218±0.005	0.268±0.007
150 N - 2 mm/s (0.5 RPM)	0.223±0.004	0.220±0.002	0.265±0.003
200 N - 2 mm/s (0.5 RPM)	0.224±0.002	0.219±0.001	0.265±0.003
100 N - 0.4 mm/s (0.1 RPM)	0.200±0.002	0.196±0.002	0.263±0.003
100 N - 4 mm/s (1 RPM)	0.240±0.002	0.238±0.002	0.285±0.002

Table 5.6: The friction coefficient is evaluated as a function of normal force, sliding velocity and relative humidity. All the measurements are done at room temperature. Pattern sample.

Simulation results

By performing numerical simulations with the modified friction law, the results shown in figure 5.51 is obtained. Curves are qualitatively similar to the experimental behavior. The macroscopic dynamic friction coefficient, obtained from the time average over the dynamic phase, is smaller in the patterned case compared to the flat case. In the patterned case, points located near the edges are subjected to larger pressure, but due to the non-linearity of the friction force, they experience a reduced friction force. Thus, the non-linear behavior of the local friction law, with the non-uniform pressure distribution on the contact area, is crucial to explain the experimental observation with the current model. Quantitative results depend on the arbitrary parameters, in particular the local friction coefficients and the pressure threshold from the linear to the non-linear behavior. Moreover, a perfect match of the curve and the coefficients cannot be obtained given the two-dimensional approximation. However, this result cannot be obtained in numerical simulations with a standard AC friction law by modifying all other arbitrary parameters, e.g. discretization length or local friction coefficients.

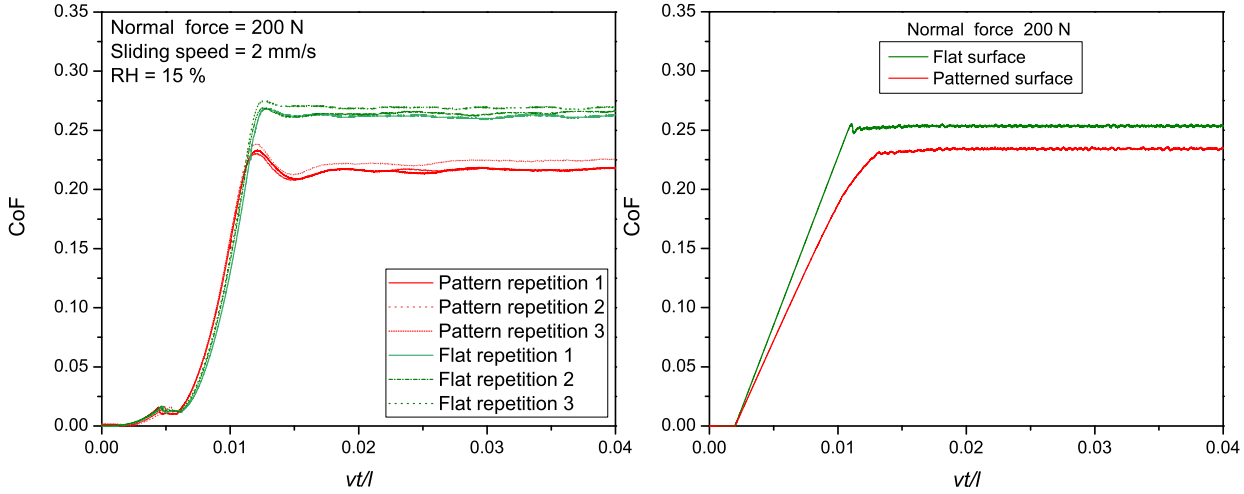

Figure 5.48: Comparison of the time evolution of the friction coefficient for the nominally flat and patterned cases, with $v = 2$ mm/s, RH=15% and total normal force 200 N, obtained from experimental test (left) and numerical simulations (right). Three repetitions are shown for experimental tests, showing good reproducibility.

Humidity effect

The CoF increases with humidity, especially for large relative humidity values (80 %). It is interesting to note that for a normal load of 50 N, the CoF of the flat sample decreases at high humidity levels, which means that the surfaces are in an immersed regime [13]. If the normal force is increased further, the excess water is eliminated from the interface. In the patterned sample, the water can be removed more easily from the surface due to the cavities, so that more water is required to obtain an immersed regime compared to the flat sample. Due to the cavities, the excess water on the surface enters the cavities, so that the effect of relative humidity at 40 % is negligible in the patterned sample.

Sliding velocity dependence

The CoF increases with sliding speed, and the patterned sample is most affected by the effect of sliding velocity. All tests were carried for a normal load equal to 100 N. Figure 5.53 shows the friction values as a function of sliding speed. The only exception is for the flat sample at 80 % humidity.

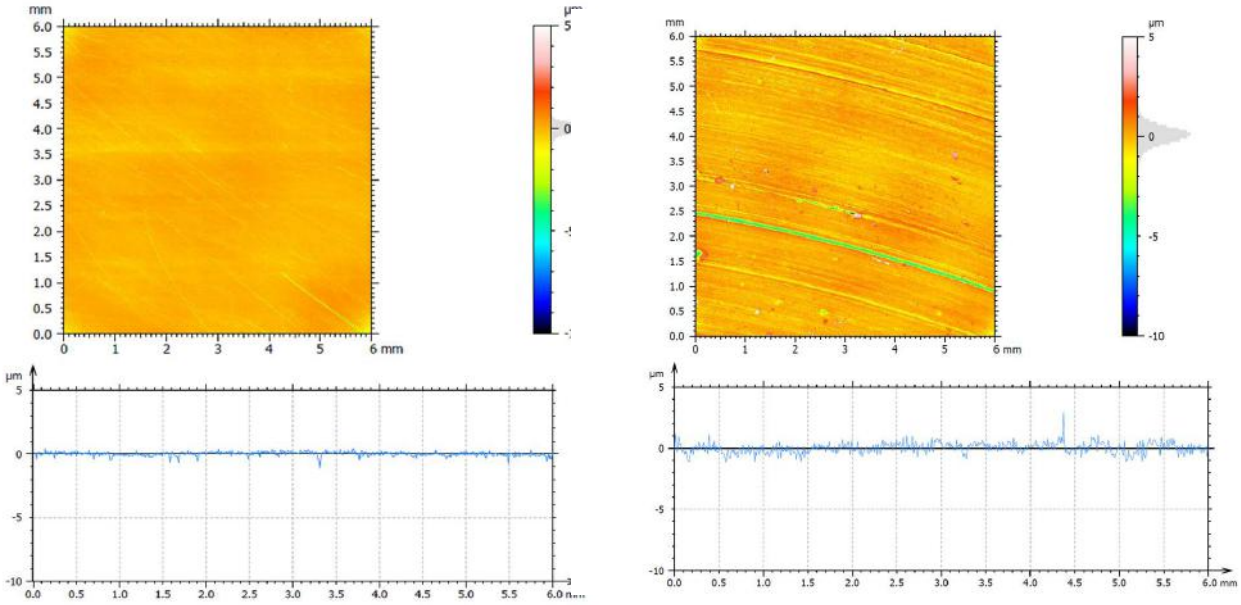

Figure 5.49: Topology of a flat sample. (left) altitude map before test in the tribometer, (right) after the test. top - altitude map of the patterned surface. bottom - depth profile extracted at height y of 3 mm.

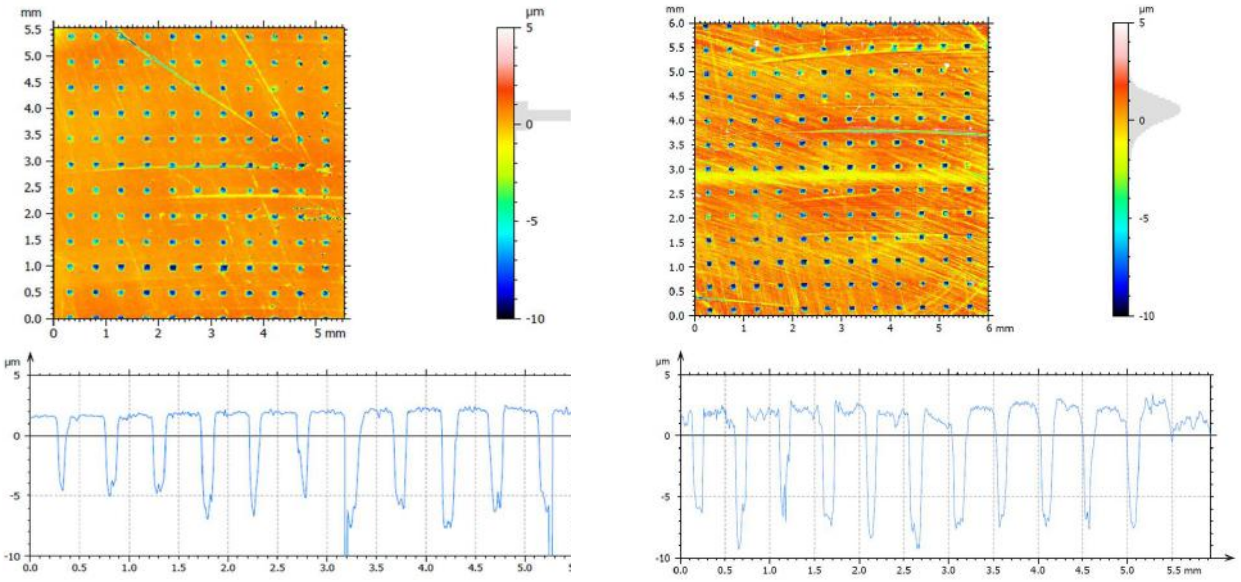

Figure 5.50: Profilometry of the patterned sample. (left) before test in the tribometer; (right) after the test. top - altitude map of the patterned surface. bottom - depth profile extracted at height y of 3 mm.

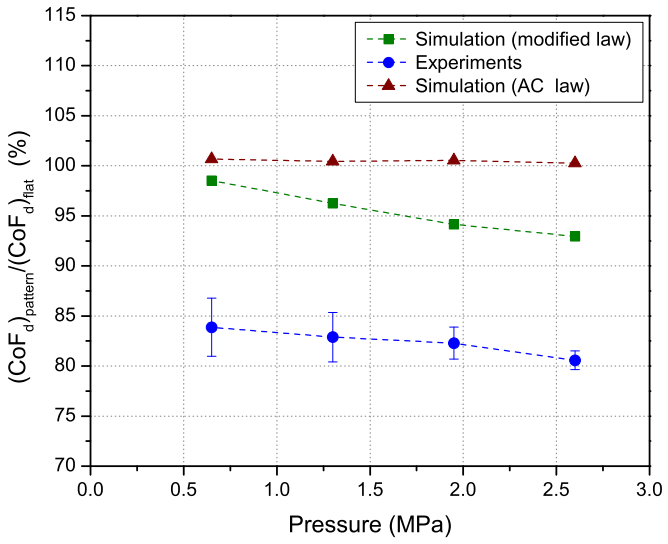

Figure 5.51: Rigth: Comparison between simulations and experiments of the ratio of patterned and flat dynamic friction coefficient as a function of the pressure.

Stick-Slip

The onset of a stick-slip regime occurs in the high humidity regime (80 % of relative humidity) due to the meniscus forces that are created between the surfaces. Stick-slip occurs at different normal load and sliding velocity values for flat and pattern samples. An important effect of sample patterning is that in addition to reducing the CoF, it also influences the stick-slip phenomenon. This occurs at different loads and sliding speeds for flat and patterned samples. The patterned sample displays stick-slip at lower loads and sliding speeds. This is due to the interplay between stress concentrations on the surface and the influence of humidity. The amplitude of stick-slip (ΔCoF) is smaller for the patterned sample, indicating a smaller difference between static and dynamic CoF. Figure 5.54 (right) shows the difference between ΔCoF of pattern and flat sample.

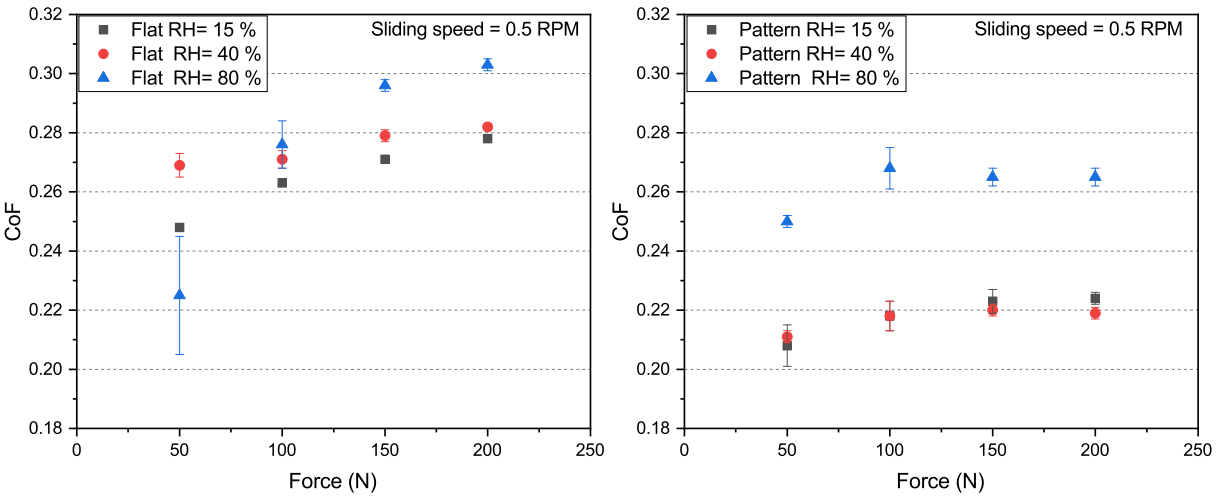

Figure 5.52: CoF for flat and patterned samples as a function of normal load and relative humidity.

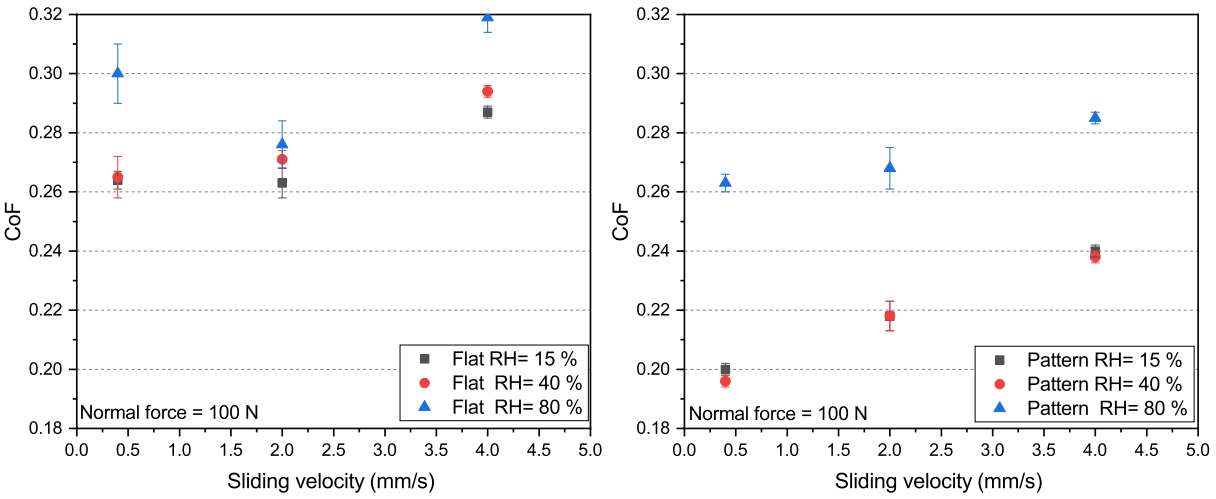

Figure 5.53: CoF for flat and patterned samples as a function of sliding speed and relative humidity.

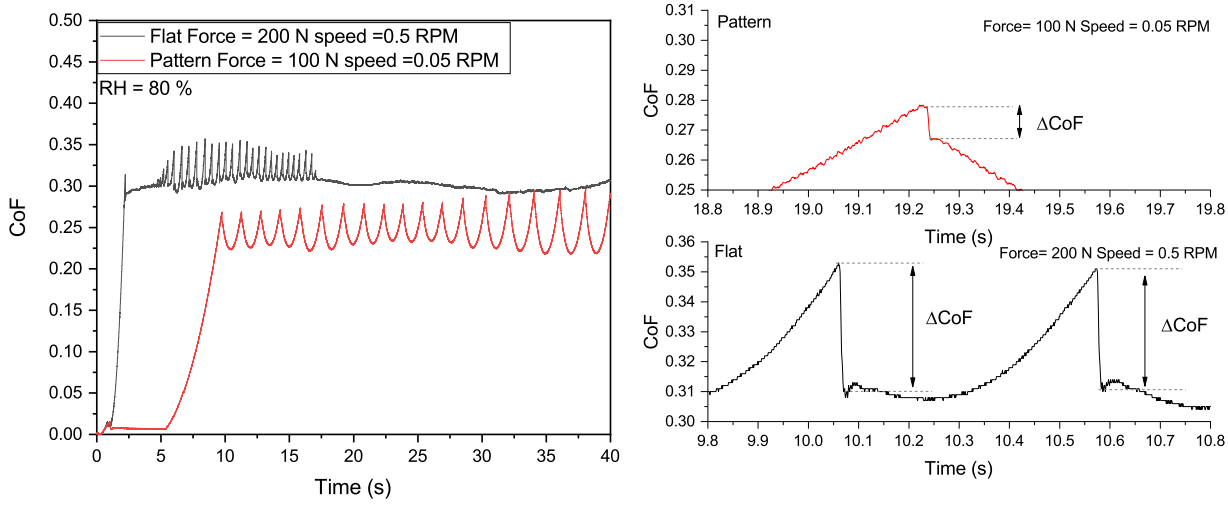

Figure 5.54: (left) Stick-slip phenomena in tribometer tests. (right) Close-up of stick-slip events. The stick-slip amplitude decreases for the patterned sample.

5.9 Tested materials: Noise propagation

Nowadays there are 13 underlayers (UL) used commercially by ITT. The goal is to characterize the damping properties as a function of the stress frequency and temperature (see Par. 3.2.4). Using the DMTA technique it is possible to study the behavior of the underlayer only; using the FRF technique, the behavior of the underlayers inside the brake pad is studied; 13 batches of 20 brake pads have been molded, all batches have the same friction material but different underlayer. For the DMTA 13 batches of 10 circular shape were molded (see Par. 4.9.3).

The 13 materials tested are identified with alphabetic letters: A,B,C,D,E,F,G,H,I,L,M,N and O; the circular sample of only underlayer A will be identified as UL A, the brake pad with underlayer A will be identified as A-PAD.

The underlayers are composed of:

- Rubber or blend of rubbers, it provides the damping properties;
- Phenolic resin, it binds the raw materials;
- Steel and organic fibers, they give the suitable mechanical and structural properties;
- Filler, it lowers the cost of the mix.

In the following table there are the main differences to be analyzed:

Underlayer	Rubber 1 %	Rubber 2 %	Rubber 3 %	Rubber 4 %	Rubber 5 %
A	100				
B		100			
C	48	52			
D	22	78			
E	42	58			
F		52	48		
G	42	58			
H		62	38		
I	45		55		
L				100	
M				100	
N				100	
O					100

Table 5.7: The underlayers have different rubber composition, the percentage refers to the total composition considering only the rubber family.

The first step of the analysis is to characterize the damping properties of the rubber. The rubber 1 is a copolymer of butadiene acrylonitrile (NBR) [39], its operating temperature range is between -40 and 130 °C, this rubber has good physical-mechanical properties and good resistance to hydrocarbons. The rubber 2 is a copolymer of ethylene acrylate (ACM), its operating temperature range is between -30 and 150°C, it has an excellent resistance to oils and is impermeable to air and other gases. The rubber 3 is a copolymer of chlorinated isobutylene and isoprene (CIIR), it has a very dense molecular structure which guarantees high impermeability to many gases and good resistance to breakage and abrasion; its operating temperature range is between -50 and 150 °C. The rubber 4 is powder of NBR. The rubber 5 is again NBR but it has a vulcanizing agent[3].

Figure 5.55: All the rubbers have this shape, only rubber 4 has not this shape, the latter is in powder form.

The second step is to characterize the damping properties of the underlayers, and finally, develop new underlayers formulas with new rubber.

5.10 Standard deviation evaluation

- **Instrument error**, it is evaluated using the same sample and repeating the test several times;

[3]In the vulcanization process natural rubber loses its intrinsic plasticity characteristics and acquires the properties of an elastic material. Generally the process consists of heating the rubber with sulfur, this creates transverse bonds between the chains of the macromolecules [40].

- **Dispersion in the batch**, the measurement is performed on samples from the same batch;
- **Dispersion among batches**, the measurement is performed on samples of the same material but from different batches.

Repeatibility is the necessary condition to evaluate the instrument error. However, this is not possible, since tests are destructive. DMTA is a destructive measure; heating the UL specimen up to 150 °C creates a thermal history. The resin has enough energy to further crosslink and part of the rubber is degraded. The only source of dispersion that is reasonable to evaluate is batch dispersion. Dispersion between batches is time consuming, information on the quality of raw materials would be obtained, but this is not the aim of the thesis.
The measurement dispersion in the batch is evaluated for each technique used. DMTA is very time and energy consuming so only dispersion on UL A has been evaluated.

5.11 DMTA data acquisition

This section shows the results obtained on the analysis of rubbers and underlayers. In the following paragraphs, extrapolation to a wider frequency range will be considered using the WLF theory (see Par. 3.2).

5.11.1 DMTA data acquisition of rubber

The analysis on the rubber is performed with the parallel flat plates geometry. The rubber is glued between the two plates. Rubber 1,2 and 3 have been tested (Fig. 5.57), for the other rubbers it was not possible to perform the analysis as they are powder tires and there is no suitable setup.
The values of E' are calculated (storage modulus) and E" (loss modulus); damping (tan δ) is calculated from their ratio. The tan δ peak corresponds to the glass transition, during the transition the elastic and viscous modulus are out of phase.

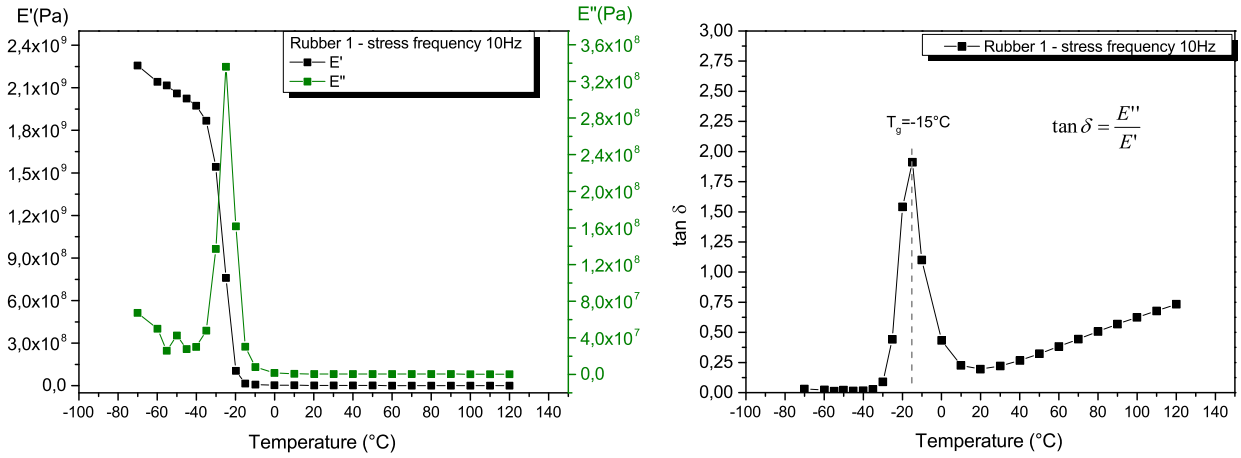

Figure 5.56: On the left, E' and E" as a function of temperature of the rubber 1. On the right, the damping as a function of temperature. The stress frequency is 10 Hz.

Figure 5.56 shows on the left, the values of the elastic and viscous modulus as a function of temperature. By increasing the temperature there is a glass transition and therefore a decrease in E' and an increase in E" (see Fig. 3.7).

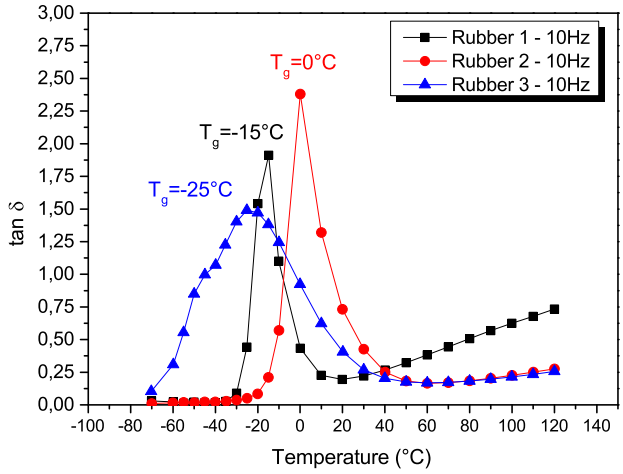

Figure 5.57: Damping as a function of temperature for the three rubbers analyzed. The temperature range is from -70 to 120 °C, the stress frequency is 10 Hz.

Rubber 3 has a glass transition at a lower temperature; the glass transition is influenced by the stress frequency. Generally in polymers, the glass transition ranges from 5

to 7 °C for each decade in stress frequency [41] (Fig. 5.58).

	T_g 1Hz (°C)	T_g 10Hz (°C)	T_g 111Hz (°C)	σ_{T_g} (°C)
Rubber 1	-20	-15	-10	5
Rubber 2	0	0	10	10
Rubber 3	-35	-25	-10	5

Table 5.8: Glass transition as a function of stress frequency. The error σ_{T_g} of the measurement is the temperature step of the procedure.

Rubber 2 has higher tan δ values than the other two rubbers analyzed, rubber 3 has lower glass transition and its damping curve is broad as a function of temperature.

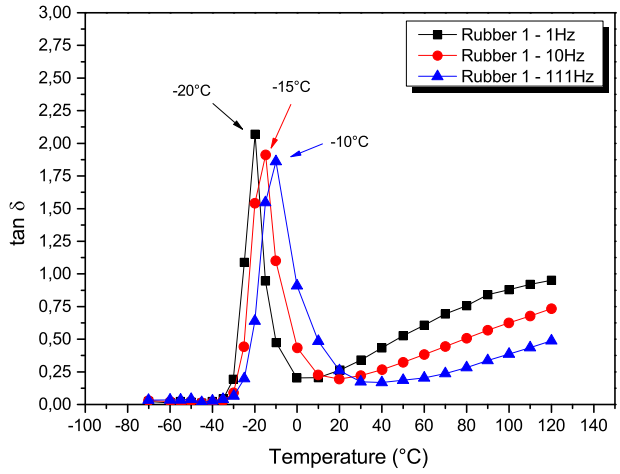

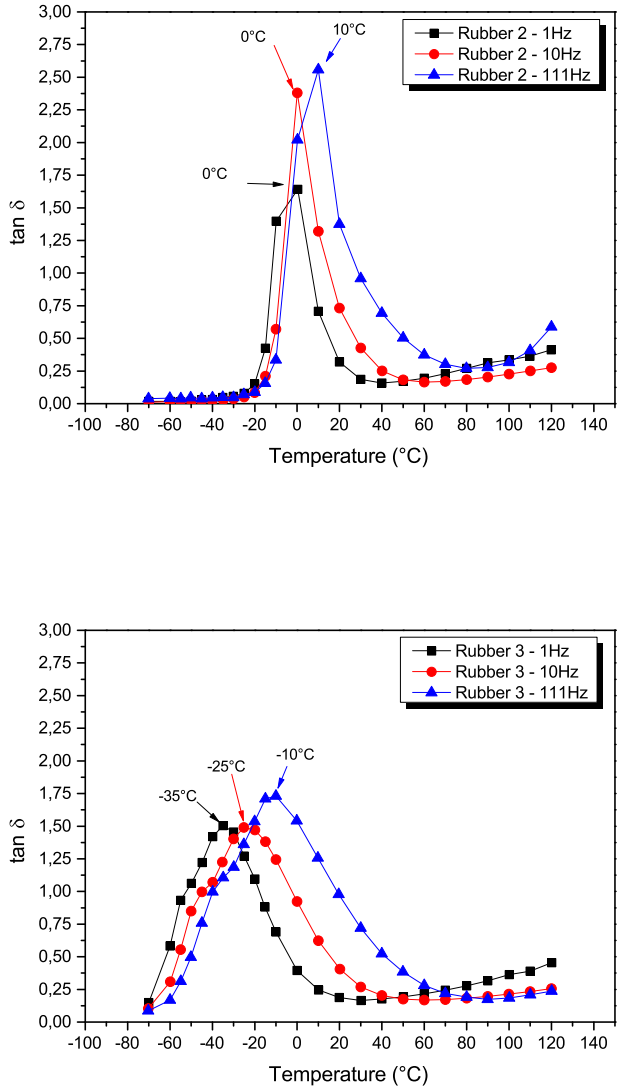

Figure 5.58: Damping as a function of temperature for three decades of stress frequency. Temperature range from -70 to 120 °C.

5.11.2 DMTA data acquisition of underlayer

UL analysis is performed with three-point bending setup, the reference curve is at a stress frequency of 10 Hz. The UL damping curves are in agreement with the UL rubbers composition; in the following figures the green lines and dots are the UL damping curve, rubber 1 is black, rubber 2 is red and rubber 3 is blue. The y axes for UL and rubber are different. The UL has lower damping value because the other raw materials in the

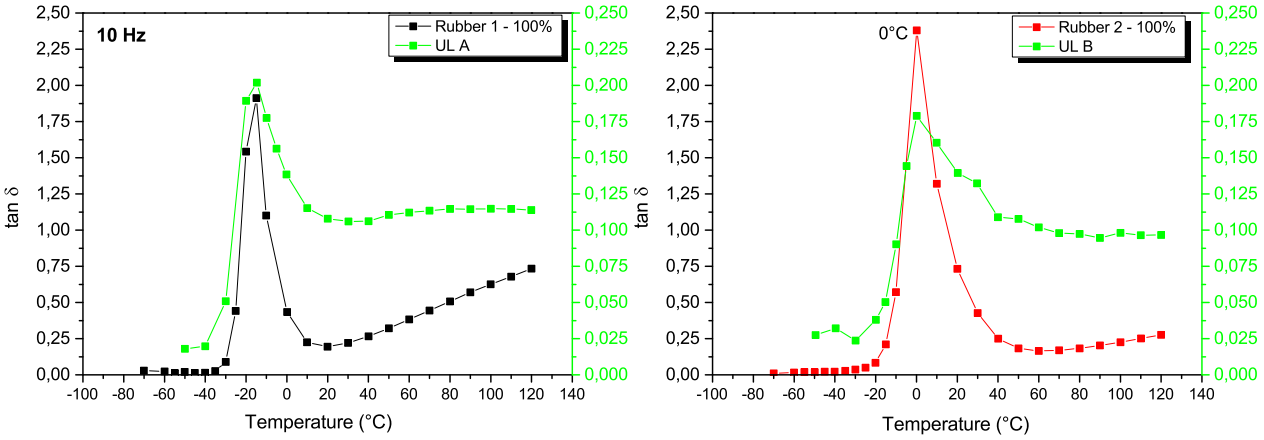

Figure 5.59: UL with single rubber composition; the glass transition temperature of UL and rubber are equal. The stress frequency is 10 Hz.

mix. For instance, steel fibers increase the elasticity of underlayer and resin decreases the damping properties.

Different rubber compositions have different damping behavior. In UL with a single rubber, the glass transition temperature of UL and rubber are equal (Fig. 5.59). In UL with a blend of rubber, the glass transition changes as a function of the percentage of rubbers (see Fig. 5.60).

The peak value of the glass transition change as a function of rubber. The glass transition for UL with a blend of rubber is driven by the high temperature glass transition rubber. The rubber with lower glass transition in the blend increase the tan δ in the low temperature range (Fig. 5.61). For example the UL I has rubber 3, so the damping under -40 °C is higher than UL A, which has only rubber 1, but the temperature of the glass transition is equal to rubber 1.
The UL with rubber 4 (rubber not tested because there isn't the setup for powder rubber) has the same glass transtion temperature of NBR (rubber 1).

UL O includes the vulcanized rubber 5, therefore there are cross bonds in the polymer chains. Its damping as a function of temperature doesn't show a peak (Fig. 5.62), this is due to the presence of the vulcanizer, which stiffens the structure. UL O is an aftermaket product, so this is not a good material for damp the vibration (this is a low-cost material).

5.11.3 DMTA data acquisition of friction material

Friction material can be analyzed using DMTA analysis. The procedure for analyze the friction material is similar to the UL procedure. Figure 5.63 shows the comparison

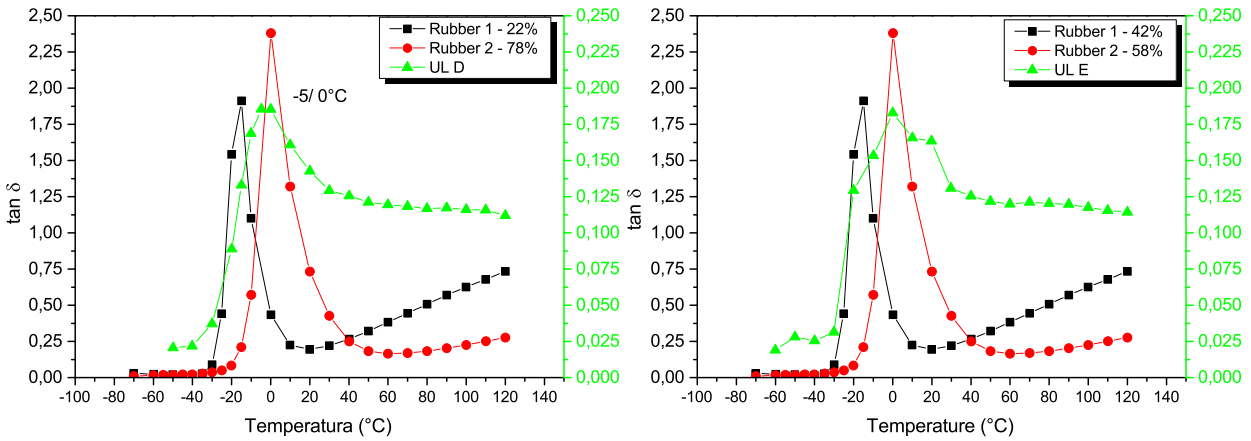

Figure 5.60: UL with blend of rubber 1 and 2, the percentages of rubbers inside the UL mix are different. The stress frequency is 10 Hz.

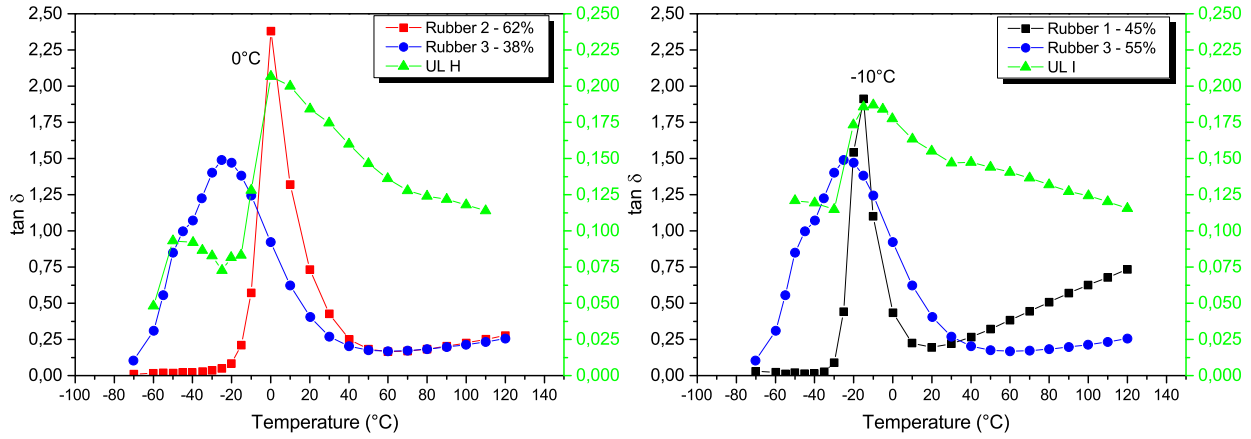

Figure 5.61: UL with blend of rubber 1 and 3 and rubber 2 and 3, the percentages of rubbers inside the UL mix are different. The stress frequency is 10 Hz.

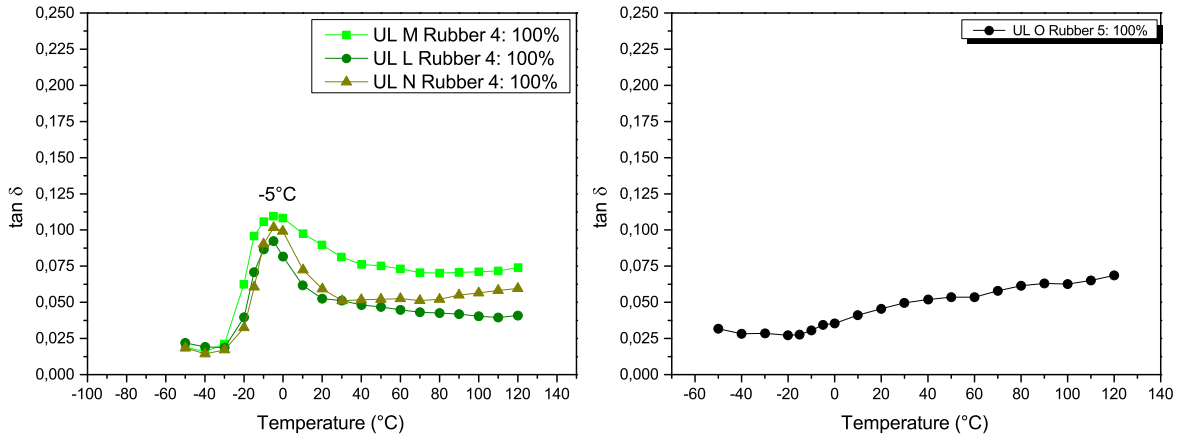

Figure 5.62: On the left: UL M, L and N have the same rubber composition. The temperatures of glass transition are the same. The stress frequency is 10 Hz. On the right: UL O, the tan δ is low. The stress frequency is 10 Hz.

between the elastic modulus of friction material and UL. The elastic modulus of friction material is flat, this is a good behavior because its main task is to have constant coefficient of friction in a wide range. The damping property of friction material is constant, so, it does not influence the Cold Noise phenomenon (Fig. 5.63) because the damping is low if there is no glass transition.

5.11.4 DMTA standard deviation

The standard deviation of the batch is evaluated by repeating the measurement 5 times on different samples (see Par. 5.10). The error is evaluated for the UL A, the stress frequency is 10Hz:

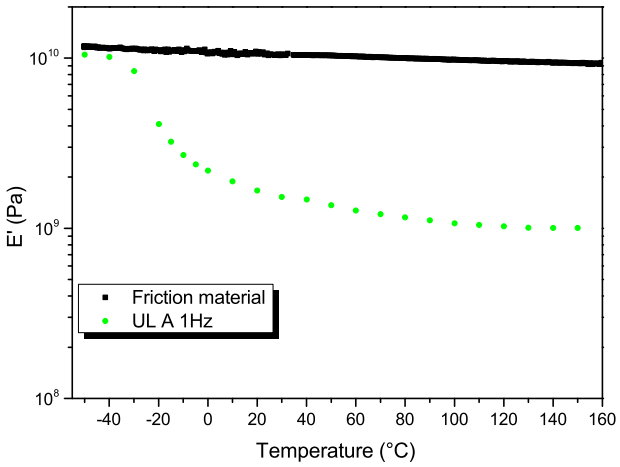

Figure 5.63: The figure shows the elastic modulus of friction material and UL. The stress frequency is 1 Hz.

T [°C]	$\overline{tan\,\delta}$	σ tan δ	T [°C]	$\overline{tan\,\delta}$	σ tan δ
-50	0.019	0.003	30	0.104	0.008
-40	0.022	0.001	40	0.104	0.007
-30	0.043	0.005	50	0.10	0.01
-20	0.16	0.02	60	0.110	0.008
-15	0.18	0.02	70	0.108	0.007
-10	0.17	0.01	80	0.108	0.008
-5	0.15	0.01	90	0.109	0.009
0	0.14	0.01	100	0.109	0.009
10	0.114	0.009	110	0.10	0.01
20	0.105	0.009	120	0.10	0.02

Table 5.9: Mean and standard deviation of tan δ. The stress frequency is 10 Hz.

Table 5.9 shows the average value and relevant uncertainty for UL A, measured with a stress frequency of 10 Hz. It is worth noticing that the relative uncertainty is about 10 % for T>-30 °C, corresponding to the glass transition temperature. Figure 5.64 shows the 5 repetitions of UL A.

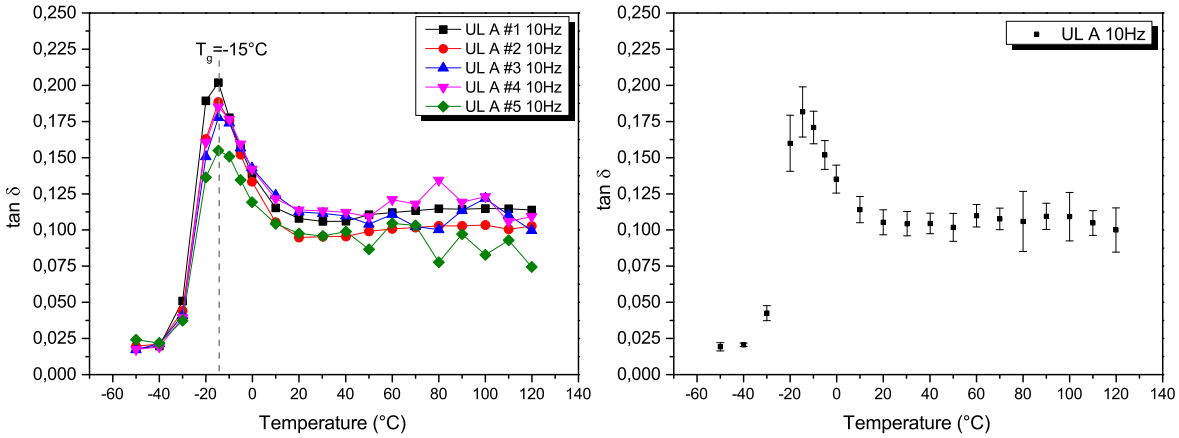

Figure 5.64: On the left: Five repetitions of DMTA test. The samples come from the same batch. On the right: Average and standard deviation of damping curve.

5.12 DMTA data analysis and WLF extrapolation

The WLF mathematical method allows to calculate the frequency response of the material for a reference temperature (Par. 4.9.2). This analysis is done for UL and rubber.

5.12.1 WLF extrapolation of rubber

A programme has been developed (Python language) in order to calculate the shift factor (Eq. 4.26). All the isotherms have been fitted with a third degree polynomial function. One reference isotherm is chosen, then the shift factor for adjacent isotherms is calculated (the software find the overlap windows). All of isotherms are shifted starting from the reference one. The master curve is obtained for a reference temperature and a seven order polynomial fit is calculated (only for highlight the trend of experimental data). This procedure is done for the elastic and viscous modulus, the master curve for the damping is given by the ratio between E"(T_{ref},ω) and E'(T_{ref},ω).

The peak of damping curve as a function of stress frequency is the glass transition, considering T=0 °C, it is possible to calculate at which frequency the material has the glass transition. The three rubbers have significant difference. Figure 5.65 shows the damping frequency response function at 0 °C and 25 °C.

The frequency of the glass transition increases if the temperature rises. If the thermal energy is higher, to have a glassy state in the polymer, it must be solicited at a higher frequency, such that the relaxation time is not sufficient to obtain a viscous behavior [28].

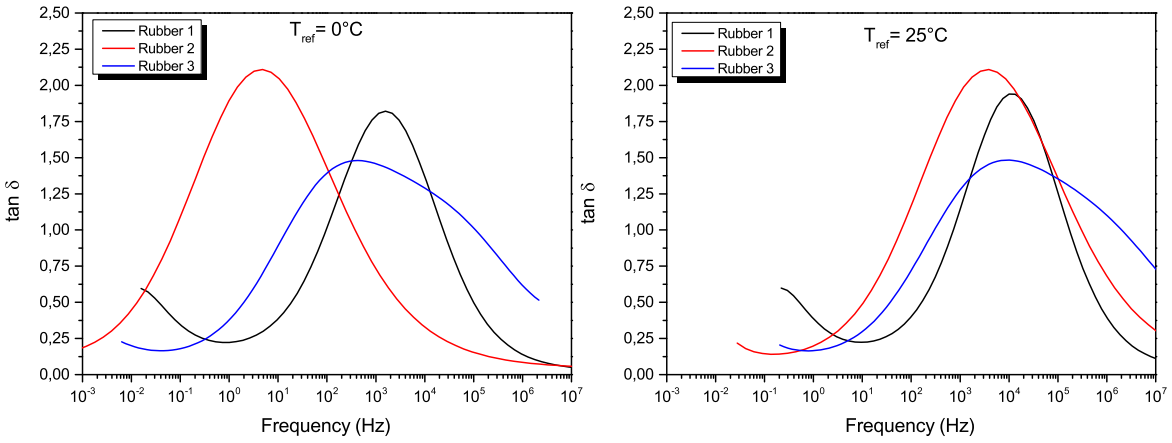

Figure 5.65: On the left: Damping frequency response function at 0 °C. On the right: Damping frequency response function at 25 °C.

Sample	C_1 -	C_2 [K]
Rubber 1	3.3	50.3
Rubber 2	9.3	65.4
Rubber 3	7.3	130.6

Table 5.10: Characteristic constants at 0 °C. In literature these values are in kelvin.

By evaluating the shift factor a_T, the characteristic constants C_1 and C_2 are calculated (Eq. 3.27), which depend on the free volume and the thermal expansion coefficient (Table 5.10).

5.12.2 WLF extrapolation of underlayer

The underlayers are studied according to their raw materials, as was done for a single frequency (10 Hz) and a wide range of temperatures (Par. 5.11.2), now a single temperature is studied in a wide range of frequency.
Extrapolation at high and low frequencies is performed by selecting the isotherms and which frequencies to consider. For the stress frequencies above 45 Hz, there is a resonance effect of the sample due to the three-point bending geometry. These frequencies are excluded in the analysis.

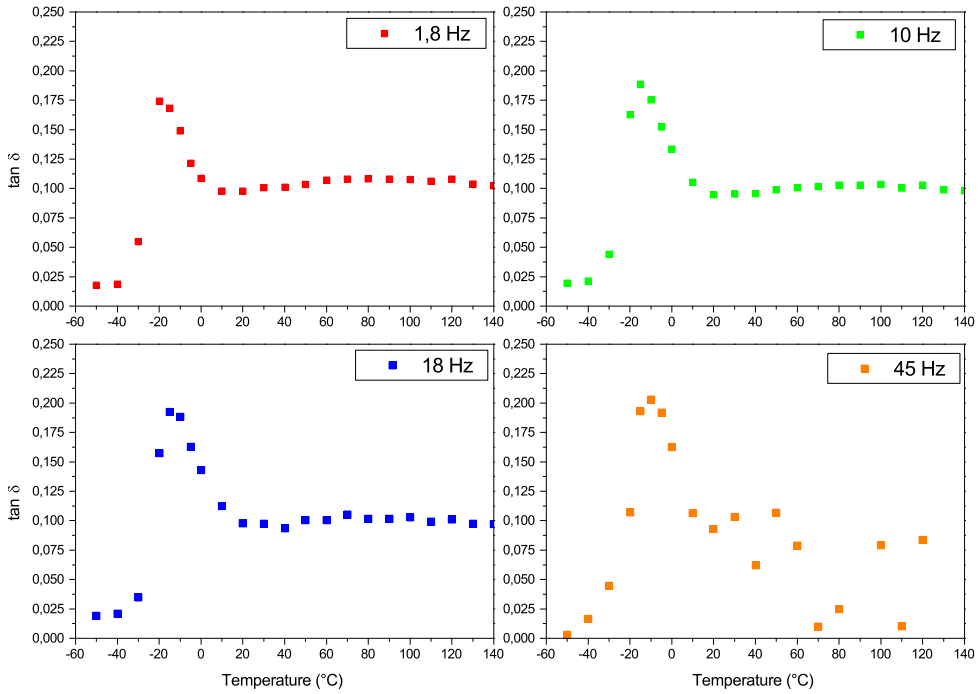

Figure 5.66: Damping as a function of temperature for different stress frequencies, above 45 Hz there is a resonance effect and the measurement is noisy.

Qualitatively it is observed that the glass transition of the underlayer is strongly influenced by rubber composition.

The underlayers have the same glass transition of the rubbers inside them. By changing the rubber composition the damping response of the underlayer changes. The y axes for UL and rubber are different. The UL has lower damping value because the other raw materials in the mix (Fig. 5.67).

Figure 5.68 shows how the percentage of rubber affects the frequency response spectrum. Again, the rubber with the glass transition at higher temperature has a greater influence on the transition of the underlayer, in terms of frequency (at fixed temperature), rubber that has the glass transition at the lowest frequency is the one that has the greatest influence (see Par. 3.2.4).

The underlayer H, despite having rubber 3, does not have any transition linked to this rubber (Fig. 5.69), this is due to the low amount of rubber 3 with respect to rubber 2. By varying the percentages and replacing the rubber 2 with the rubber 1, for UL I

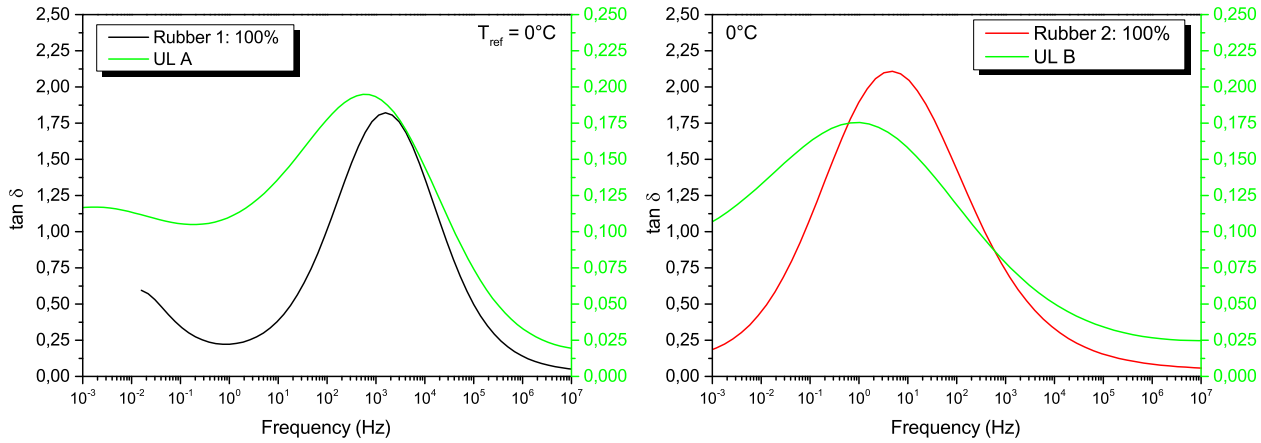

Figure 5.67: On the left: Damping frequency response at 0 °C for UL A and rubber 1. Frequecy (5 points): 1.8-3.2-5.8-10.5-18.9 Hz, Temperature (17 points): from -40 to 100 °C. On the right: Damping frequency response at 0 °C for UL B and rubber 2. Frequecy (6 points): 1.8-3.2-5.8-10.5-18.9-23 Hz, Temperature (17 points): from -40 to 100 °C.

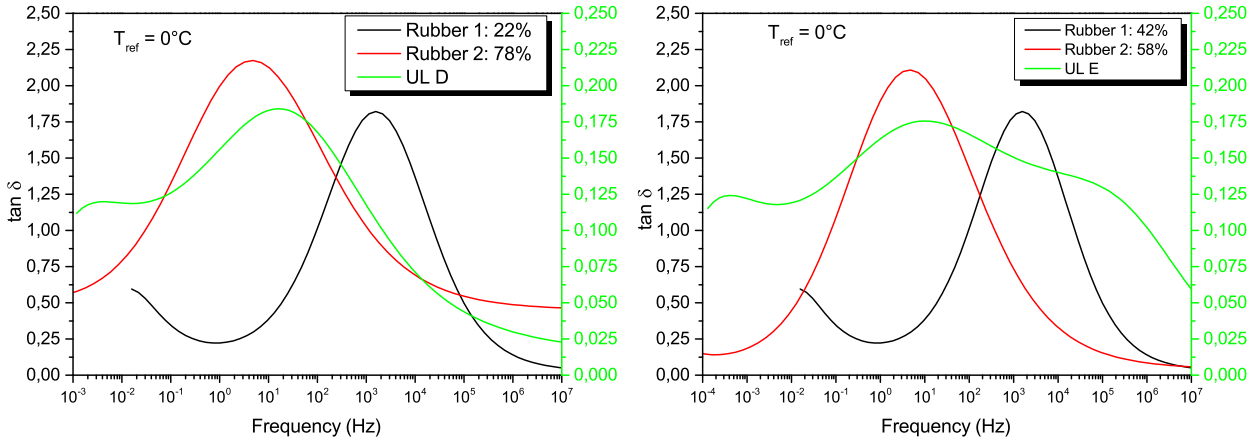

Figure 5.68: On the left: Damping frequency response at 0 °C for UL D and rubber 1 and 2. Frequecy (6 points): 1.8-3.2-5.8-10.5-18.9-23 Hz, Temperature (17 points): from -40 to 100 °C. On the right: Damping frequency response at 0 °C for UL E and rubber 1 and 2. Frequecy (5 points): 3.2-5.8-10.5-18.9-23 Hz, Temperature (17 points): from -40 to 100 °C.

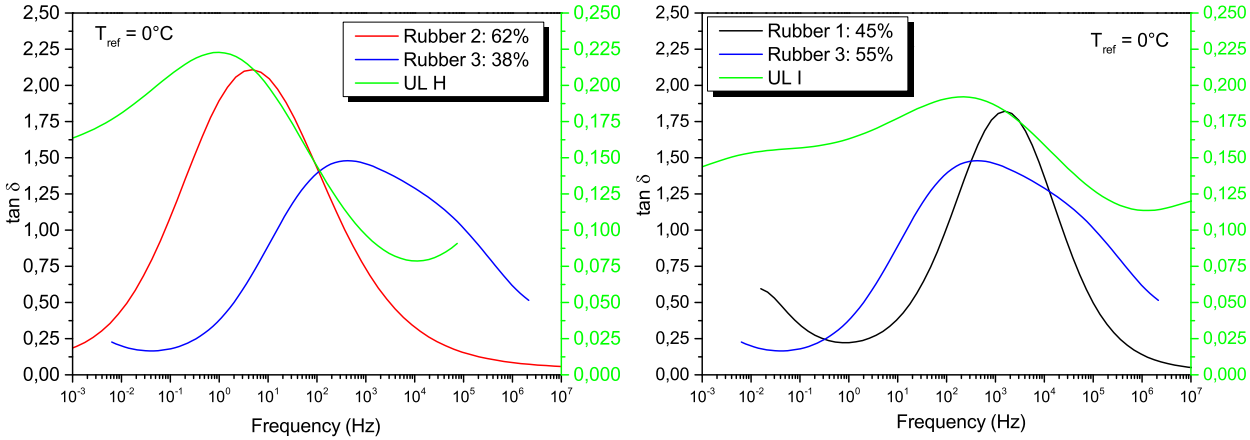

Figure 5.69: On the left: Damping frequency response at 0 °C for UL H and rubber 2 and 3. Frequecy (5 points): 1.8-3.2-5.8-10.5-18.9 Hz, Temperature (17 points): from -40 to 100 °C. On the right: Damping frequency response at 0 °C for UL I and rubber 1 and 3. Frequecy (4 points): 5.8-10.5-18.9-23 Hz, Temperature (17 points): from -40 to 100 °C.

the damping value is obtained around the frequencies at which the glass transition of the rubber occurs.

The underlayers with rubber 4 are all characterized by low damping values (Fig. 5.70).

Underlayer O does not have a glass transition (see Fig. 5.62), therefore it is not possible to extrapolate its frequency behavior, as the time-temperature superposition principle does not apply.

The first important result is that rubber 2 is worse than rubber 1. At 0 °C the damping of rubber 1 is greater than rubber 2 in the acoustic frequency range (9 and 12 kHz). Quantitatively the difference between the rubbers is the same between the underlayers (Fig. 5.71).

The figure 5.72 shows all the significant underlayer at the reference temperature of 0 and 25 °C. UL A, E and I have the highest damping values in the acoustic range. UL A is composed by rubber 1, UL E is composed by rubber 1 and 2, and UL E is composed by rubber 1 and 3.

The phenomenon of Cold noise could be due to the rubber inside the underlayer (further experimental results are showed in the paragraph 5.14.2). Figure 5.72 shows that as the temperature increases, for the frequencies considered (9 and 12 kHz), the damping increases; obviously in a different way depending on the material. For example,

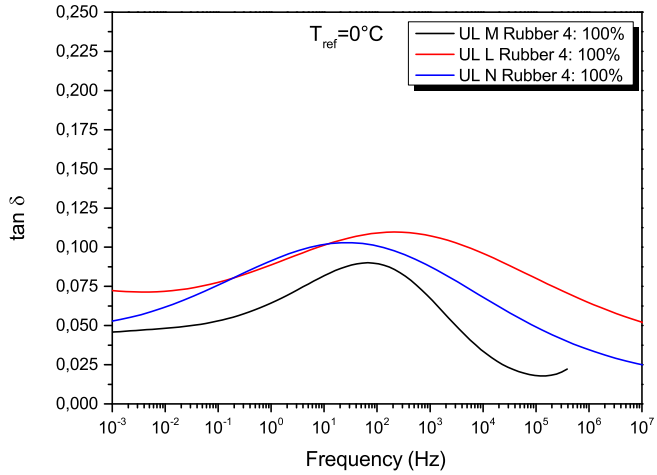

Figure 5.70: Damping frequency response at 0 °C for UL M, N, L and rubber 4. Frequecy (5 points): 1.8-3.2-5.8-10.5-18.9 Hz, Temperature (17 points): from -40 to 100 °C.

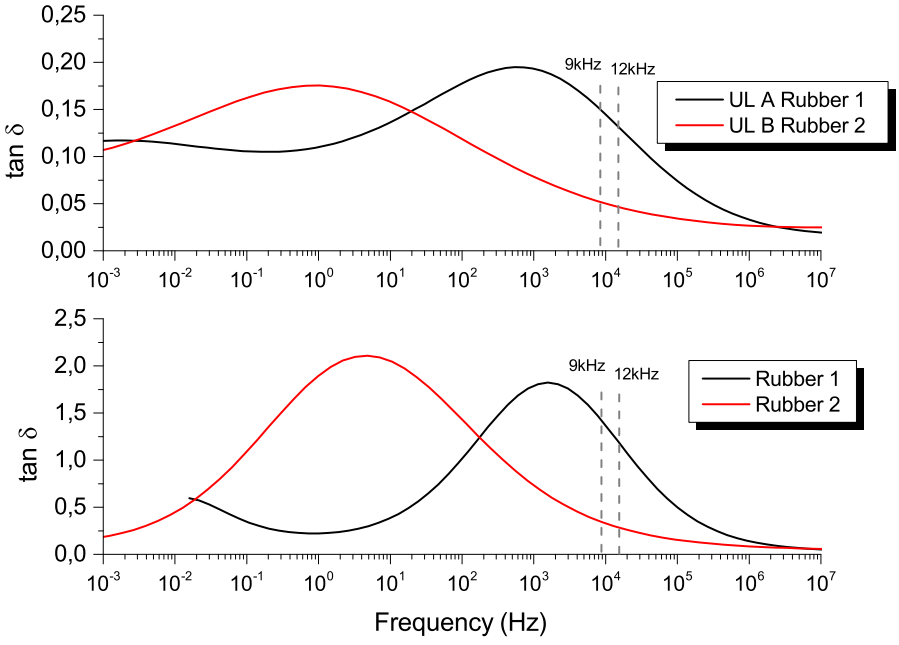

Figure 5.71: Damping response function. On the top there are the UL A and B, on the bottom the rubbers.

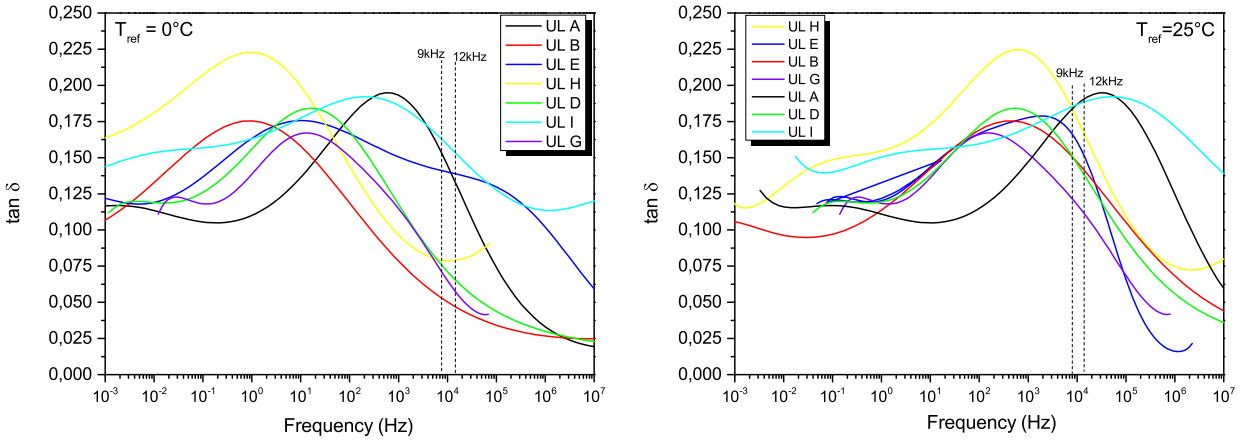

Figure 5.72: Damping response function of all the UL. On the left: Reference temperature 0 °C. On the right: Reference temperature 25 °C.

the UL H at 25 and 0 °C has big difference in the damping properties (Fig. 5.73). This huge visco-elastic difference of the material could be one of the causes of the generation of the noisy phenomenon.

5.12.3 WLF standard deviation

The measurement was repeated five times on different samples of the batch of the UL A (Fig. 5.74). From the five curves obtained of tan δ (ω) the value of the maximum was calculated by performing a second degree regression (around the peak) and equaling the first derivative to zero.

The average values of the damping peaks are:

$\overline{\omega}$ Hz	$\overline{tan\,\delta}$
$(6 \pm 1) \cdot 10^2$	0.19 ± 0.02

Table 5.11: Mean value of damping and frequency peak.

5.12.4 Damping map

The damping map of UL and rubber can be obtained from the WLF theory and DMTA data. The procedure explained in the Par. 4.9.2 (translate all the isotherms with respect

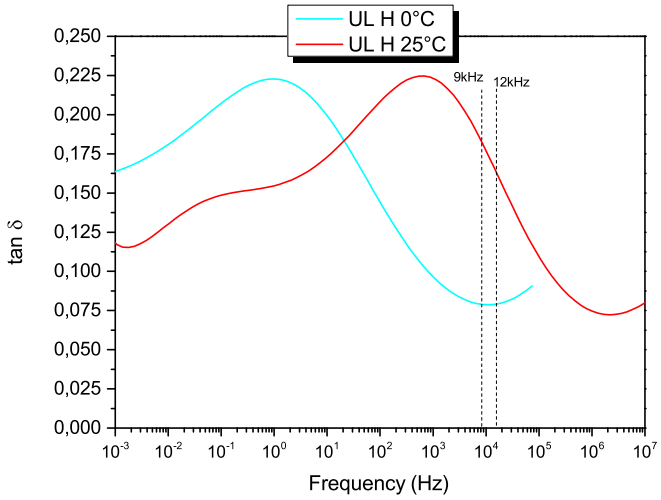

Figure 5.73: Damping response function of the UL H at two different reference temperature.

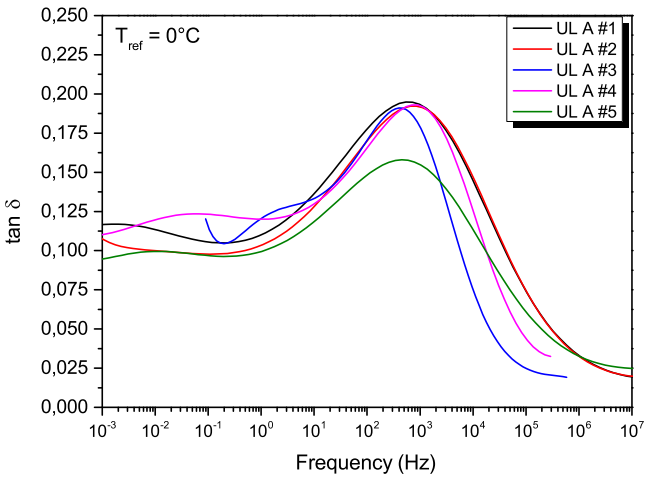

Figure 5.74: Measure repetition on UL A. Reference temperature: 0 °C.

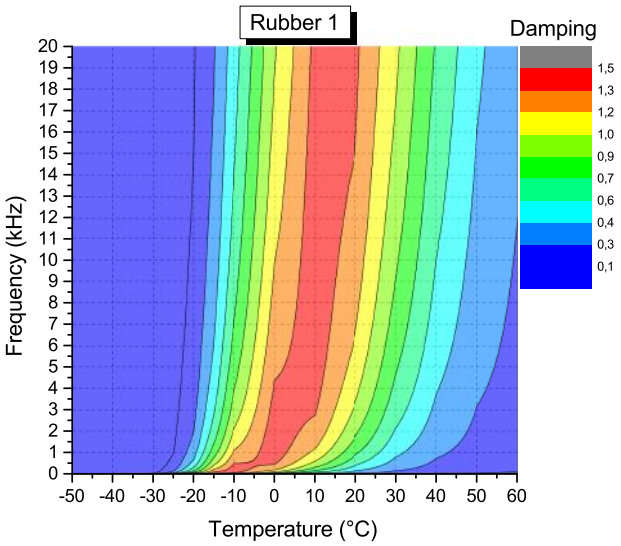

Figure 5.75: Damping map of rubber 1, temperature range: -50 to 60 °C, stress frequency range: 0 to 20 kHz.

to the reference one), it can be repeated by changing the reference isotherm. Then by selecting the acoustic range (between 1 and 20 kHz) the damping map is obtained.

The figures 5.75 and 5.76 show a damping map of a rubber and underlayer E, no other data are shown because they are sensitive data for the company. Rubber 1 has high damping value in the acoustic range between -10 and 20 °C. UL E has high damping values over 20 °C, hence this is a bad UL for Cold noise, but it can be useful to damp a warm noise issue. Thanks to the damping maps it is possible to engineer the formula of underlayer and have the best material to solve a specific noise problem (specific frequency and temperature range).

5.13 Frequency response function of brake pad

This analysis is done on a brake pad, composed of friction material, underlayer and metal back plate. All the brake pads have the same friction material but different underlayer. The brake pad is placed in the freezer for more than 12 hours at a temperature of -31 °C; the measurement is performed for temperatures of -20 / -15 / -10 / -5 / 0 and 25 ° C, the temperature is measured by the infrared thermometer on the metal back plate. The pad has a good thermal capacity, it takes thirty minutes from -20 to 0 °C. The brake pad is placed on the sponge, which isolates it from external vibrations.

The frequencies of the spectrum are similar to those of the dyno, there are two

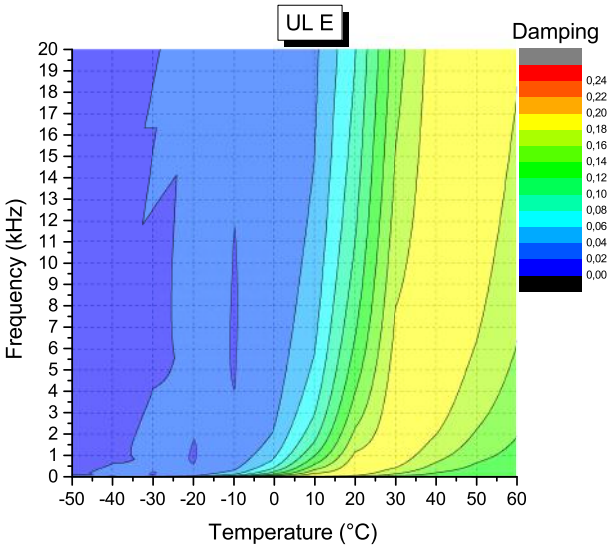

Figure 5.76: Damping map of UL E, temperature range: -50 to 60 °C, stress frequency range: 0 to 20 kHz.

resonant frequencies at about 9 and 12 kHz:

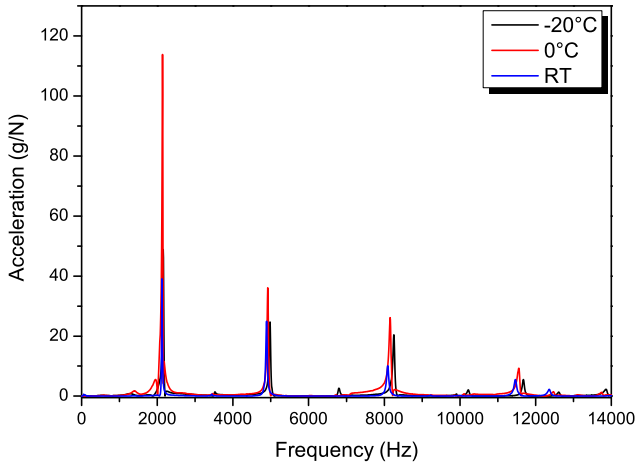

Figure 5.77: Frequency response function at -20, 0 and 25 °C.

The frequencies of about 2 and 5 kHz are related to the mass and geometry of the pad, therefore they have negligible influence on the temperature variation (Fig. 5.77).

For example, the underlayer E for the frequency of 2 kHz has a temperature shift of the peak (from -20 to 25 °C) of about 140 Hz, while for the frequency of 9 kHz, it has a shift of the resonance frequency peak over 800 Hz (Figure 5.78). High frequencies are strongly influenced by temperature, for example the frequency of 12 kHz tends to disappear at room temperature. The frequencies of 9 and 12 kHz were analyzed at different temperatures, evaluating the peak value and the resulting damping (Eq. 4.30). The first measure was done on the friction material without underlayer, this is to evaluate the contribution of the friction material. By evaluating the frequency of about 9 kHz, it is obtained that the pad without underlayer shows a negligible variation as a function of temperature (Figure 5.79). This result indicates that the greatest contribution to the damping of vibrations in the pad is due to the underlayer; moreover, the friction material has negligible variation in the temperature range analyzed.

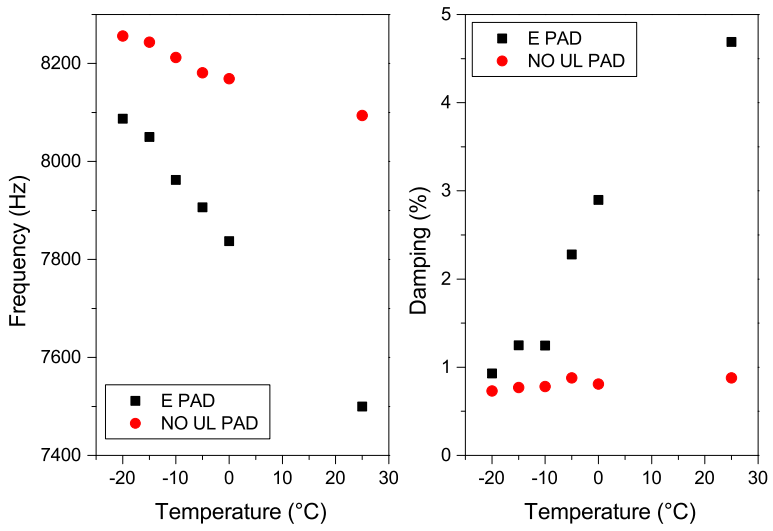

Figure 5.78: On the left, the graph shows the frequency response function of brake pad. On the right, the damping of the frequency.

The same trend has the frequency around 12 kHz.

5.13.1 Frequency analysis of 9 kHz

Different underlayers inside the brake pads show different damping properties.

The materials containing rubber 1 and 2 qualitatively have the same behavior as a function of temperature (see Fig. 5.80).
The underlayers with the rubber 4 have a low damping value $\xi(T)$, this is in agreement with the DMTA data.

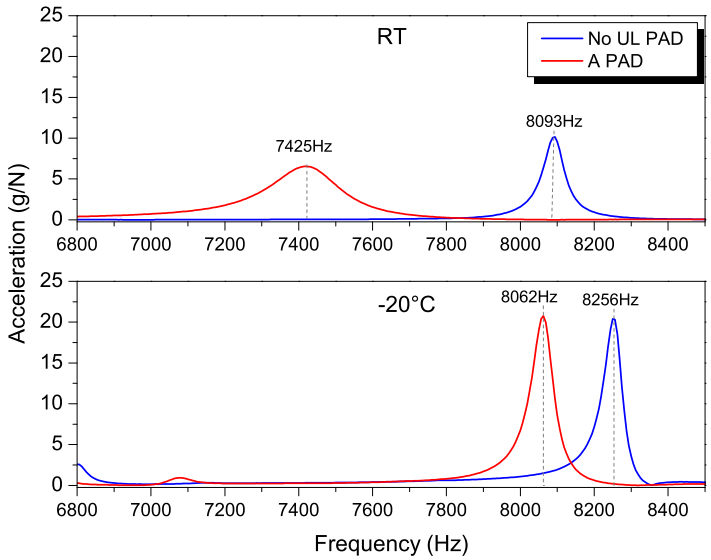

Figure 5.79: Frequency response function of A PAD and no UL PAD at -20 and 25 °C.

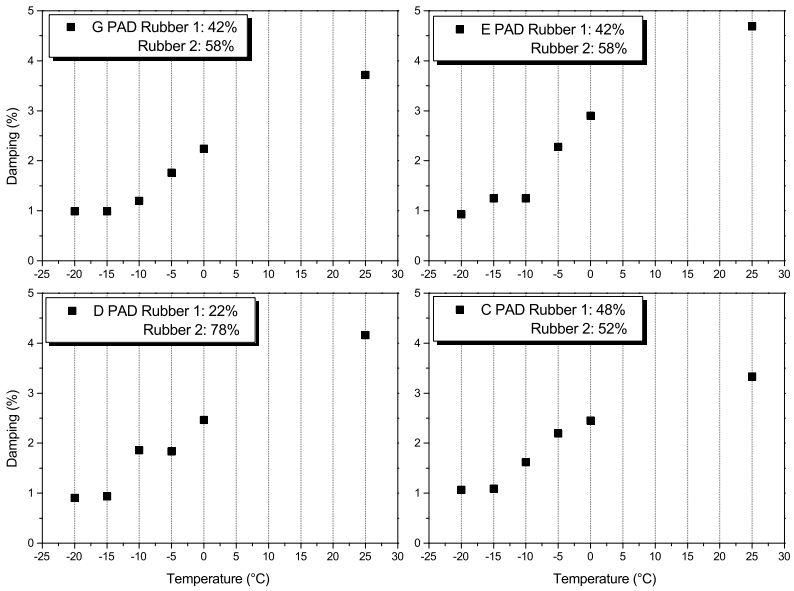

Figure 5.80: Damping as a function of temperature $\xi(T)$, UL composed by rubber 1 and 2. Frequency of 9 kHz.

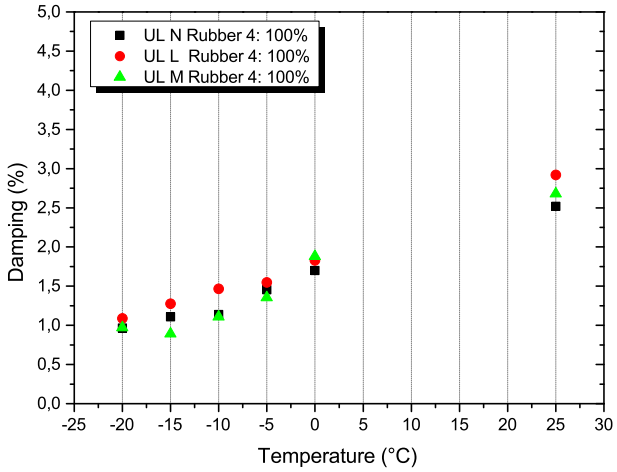

Figure 5.81: Damping as a function of temperature $\xi(T)$, UL composed by rubber 4. Frequency of 9 kHz.

The pads with underlayer A and B, containing respectively only rubber 1 and 2, show a different trend.

The $\xi(T)$ of A PAD increases from -15 °C, this is in agreement with the glass transition of rubber 1 (Fig. 5.57). Rubber 1 has a lower temperature transition and therefore higher damping properties at lower temperatures (Fig. 5.82).
The underlayers with rubber 3 show high damping values below 0 °C (Fig. 5.83); rubber 3 has a glass transition at very low temperature (Fig. 5.57), so it is a good rubber to damp the mechanical vibration in the cold range.
The rubber component in the underlayer, for low temperatures, is fundamental to understand the behavior of the geometry resonance frequency of the brake pad.

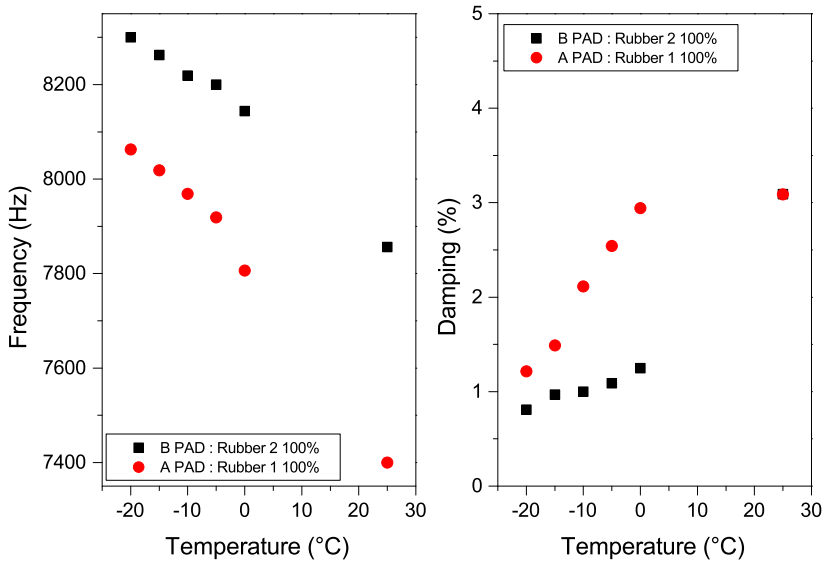

Figure 5.82: Damping as a function of temperature $\xi(T)$. The underlayers have different rubber.

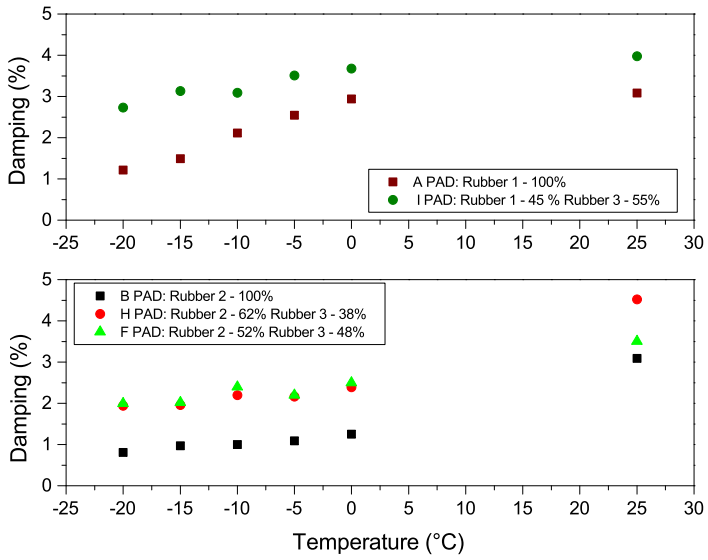

Figure 5.83: Damping as a function of temperature $\xi(T)$. ULs composed by rubber 3 show higher damping values.

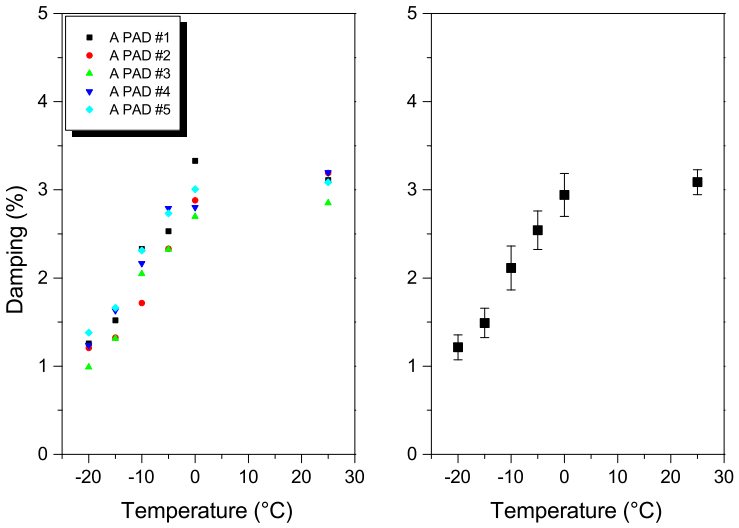

Figure 5.84: Damping as a function of temperature $\xi(T)$ of the repetitions of A PAD.

5.13.2 Standard deviation of 9 kHz

The dispersion on the batch was calculated on five underlayer A pads (Fig. 5.84). In all repetitions, the damping $\xi(T)$ increases as a function of the temperature (from -20 to 25 °C).

Temperature (°C)	$\overline{\xi}$	σ
-20	1.2	0.1
-15	1.5	0.2
-10	2.12	0.25
-5	2.5	0.2
0	2.9	0.2
25	3.09	0.14

Table 5.12: Average and standard deviation of damping.

Therefore the dispersion of the geometric resonance frequencies:

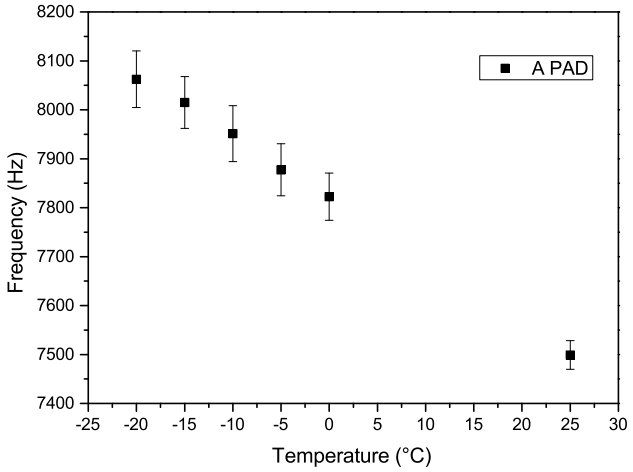

Figure 5.85: Frequency in function of temperature (A PAD).

the frequency decreases if the temperature increases (Fig. 5.85).

Temperature [°C]	$\overline{\nu}$ [kHz]	σ [kHz]
-20	8.06	0.06
-15	8.02	0.05
-10	7.95	0.06
-5	7.88	0.05
0	7.82	0.05
25	7.50	0.03

Table 5.13: Average of frequency ($\overline{\nu}$) and standard deviation.

5.13.3 Frequency analysis of 12 kHz

The frequency of 12 kHz shows qualitatively the same results of the analysis of 9 kHz. Only two examples of underlayer A (Fig. 5.86) and B follow (Fig. 5.87):

The standard deviation of A PAD of damping is:

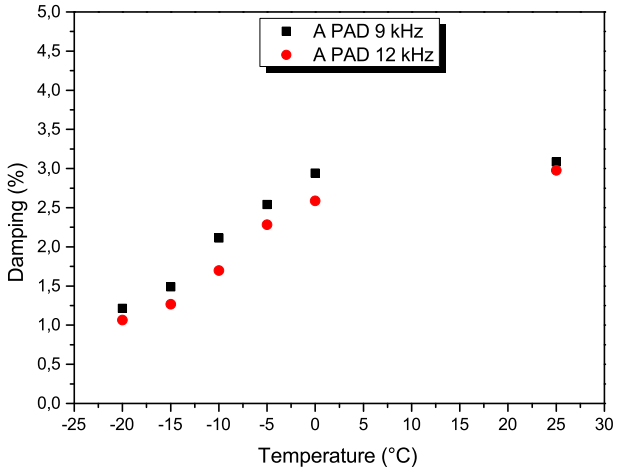

Figure 5.86: Damping of 9 and 12 kHz of A PAD.

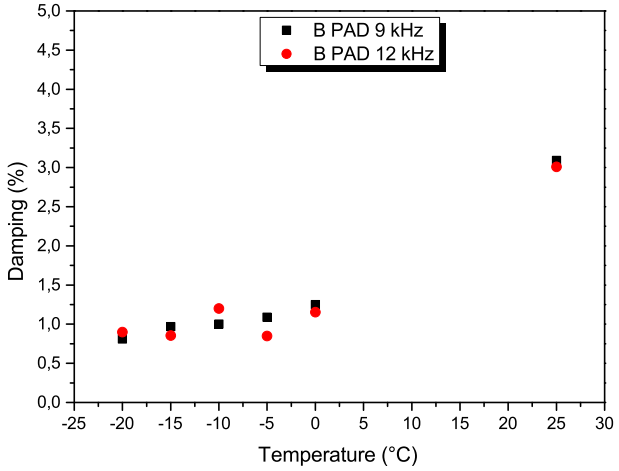

Figure 5.87: Damping of 9 and 12 kHz of B PAD.

Temperature (°C)	$\overline{\xi}$	σ
-20	1.06	0.09
-15	1.3	0.2
-10	1.7	0.3
-5	2.3	0.2
0	2.6	0.2
25	3.0	0.2

Table 5.14: Average and standard deviation of damping. Frequency: 12 kHz.

These values are comparable with 9 kHz analysis. The frequencies of 9 and 12 kHz are very close, the polymer damping response is very similar in this range. FRF results are in agreement with the DMTA results. The damping response changes significantly if the stress frequency changes order of magnitude.

5.14 Dyno test Cold Noise

The first dyno test was done on a friction material without underlayer, this is to evaluate what is the effect of underlayer on mechanical and acoustic vibrations. The procedure performed on this brake pad is the second (temperature chamber constant at -15 °C and high pressure brakes, see Par. 4.11). Considering the frequencies of 9 and 12 kHz, for amplitudes greater than 70 dB, this material does not show significant variations for the temperatures considered (Fig. 5.88). This result is in agreement with the FRF and DMA tests on friction material without underlayer. Amplitude of the braking noise is constant as a function of temperature.

The Fig. 5.89 shows the effect of underlayer on the amplitude of braking noise. Underlayer mechanically filters frequencies (Fig. 5.93). The UL attenuates the frequencies of 9 and 12 kHz after a specific temperature, so the rubber begins to have its damping properties, while in cold conditions, the UL is rigid below the glass transition. By increasing the temperature, a decrease in noise intensity is qualitatively observed until it disappears (G PAD).

5.14.1 Comparison between Cold Noise procedure

The two procedures are different, the first has less pressure braking, therefore the temperature of the rotor and pad during the test is lower than in procedure two. Procedure one amplifies the Cold Noise, while the second one provides general brake pad behavior. Obviously, the goal is to eliminate the two frequencies of 9 and 12 kHz in the cold range, maintaining a good behavior of the material in the warm and hot range.

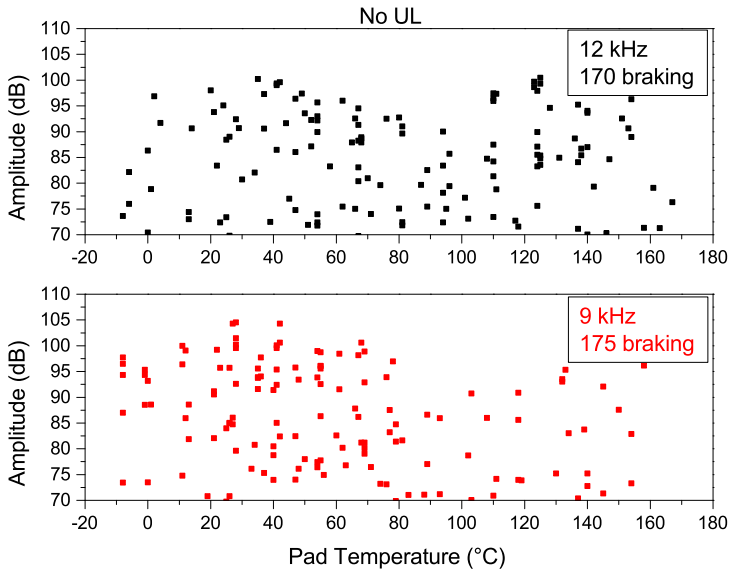

Figure 5.88: Amplitude of the braking noise of the two characteristic frequencies of 9 and 12 kHz as a function of temperature; brake pad without underlayer. Procedure two.

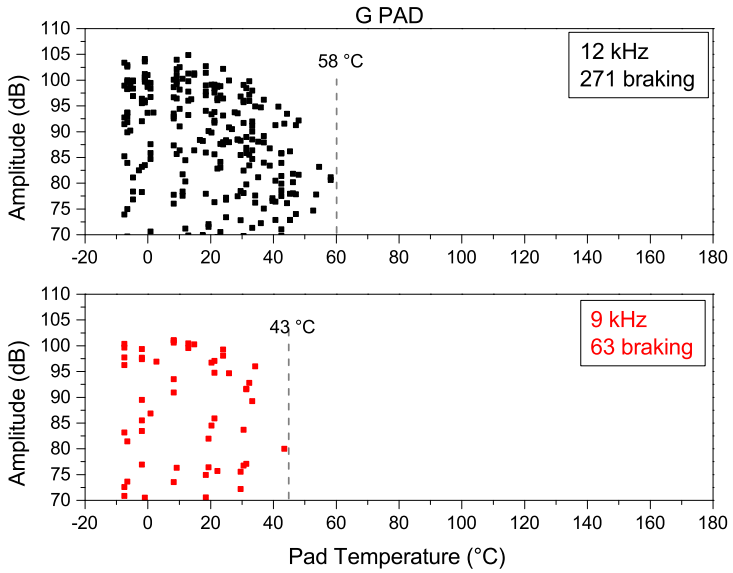

Figure 5.89: Amplitude of the braking noise of the two characteristic frequencies of 9 and 12 kHz as a function of temperature; brake pad with underlayer G. Procedure two.

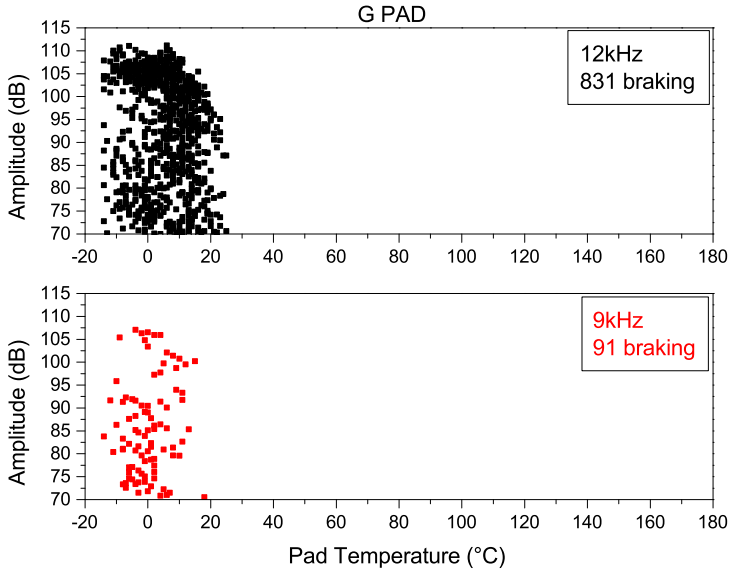

Figure 5.90: Amplitude of the braking noise of the two characteristic frequencies of 9 and 12 kHz as a function of temperature; brake pad with underlayer G. Procedure one.

With procedure one, the number of noisy braking increases for the pad with UL G (Fig. 5.90) up to 49.8%. Procedure one highlights a curious result on the material without UL. The frequency of 12 kHz appears in the temperature range between 10 and 40 °C for the material without UL (Figure 5.91), this indicates that the material without UL has greater damping properties than the UL G for low temperatures (below 10 °C). The average temperature of noisy braking of 9 kHz for the G PAD is $\overline{T}_{9-GPAD}$ ∼0.7 °C and for the pad without UL $\overline{T}_{9-NoULPAD}$ ∼12 °C (not considering temperatures above 60 °C which are not of interest for the cold study); therefore the stiffening of the UL at low temperatures has lower damping properties than the friction material. These results highlight how fundamental the underlayer is for the vibrational properties of the brake system.
It should be noted that the underlayer is a component that cannot be eliminated in the brake pad, in the warm and hot range, the pad without UL has a very bad frequency spectrum.

5.14.2 Dyno test underlayer comparison

From the FRF results (Par. 5.13.1) and WLF theory (Par. 5.12), it was chosen to test the pads with commercial UL A, B, I and G and a new UL called UL Z, it was developed with a new low glass transition rubber (Fig. 5.95). The formulation of this UL is protected by a patent [68], because this rubber solves the Cold Noise. The materials were tested

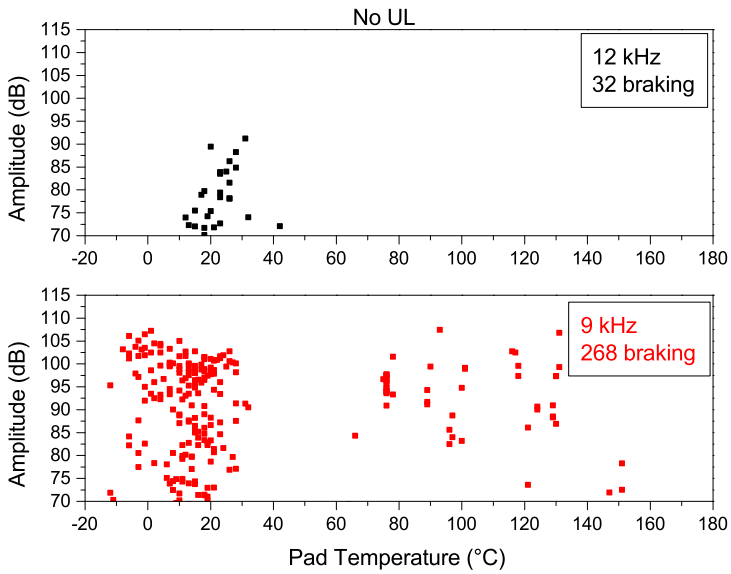

Figure 5.91: Amplitude of the braking noise of the two characteristic frequencies of 9 and 12 kHz as a function of temperature; brake pad without underlayer. Procedure one.

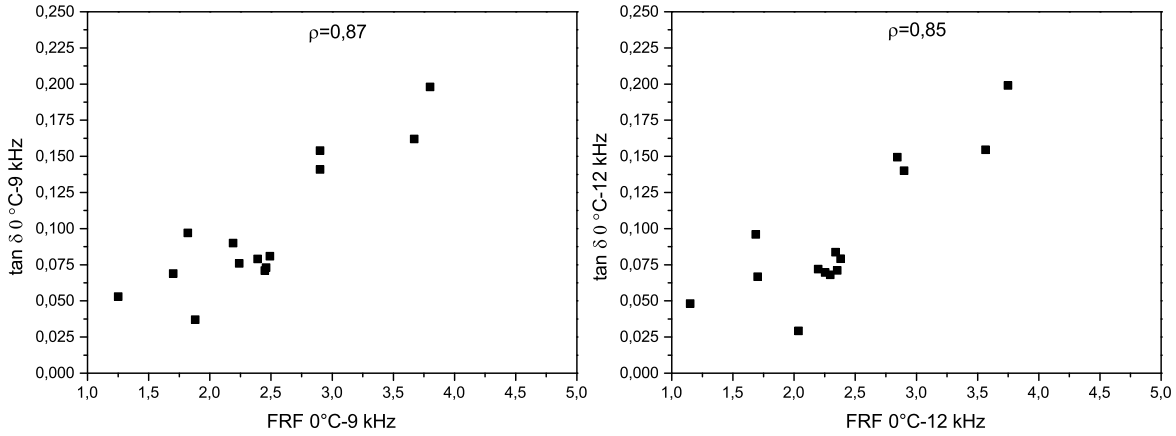

Figure 5.92: Correlation between FRF and WLF results. The figures show the Pearson correlation index (ρ).

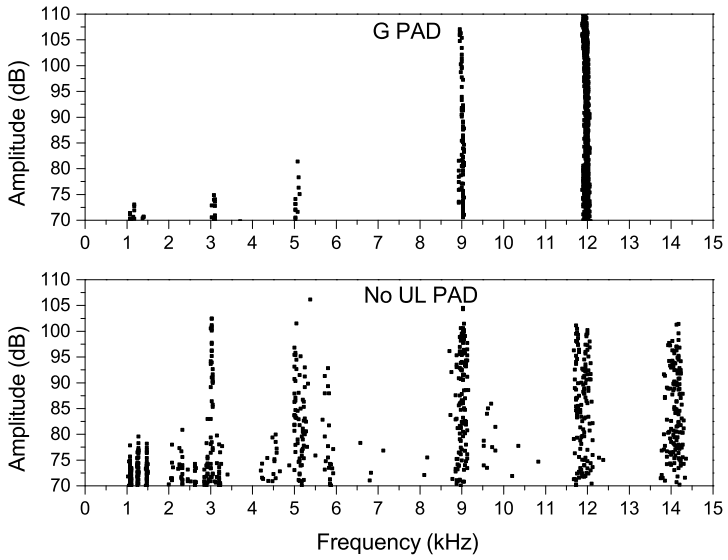

Figure 5.93: Frequency spectrum of dyno test (procedure two). The brake pad without underlayer has many critical frequencies. Each point is a noisy braking.

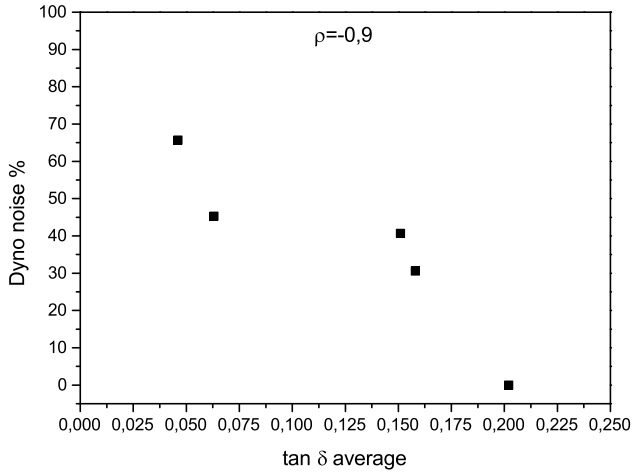

Figure 5.94: Correlation between dyno test and WLF results. The average value of tanδ between 9 and 12 kHz was taken.

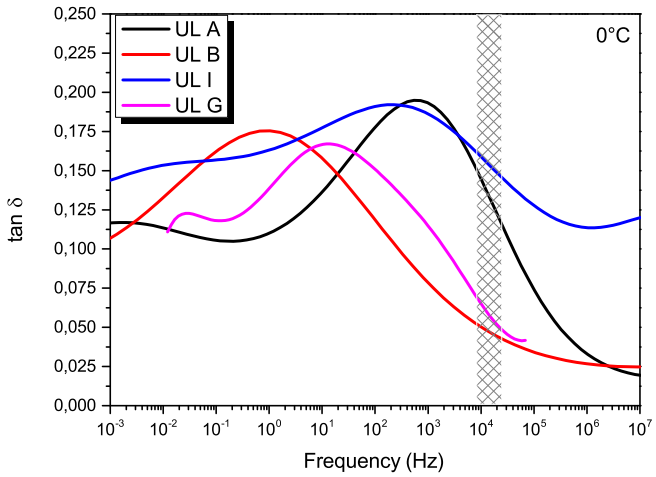

Figure 5.95: Damping response function at 0 °C. UL tested on dyno. Gray grid highlight the frequency range of interest.

with procedure one. The reference material is the UL G, the selected underlayers are able to prove the proposed damping model. UL B is the worst underlayer for Cold Noise, UL A (Fig. 5.96) and I show an improvement respect to the reference one (UL G) and UL Z solves the Cold Noise (Fig. 5.97). These results are in agreement with the FRF and DMTA (Fig. 5.92). The damping model and the procedure created to characterize the materials have good results. The material without underlayer has good damping in the cold range, but in the warm and hot regime is rich of noisy braking. Considering the mean value of damping frequency response between 9 and 12 kHz, the correlation between dyno test and DMTA is good (Fig. 5.94).

	B PAD %	G PAD %	A PAD %	I PAD %	NO UL PAD %	Z PAD %
braking noisy	65.7	45.3	40.7	30.6	14.7	0

Table 5.15: Percentage of noisy braking considering the frequencies of 9 and 12 kHz, total of 2034 braking.

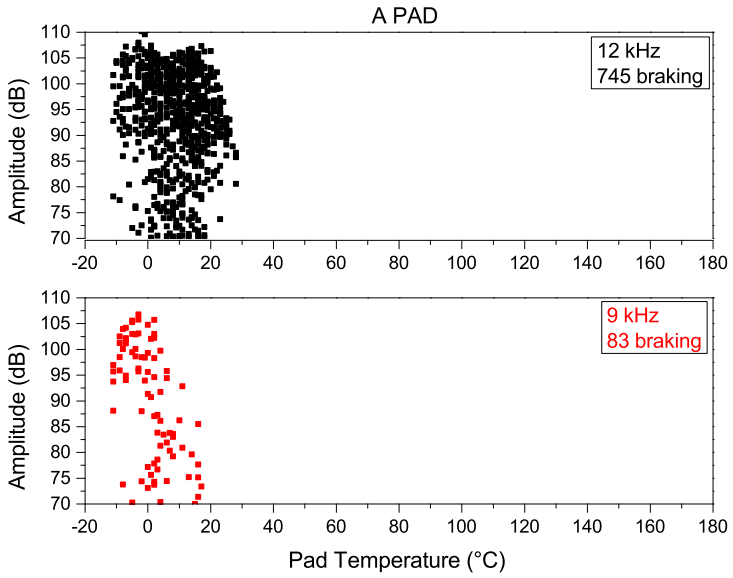

Figure 5.96: Amplitude of the braking noise of the two characteristic frequencies of 9 and 12 kHz as a function of temperature; brake pad with UL A. Procedure one.

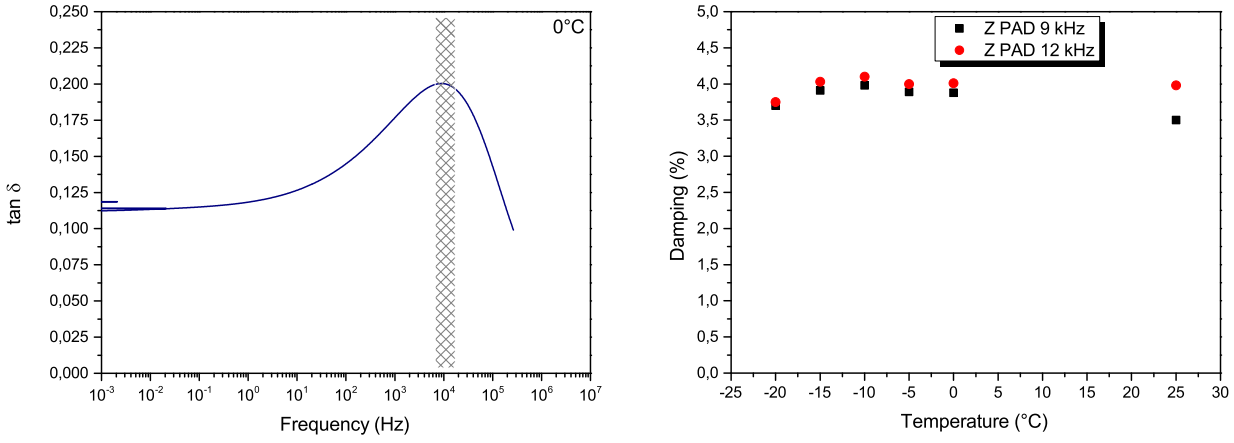

Figure 5.97: Damping properties of UL Z. It has excellent damping in the cold range.

Chapter 6

Conclusions

6.1 Conclusions and outlook

The study of the generation and propagation of the mechanical vibration generated by the brake pad has had good results, which will be useful for the company to develop the materials of the future. In the near future, the production of electric cars will increase and therefore the threshold of acceptability of the noise of the brake system will decrease. Regarding the noise generation, the results of the *Stick-Slip* Low Steel tests show a correlation between the tribometer, the vehicle and the dynamometer results (Par. 5.6.7). This means that the friction materials study in laboratory, for specific problem, can be a valid instrument for the tribological characterization. The study of friction materials on tribometer does not pretend to substitute the study on vehicle or on dyno. However, the decreasing of time, energy and economic cost allows to get more data, which makes it a good instrument both to make a preselection of the materials that then will be studied in other ways, and to help the formulation of new materials. As expected, a correlation between the humidity and the *Stick-Slip* phenomenon has been found (Par. 5.6.6). This can be explained with the increase of the static and dynamic CoF difference at high humidity, in particular with a greater increase of the static one.
Another result is the evidence of an effect of the height surface distribution, in particular linked to a moderate correlation between the Skewness and the Kurtosis with the *Stick-Slip* generation (Par. 5.6.4), even if, in many cases, the chemistry changes because of a surface modification and it is difficult to understand how the variables interact. Another information that comes out from the surface analysis is the importance of an uniform distribution of raw materials on the surface, specially the lubricant and the abrasive, in order to reduce the *Stick-Slip* phenomenon (Par. 5.6.4). This happens because in this case the CoF has a more uniform distribution. From the SEM analysis the materials that produce less *Stick-Slip* are the ones that present a minor surface dispersion of raw materials. Many small contact points have a lower propensity to *Stick-Slip*.

The FIB inspections showed how primary and secondary plateuax and debris are made (Par. 5.6.5); the differences between these areas are very significant, both in terms of morphology and chemistry.
The *Stick-Slip* test for NAO materials on tribometer shows a correlation with the vehicle results (Par. 5.7.2). This is a very satisfying outcome because the NAO materials do not produce good results on the dynamometer in the *Stick-Slip* test, and the only possibility was to study then on the vehicle but it is not possible for all the materials.
Regarding the modification of the friction properties of polyethilene through surfac patterning, interesting results have been obtained. The dynamic friction coefficient decreases with respect to that of a non-patterned surface and the presence of surface cavities also affect the stick-slip behavior. Friction increases with humidity, and the onset of stick-slip events occur in the high humidity regime. The qualitative agreement between the experimental and numerical results indicate the robustness of the adopted simplified approach, which can be adopted in future to design more complex patterned surfaces with controlled, possibly anisotropic, friction properties. Using patterned surfaces can provide a means to modify the parameter ranges in which stick-slip takes place without changing the chemical composition of the surfaces, which can be useful in many applications, including groan and squeal noise reduction. Reducing the amplitude of stick-slip can also be useful to reduce the mechanical vibrations generated during friction.
Regarding the noise propagation, the characterization of underlayers and rubbers done with DMTA has shown a clear influence of rubber on the viscoelastic properties of the underlayer. This is an important result, which allows the identification of those features (e.g. rubber composition, percentage) of the underlayers, which effectively contribute to attenuate noise propagation (Par. 5.12.2).
The frequency response of the brake pad has shown how the friction material has a flat behavior as a function of temperature and how different underlayers modify the damping of the brake pad (Par. 5.13).
The results obtained with FRF and DMTA are in agreement (Par. 5.14.2). These results have enable to choose the underlayers to be tested on the dyno test in order to verify the developed laboratory protocols. The dyno tests confirmed flat behavior as function of temperature of the friction material.
The results of the dyno tests (the percentage of noisy braking) are in agreement with the damping obtained with the DMTA and FRF (Par. 5.14.2). High damping values mean low percentage of noisy braking in the temperature and frequency range under consideration. Topographical maps of the damping for each material can be obtained by the WLF theory (Par. 5.12.4); therefore, for each squeal problem it is possible to select the suitable material for a determined temperature and frequency range. Thanks to this protocol, a underlayer Z was created that solves the *Cold noise*. The details of this formula have been patented. This underlayer also gave excellent results on other critical projects for *Cold noise*.
With these techniques it is possible to implement new types of rubber, according to

other parameters (see appendix B). The formulation of the underlayers and the study of their behavior as a function of frequency and temperature is fundamental, since, once a mixture has been agreed with the customer, if noise problems occur, it is possible to do variations of the underlayer, without changing the formulations of the friction material. Therefore, the ability to drive the mechanical-acoustic frequencies of the brake pads by acting only on the underlayer formulation, offers excellent technical and commercial solution to reduce noise and to improve the comfort level in vehicles.

Appendix A

Surface parameters

A.1 Roughness

The surface parameters are defined using A as the whole surface, x and y as the width and the length coordinates and z as the height coordinate. z_{mean} is the height mean value. Roughness (Sq) is defined as:

$$Sq = \sqrt{\frac{\int\int_A (z(x,y) - z_{mean})^2 dxdy}{A}} \tag{A.1}$$

it is the standard deviation of the surface z values.

Arithmetical mean height (Sa) is define as:

$$Sa = \frac{1}{A} \int\int_A |z(x,y)| dxdy \tag{A.2}$$

Sa is the extension of Ra to a surface. It expresses, as an absolute value, the difference in height of each point compared to the arithmetical mean of the surface. Sa is used to evaluate surface roughness.
Skewness (Ssk) is defined as:

$$Ssk = \frac{1}{Sq^3} \left[\frac{\int\int_A (z(x,y) - z_{mean})^3 dxdy}{A} \right] \tag{A.3}$$

it is the third statistical moment of the z distribution and it represents its symmetry.

Kurtosis (Sku) is defined as:

$$Sku = \frac{1}{Sq^4} \left[\frac{\int\int_A (z(x,y) - z_{mean})^4 dxdy}{A} \right] \tag{A.4}$$

it is the fourth statistical moment of the z distribution. It is related to the tails of the distribution.

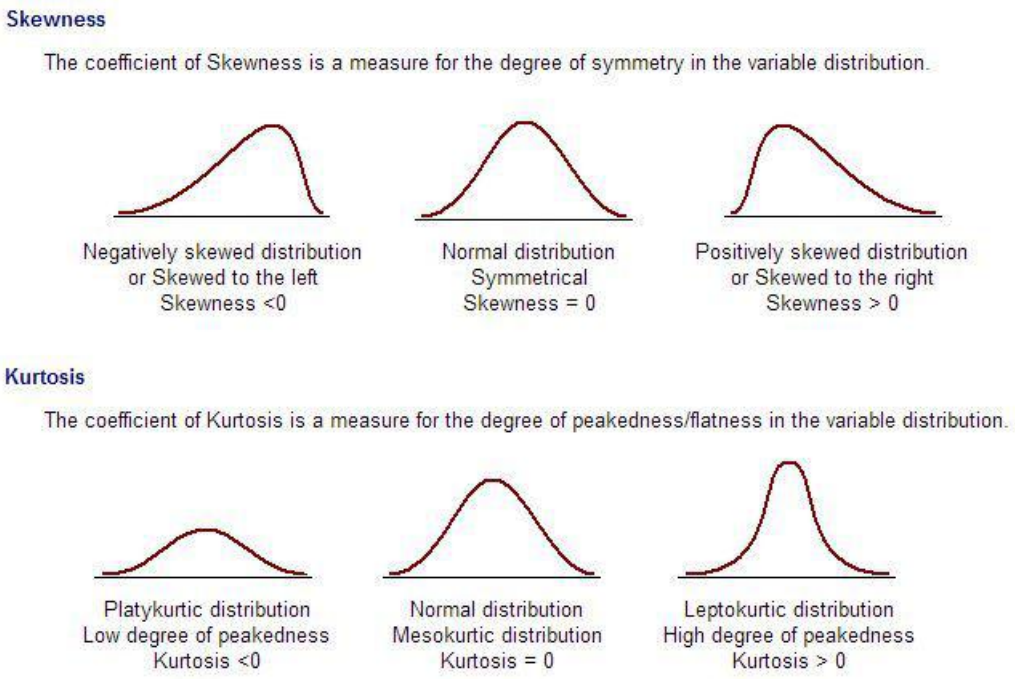

Figure A.1: Skewness and Kurtosis representation [44].

Appendix B

General measures on underlayer

General measurements are done to study the properties of the different underlayers. Density and hardness analyzes are done on the circular sample (d =90 mm) of underlayer (see Fig.4.15 right side), the detachment measurements at room temperature are done on the pad with the same friction material and different underalyer. All projects have minimum and miximum values to which detachment and compressibility must comply.

B.1 Density measurement

The density of UL is calculated using the Archimedes principle. The measurement is done by weighing the UL mass on the scale, then it is immersed in water ($\varrho = 1\, g/cm^3$) and weighed. This measure allows to calculate the density of the underlayer:

$$m_{UL}g - m_{UL_{H_20}}g = \varrho_{H20}gV_{UL} \tag{B.1}$$

simplified gravity acceleration and dividing by m_{UL} to both members:

$$\varrho_{UL} = \varrho_{H20}\frac{m_{UL}}{m_{UL} - m_{UL_{H_20}}} \tag{B.2}$$

Following the table with the results obtained for density measurements. The error was calculated by repeating the measurement on three samples from the same batch.

UL	ϱ	σ_ϱ
	g/cm^3	g/cm^3
A	3.03	0.03
B	3.18	0.05
C	3.09	0.04
D	3.14	0.05
E	2.93	0.04
F	3.08	0.05
G	3.06	0.02
H	2.91	0.05
I	2.99	0.05
L	2.58	0.04
M	2.53	0.06
N	2.44	0.05
O	2.84	0.06

Table B.1: Density of UL.

It is observed that the density does not show a great variation and therefore the mass of the pad with different underlayers does not have significant mass differences. The lower density UL (L, M, N) are those for commercial vehicles (trucks) that have a different formulation, more similar to the friction material as they must withstand higher temperatures.

B.2 Hardness measurement

The hardness measurement is performed with a Galileo durometer, the penetration of one material on another material is measured [43]. The measurement is performed on five different points on the UL sample, the hardness of the underlayer is the average and the error is the standard deviation.

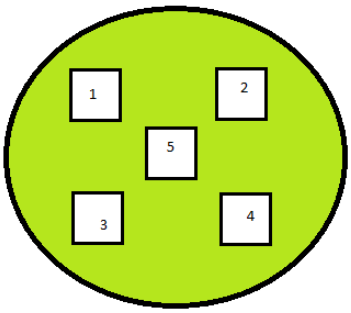

Figure B.1: Measuring points on the UL sample. The diameter is 90 mm.

The UL is placed between the support and the steel indenter (12.7 mm steel ball), the 10 kg preload is applied manually, then a load of 980.7 kN ($\sim$ 100 kg) is applied for a time of 10 s; at the end it is measured how much the penetrator has entered the material. The scale used for the measurement is the Rockwell scale:

$$Hardness = 130 - \frac{h}{0.002mm} \tag{B.3}$$

h (mm) is the depth of the mark left by the indenter.

UL	Hardness	$\sigma_{Hardness}$
A	52	4
B	43	7
C	50	3
D	43	3
E	34	3
F	42	5
G	39	4
H	40	9
I	30	5
L	34	5
M	41	5
N	37	5
O	60	7

Table B.2: Hardness of UL.

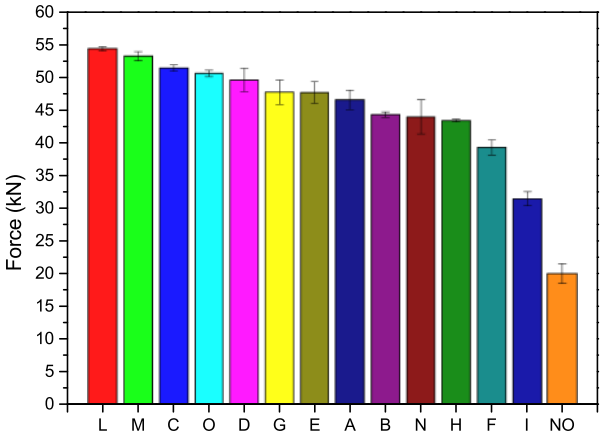

Figure B.2: Detachment of UL.

B.3 Shear stress measurement

The resistance to shear stress measurement is performed on the pad at room temperature. The adhesion between friction material, underlayer and metal back plate is evaluated. The force is applied parallel to the surface of the friction material, the load is applied by a piston, a metal support is used to interface the piston to the pad. The load is applied 1 mm from the metal back plate, it increases by 4.5 ± 0.5 kN/s until the friction material breaks. The minimum detachment value depends on the application project. The analysis was done on the friction material with different substrates, the measurement was repeated three times on different brake pads of the same batch.

Fig. B.2 shows that a friction material without UL has poor adhesion with the metal back plate, this is the main safety issue for which a material without UL cannot be used (in addition to noise problems).

B.4 Compressibility measurement

The compressibility is measured on the brake pad, a piston apply 160 bar on the metal back plate and the compressibility is measured. The minimum and maximum compressibility value depends on the application project. The measurement was repeated three times on different brake pads of the same batch.

UL	$Shear force$	σ_{Force}
	kN	kN
A	46	1
B	44.2	0.4
C	51.3	0.5
D	49	2
E	48	2
F	39	1
G	48	2
H	43.3	0.2
I	31	1
L	54.3	0.3
M	53	1
N	44	3
O	50.5	0.5
No	20	2

Table B.3: Detachment values of UL.

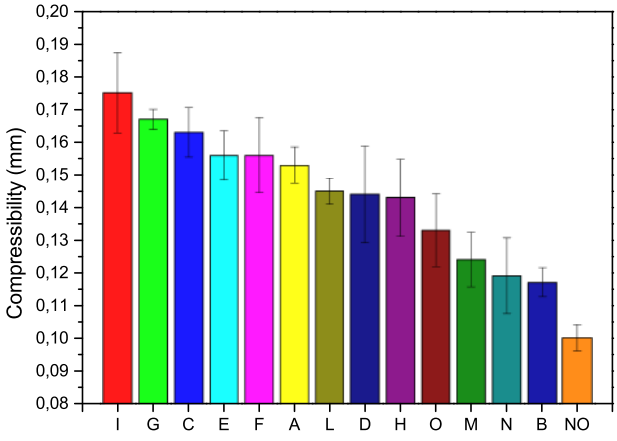

Figure B.3: Compressibility of UL.

Appendix C

Correlation matrix

The correlation matrix is a n x n symmetric matrix with n the number of variables studied. The single element ρ_{ij} is the Pearson correlation coefficient between the variable i and the variable j, defined as the ratio between the covariance σ_{ij} and the product of the two standard deviations $\sigma_i \sigma_j$:

$$\rho_{ij} = \frac{\sigma_{ij}}{\sigma_i \sigma_j} \tag{C.1}$$

Pearson correlation coefficient is a number between 1 and -1. An index of 1 indicates a positive linear correlation, 0 a no linear correlation and -1 a negative correlation [42]. The correlation matrix is:

$$\begin{pmatrix} 1 & \rho_{12} & ... & ... & \rho_{1n} \\ \rho_{21} & 1 & ... & ... & ... \\ ... & ... & 1 & ... & ... \\ ... & ... & ... & ... & ... \\ \rho_{n1} & ... & ... & ... & 1 \end{pmatrix} \tag{C.2}$$

The elements on the main diagonal are obviously equal to 1 ($\rho_{ii} = 1 \ \forall i$).

Bibliography

[1] http://www.autoworksofdestin.com/brake-system-operation-and-inspection.jpg

[2] http://cdn.elaborare.com/wp-content/uploads/2016/02/Pastiglia-freno-composizione.jpg

[3] DAY, Andrew J. Braking of road vehicles. Butterworth-Heinemann, 2014.

[4] LIU, Weiming; PFEIFER, Jerome L. Introduction to brake noise and vibration. Honeywell Friction Materials, 2003.

[5] BHUSHAN, Bharat (ed.). Nanotribology and nanomechanics: an introduction. Springer Science and Business Media, 2008 for Steel Treating, Vol. II

[6] STRAFFELINI, Giovanni. Friction and wear. Methodologies for Design and Control. Switzerland: Springer International Publishing AG Switzerland, 2015.

[7] TEGZES, Pal. Stability, Avalanches and Flow in Dry and Wet Granular Materials. Thesis, 2002.

[8] POPP, K.; STELTER, P. Stick-slip vibrations and chaos. Philosophical Transactions: Physical Sciences and Engineering, 1990, 89-105.

[9] PATEK, S. N.; BAIO, J. E. The acoustic mechanics of stick–slip friction in the California spiny lobster (Panulirus interruptus). Journal of Experimental Biology, 2007, 210.20: 3538-3546.

[10] Di Liberto, F., Balzano, E., Serpico, M., Peruggi, F. (2010). What We Can Learn About Stick-Slip Dynamics. In Applied Mechanics and Materials (Vol. 24, pp. 343-348). Trans Tech Publications Ltd.

[11] POPOV, Valentin L.; GRAY, J. A. T. Prandtl-Tomlinson Model: A Simple Model Which Made History. In: The History of Theoretical, Material and Computational Mechanics-Mathematics Meets Mechanics and Engineering. Springer, Berlin, Heidelberg, 2014. p. 153-168.

[12] NOSONOVSKY, Michael; BHUSHAN, Bharat. Multiscale friction mechanisms and hierarchical surfaces in nano-and bio-tribology. Materials Science and Engineering: R: Reports, 2007, 58.3-5: 162-193.

[13] BHUSHAN, Bharat. Adhesion and stiction: mechanisms, measurement techniques, and methods for reduction. Journal of Vacuum Science and Technology B: Microelectronics and Nanometer Structures Processing, Measurement, and Phenomena, 2003, 21.6: 2262-2296.

[14] VAKIS, A. I., et al. Modeling and simulation in tribology across scales: An overview. Tribology International, 2018, 125: 169-199.

[15] MAEGAWA, Satoru; ITOIGAWA, Fumihiro; NAKAMURA, Takashi. Effect of surface grooves on kinetic friction of a rubber slider. Tribology International, 2016, 102: 326-332.

[16] HÖLSCHER, Hendrik; SCHIRMEISEN, André; SCHWARZ, Udo D. Principles of atomic friction: from sticking atoms to superlubric sliding. Philosophical Transactions of the Royal Society A: Mathematical, Physical and Engineering Sciences, 2008, 366.1869: 1383-1404.

[17] ERIKSSON, Mikael; JACOBSON, Staffan. Tribological surfaces of organic brake pads. Tribology international, 2000, 33.12: 817-827.

[18] NOH, H. J.; JANG, Ho. Friction instability induced by iron and iron oxides on friction material surface. Wear, 2018, 400: 93-99.

[19] LEE, Sangmok; JANG, Ho. Effect of plateau distribution on friction instability of brake friction materials. Wear, 2018, 400: 1-9.

[20] Gottfried W. Ehrenstein, "Polymeric Materials", Hanser, (2001)

[21] Marco Zanetti, Dispense Modulo polimeri, Corso di Studi in Chimica e Tecnologie Chimiche, UNITO, (2012/2013)

[22] P.E.Rouse, "A theory of the Linear Viscoelastic Properties of Dilute Solutions of Coiling Polymers", J. Chem. Phys., 21, 1272 (1953)

[23] TriboLab. TriboLab. URL: https : / / www . bruker . com / products / surface - and -dimensional-analysis/tribometers-and-mechanical-testers/umt/tribolab/overview.html.

[24] Nanovea. Profilometer. URL: https://nanovea.com/instruments/?p=profilometers.

[25] https://www.zeiss.com/microscopy/int/products/scanning-electron-microscopes.html

[26] https://www.inrim.it/ricerca-sviluppo/laboratori-di-ricerca/nanofabbricazione-e-caratterizzazione-di-dispositivi

[27] https://www.inrim.it/ricerca-sviluppo/dal-macro-al-nanomondo

[28] Kevin P.Menard, "DYNAMIC MECHANICAL ANALYSIS A pratical introduction", CRC Press LLC, (1999)

[29] U.W. Gedde, "Polymer Physics", Spinger ed. (1999)

[30] http://polymerinnovation.com/wp-contenent/uploads/2015/04/polymer-molecule-2.jpg

[31] http://www.continuummechanics.org/images/dynamats/stress-strains-sines.png

[32] Malcom L. Williams, Robert F. Landel and John D. Ferr. "The Temperature Dependence of Relaxation Mechanisms in Amorphous Polymers and Other Glass-forming Liquids", Journal of the American Chemical society 77.14 (1955): 3701-3707

[33] Doolittle, Arthur K. "Studies in Newtonian flow. II.The dependence of the viscosity of liquids on free-space." Journal of Applied Physics 22.12 (1951): 1471-1475

[34] MetraviB, "Analizzatori Meccanici Dinamici: Specifica per l'uso", (2009)

[35] Booij, H. C., and G.P.J.M. Thoone. "Generalization of Kramers-Kronig transforms and some approximations of relations between viscoelastic quantities." Rheologica Acta, 21(1), 15-24

[36] Emmanuel Chailleux, Guy Ramond, Christian Such Chantal de La Roche "A mathematical-based master-curve construction method applied to complex modulus of bituminous materials". Road Materials and Pavement Design 7.sup1 (2006): 75-92

[37] Alessandro Rivola, "Meccanica e dinamica delle macchine", UNIBO, inedito.

[38] HESLOT, F., et al. Creep, stick-slip, and dry-friction dynamics: Experiments and a heuristic model. Physical review E, 1994, 49.6: 4973.

[39] Manfred Abele, "Manuale per l'industria della gomma", Bayer (1972)

[40] Treccani, "Enciclopedia della Scienza e della tecnica", (2008)

[41] M. Sc. Jarlath Mc Hugh - "Ultrasound Technique for the Dynamic Mechanical Analysis (DMA)of Polymers". BAM, Berlino (2008)

[42] Roberto Todeschini, "Introduzione alla Chemiometria", Edises, Bologna, (1998)

[43] S.P. Rockwell, "The Testing of Metals for Hardness", Transactions of the American Society

[44] https://www.bidmc.org/-/media/files/beth-israel-org/research/research-centers/smith-center-for-outcomes-research-in-cardiology/09-26.pdf

[45] G. Costagliola, F. Bosia, N.M. Pugno, *Tuning friction with composite hierarchical surfaces*, Tribol. Int. 115 (2017) 261

[46] Costagliola, Gianluca, Federico Bosia, and Nicola M. Pugno. "A 2-D model for friction of complex anisotropic surfaces." Journal of the Mechanics and Physics of Solids 112 (2018): 50-65.

[47] S, Balestra, G. Costagliola, A. Pegoraro, F. Picollo, A. Sin, J.-F. Molinari, F. Bosia, E. Vittone, N. M. Pugno, "Modication of the frictional properties of polymer surfaces through surface patterning", submitted to Tribology International

[48] Fiaschi, Giulia, et al. "Tribological response of laser-textured steel pins with low-dimensional micrometric patterns." Tribology International (2019): 105548.

[49] Greiner, Christian, et al. "Contact splitting and the effect of dimple depth on static friction of textured surfaces." ACS applied materials and interfaces 6.11 (2014): 7986-7990.

[50] M.J. Baum, L. Heepe, E. Fadeeva, S.N. Gorb, *Dry friction of microstructured polymer surfaces inspired by snake skin*, Beilstein J. Nanotechnol. 5 (2014) 1091

[51] B. Murarash, Y. Itovicha, M. Varenberg, *Tuning elastomer friction by hexagonal surface patterning*, Soft Matters 7 (2011) 5553

[52] N. Li, E. Xu, Z. Liu, X. Wang, L. Liu, *Tuning apparent friction coefficient by controlled patterning bulk metallic glasses surfaces*, Sci. Rep. 6 (2016) 39388

[53] B. He, W. Chen, Q.J. Wang, *Surface Texture Effect on Friction of a Microtextured Poly(dimethylsiloxane) (PDMS)*, Trib. Lett. 31 (2008) 187

[54] N.B. Tay, M. Minn, S.K. Sinha, *A Tribological Study of SU-8 Micro-Dot Patterns Printed on Si Surface in a Flat-on-Flat Reciprocating Sliding Test* Trib. Lett. 44 (2011) 167

[55] C. Greiner, M. Schafer, U. Pop, P. Gumbsch, *Contact splitting and the effect of dimple depth on static friction of textured surfaces*, Appl. Mater. Interfaces 6 (2014) 7986

[56] Wang, D. W., et al. "Disc surface modifications for enhanced performance against friction noise." Applied Surface Science 382 (2016): 101-110.

[57] Gnilitskyi, Iaroslav, et al. "Tribological Properties of High-Speed Uniform Femtosecond Laser Patterning on Stainless Steel." Lubricants 7.10 (2019): 83.

[58] Capozza, Rosario, and Nicola Pugno. "Effect of surface grooves on the static friction of an elastic slider." Tribology Letters 58.3 (2015): 35.

[59] Österle, Werner, and Ingrid Urban. "Third body formation on brake pads and rotors." Tribology International 39.5 (2006): 401-408.

[60] Costagliola, Gianluca, Federico Bosia, and Nicola M. Pugno. "Static and dynamic friction of hierarchical surfaces." Physical Review E 94.6 (2016): 063003.

[61] R. Burridge and L. Knopoff, "Model and theoretical seismicity", Bull. Seismol. Soc. Am. 57 (1967) 341

[62] O.M. Braun, I. Barel, M. Urbakh, "Dynamics of Transition from Static to Kinetic Friction", Phys. Rev. Lett. 103 (2009) 194301

[63] J. Trømborg, J. Scheibert, D.S. Amundsen, K. Thøgersen, A. Malthe-Sørenssen, "Transition from Static to Kinetic Friction: Insights from a 2D Model", Phys. Rev. Lett. 107 (2011) 074301

[64] E. Absi, W. Prager, "Comparison of equivalence and finite element methods", Comp. Methods. in Appl. Mech. Eng. 6 (1975) 59

[65] F. P. Bowden and D. Tabor, "The Friction and Lubrication of Solids", Oxford University Press, Oxford, 1950

[66] L. Frérot, M. Bonnet, J.F. Molinari, G. Anciaux "A Fourier-accelerated volume integral method for elastoplastic contact", Computer Methods in Applied Mechanics and Engineering 351 (2019) 951

[67] https://tamaas.readthedocs.io/en/latest/index.html

[68] S. Balestra, A. Sin, V.Iodice "Method to select an elastomeric material for making an underlayer of a braking pad corresponding braking pad", Filing Date: 17.09.2020, Application number: 102020000021889, Jurisdiction: Italy